

**Design and Construction of a One-Dimensional Particle  
Tracker for Measurement of Alpha Particle Stopping  
Power**

by

Sarah Watt

A thesis submitted to the  
School of Graduate and Postdoctoral Studies in partial  
fulfillment of the requirements for the degree of

**Master of Applied Science in Nuclear Engineering**

Faculty of Energy Systems and Nuclear Science

University of Ontario Institute of Technology

Oshawa, Ontario, Canada

August 2019

© Sarah Watt, 2019

# THESIS EXAMINATION INFORMATION

Submitted by: **Sarah Watt**

## Master of Applied Science in Nuclear Engineering

Design and Construction of a One-Dimensional Particle Tracker for Measurement of Alpha Particle Stopping Power
--

An oral defense of this thesis took place on August 6, 2019 in front of the following examining committee:

### Examining Committee:

Chair of Examining Committee	Dr. Hossam Gaber
Research Supervisor	Dr. Anthony Waker
Research Co-supervisor	N/A
Examining Committee Member	Dr. Brian Ikeda
Examining Committee Member	Dr. Eleodor Nichita
Thesis Examiner	Dr. Rachid Machrafi

The above committee determined that the thesis is acceptable in form and content and that a satisfactory knowledge of the field covered by the thesis was demonstrated by the candidate during an oral examination. A signed copy of the Certificate of Approval is available from the School of Graduate and Postdoctoral Studies.

## **Abstract**

The energy deposited by a charged particle in a medium is non-uniform and peaks near the end of the particle's path. The energy deposition through the medium is known as stopping power and the shape of this function is called the Bragg curve. Stopping power is typically calculated from first principles rather than measured due to the difficulty of doing so.

A one-dimensional particle tracker using gas electron multiplier technology was designed and constructed to directly measure the stopping power at 16 discrete points along the path of alpha particles emitted by  $^{241}\text{Am}$ . The use of tissue-equivalent gas allows the results to be compared to those expected within tissue.

The results obtained show that the detector concept has merit, although there is room for improvement. In particular, certain voltages and electric field strengths have room for optimization, and more sophisticated readout electronics could be used to reduce experiment run time.

**Keywords:** radiation, health physics, alpha particle, stopping power, gas electron multiplier

## **Author's Declaration**

I hereby declare that this thesis consists of original work of which I have authored. This is a true copy of the thesis, including any required final revisions, as accepted by my examiners.

I authorize the University of Ontario Institute of Technology to lend this thesis to other institutions or individuals for the purpose of scholarly research. I further authorize University of Ontario Institute of Technology to reproduce this thesis by photocopying or by other means, in total or in part, at the request of other institutions or individuals for the purpose of scholarly research. I understand that my thesis will be made electronically available to the public.



Sarah Watt

## **Statement of Contributions**

I hereby certify that I am the sole author of this thesis and that no part of this thesis has been published or submitted for publication. I have used standard referencing practices to acknowledge ideas, research techniques, or other materials that belong to others. Furthermore, I hereby certify that I am the sole source of the creative works and/or inventive knowledge described in this thesis.

## **Acknowledgements**

I would like to thank Dr. Anthony Waker, my supervisor, for giving me the opportunity to work on this project. His advice and mentorship during my time with him allowed me to learn a great deal and was vital in the completion of this thesis. I would also like to thank him for his patience with me during the ups and downs of the project.

I would like to thank my long-time partner Gregg Henry and my father Bill Watt for their emotional support during this project. They were always there for me when I needed them and I am not sure how I would have been able to get through it without them.

# Table of Contents

Abstract.....	i
Author’s Declaration.....	ii
Statement of Contributions .....	iii
Acknowledgements.....	iv
Table of Contents .....	v
List of Tables .....	viii
List of Figures.....	ix
List of Abbreviations and Symbols.....	xi
Chapter 1. Introduction .....	1
1.1 Thesis Objectives .....	2
1.2 Previous Work .....	3
1.3 Thesis Outline .....	3
Chapter 2. Background and Theory .....	5
2.1 Alpha Radiation .....	5
2.1.1 Brief History .....	5
2.1.2 Interactions with Matter .....	6
2.1.3 Stopping Power .....	9
2.1.4 Linear Energy Transfer .....	12
2.1.5 Range and Straggling.....	13
2.1.6 Health Effects.....	14
2.2 Gas-filled Radiation Detectors.....	17
2.2.1 Electron Interactions in Gas.....	17
2.2.2 Tissue Equivalence .....	18
2.2.3 Gas Multiplication Process and Proportional Counters .....	19

2.2.4 Gas Electron Multipliers .....	21
2.2.5 Shockley-Ramo Theorem .....	25
2.3 Radiation Detector Electronics .....	27
2.3.1 Charge-Sensitive Preamplifiers.....	27
2.3.2 Multi-Channel Analyzers.....	28
Chapter 3. Experiment Concept and Design Process.....	30
3.1 Concept .....	30
3.2 Design Process .....	33
3.2.1 Detector Design Process .....	33
3.2.2 Experiment Design Process .....	38
Chapter 4. Detector Design.....	42
4.1 Vacuum Chamber .....	43
4.2 Circuit Board Stack.....	45
4.3 Alpha Source, Source Holder, and Collimator .....	50
4.4 Main Board .....	54
4.4.1 Collector Pads .....	55
4.4.2 Multiplexer.....	58
4.4.3 Preamplifier.....	61
4.5 GEM Frame .....	62
4.6 Drift Board .....	63
4.7 Feedthroughs.....	67
4.8 External Connectors.....	72
Chapter 5. Experiment Components and Methodology.....	74
5.1 Experiment Components.....	74
5.1.1 Detector .....	75

5.1.2 Gas Filling Equipment .....	75
5.1.3 Fill Gas .....	77
5.1.4 Modular Crate .....	78
5.1.5 High Voltage Power Supply .....	79
5.1.6 Test Pulser.....	80
5.1.7 Oscilloscope .....	81
5.1.8 Multichannel Analyzer.....	82
5.1.9 Pad Selector .....	83
5.1.10 Laptop Computer .....	87
5.2 Experiment Methodology .....	87
5.2.1 Data Processing.....	90
Chapter 6. Experiment Results .....	92
6.1 Expected Results from Calculations .....	92
6.2 Raw Data.....	95
6.3 Calibration .....	96
6.4 Final Results .....	99
6.5 Discussion.....	101
Chapter 7. Conclusions .....	104
7.1 Future Developments .....	105
8 References.....	107

## List of Tables

Table 1 - TEG Composition by Weight Percent Compared to ICRU Tissue (from [24])	19
Table 2 - Raw Data .....	95
Table 3 - Data For Calibration Calculations .....	97
Table 4 - Calibration Factors .....	98
Table 5 - Final Results .....	100

## List of Figures

Figure 1 - Alpha Particle Interaction with Orbital Electron Resulting in a Delta Ray .....	8
Figure 2 - Representative Bragg Curve .....	10
Figure 3 - Electron microscope image of a standard CERN GEM foil (from [26]) .....	22
Figure 4 - Electric field in and around holes in GEM foil (from [26]) .....	23
Figure 5 - Typical GEM Configuration .....	24
Figure 6 - Shockley-Ramo Theorem Illustrated in a Parallel Plate Configuration .....	26
Figure 7 - Representative Output From an MCA .....	29
Figure 8 - Detector Concept .....	30
Figure 9 - Signal Flow .....	32
Figure 10 - Stack Concept .....	36
Figure 11 - Completed Detector .....	43
Figure 12 - Open Vacuum Chamber .....	44
Figure 13 - Stack Test Fit .....	46
Figure 14 - Stack Test Fit, Side View .....	46
Figure 15 - Render of Stack Concept .....	49
Figure 16 - Final Stack Assembly .....	50
Figure 17 - Collimator/Source Holder and Alpha Source .....	51
Figure 18 - Collimator Parameters .....	53
Figure 19 - Main Board .....	54
Figure 20 - Pad Electrical Schematic .....	58
Figure 21 - Multiplexer Section Schematic .....	59
Figure 22 - Preamplifier Schematic .....	62
Figure 23 - CERN Standard 50×50 mm GEM Frame .....	63
Figure 24 - Drift Board .....	64
Figure 25 - Drift Board Schematic .....	65
Figure 26 - All Four Electrical Feedthroughs .....	69
Figure 27 - Interior Connections .....	70
Figure 28 - Selector Feedthrough Sealed With Apiezon Q .....	71
Figure 29 - Inside of the "Pod" .....	72
Figure 30 - Exterior Pad Selector Connection .....	73
Figure 31 - Experimental Apparatus .....	74
Figure 32 - Gas Filling Equipment .....	76
Figure 33 - Oscilloscope .....	81
Figure 34 - DP5 Board Within NIM Module .....	83
Figure 35 - First Selector .....	85
Figure 36 - Second Selector .....	86
Figure 37 - Representative Energy Deposition Spectrum .....	91
Figure 38 - Stopping Power Calculated with SRIM .....	92
Figure 39 - Expected Energy Deposited by Region Within Detector .....	93
Figure 40 - Expected Stopping Power in Unit Density Propane-based Tissue-equivalent Gas .....	94
Figure 41 - Plot of Raw Data .....	96
Figure 42 - Plotted Calibration Factors .....	99
Figure 43 - Plot of Final Results .....	101

Figure 44 - Preamplifier Output..... 102

## List of Abbreviations and Symbols

BNCT	Boron Neutron Capture Therapy
CERN	Conseil Européen pour la Recherche Nucléaire
CSP	Charge-Sensitive Preamplifier
D	Diameter of Collimator
d	Distance
DIP	Dual In-line Package
DPP	Digital Pulse Processor
$ \mathbf{E} $	Electric field strength
E	Energy
eV	Electron Volt
FTDI	Future Technology Devices International
G	Pad Gap
GEM	Gas Electron Multiplier
H	Height of drift region
HV	High Voltage
I or i	Current
L	Length of Collimator
LED	Light-Emitting Diode
LET	Linear Energy Transfer
M	Mass
MCA	Multi-Channel Analyzer
N	Number

NIM	NIM (historically “Nuclear Instrument Module”) [1]
NIST	National Institute of Science and Technology
P	Power
p	Pressure
Q	Charge
R	Resistance
r	Range
S	Stopping Power
T	Total Width
RBE	Relative Biological Effectiveness
SHV	Safe High Voltage
SRIM	Stopping and Range of Ions in Matter
SSOP	Shrink Small Outline Package
TEG	Tissue-Equivalent Gas
USB	Universal Serial Bus
V	Voltage
W	Pad Width
x	Distance along path
$\alpha$	Alpha Particle
$\Delta$	Delta ray cutoff energy
$\delta$	Delta Ray
$\rho$	Density

## **Chapter 1. Introduction**

As heavy charged particles such as protons, alpha particles, and heavy ions pass through a medium, they lose energy and slow down by means of Coulomb force interactions with the medium's constituent atoms [2, 3, 4]. These interactions primarily consist of collisions with atomic orbital electrons and often result in ionization or excitation of the atom. Collisions can also occur between the particle and the atomic nucleus itself, but these nuclear interactions do not result in ionization or excitation, and energy losses in this manner do not become significant except when the incident particle is travelling at a very low velocity. Regardless of the specific nature of the interaction, the result is that energy is transferred from the incident particle to the medium it is passing through.

The average rate of energy loss per unit distance a charged particle experiences from interactions with the medium it is passing through is called the stopping power. The stopping power is constant for a given particle at a fixed energy travelling through a given medium at a fixed atomic composition and density. However, because the incident particle will constantly lose energy to the medium it is passing through, its stopping power will vary over the length of its path through the medium. When plotted and visually examined, the shape of the stopping power as a function of total distance travelled through the medium is called the Bragg curve, and it exhibits a peak called the Bragg peak near the end of its path. The Bragg peak represents the maximum value of the particle's stopping power.

The shape of the Bragg curve has consequences in different subfields of health physics, including charged particle beam therapy and internal dosimetry. In general, heavy charged particle radiation is more biologically dangerous towards the end of a particle's path as the particle reaches low energies because this is where the stopping power is the highest and

stopping power generally correlates well with biological damage [2, 5, 6, 7]. This property can be exploited to optimize radiotherapy using particularly heavy charged particles, such as carbon ions [8], as the energy of the beam can be tuned so that the beam stops within the tumor. In doing so, the majority of the beam's energy is deposited within the tumor rather than the healthy tissue that the beam has to pass through before reaching the tumor, thus maximizing damage to the tumor while sparing the healthy tissue as much as possible. However, the same property contributes to the reason that ingestion of alpha emitters can be dangerous. A particularly common form of alpha emitter ingestion is the inhalation of naturally-occurring radon gas [5]. The inhaled radon may decay while within the lungs, emitting an alpha particle in close proximity to vulnerable tissue. Because of the short range of alpha particles in human tissue, the alpha particles will come to a complete stop entirely within the lung tissue. This represents a hazard to cells along the particle's path, particularly towards the end of it.

Stopping power is typically calculated or simulated using a variety of methods that have existed for several decades and are considered to be adequate for most purposes [2, 9]. However, innovations in radiation detector technology have opened up new avenues that can be explored for direct measurement of the stopping in a medium.

## **1.1 Thesis Objectives**

The objective of this thesis is to describe the design, construction, and results of an experiment intended to directly measure the stopping power of alpha particles as they pass through tissue-equivalent material. The broader goal of this experiment is to investigate the possibility of using a particle tracker concept with low-pressure tissue-equivalent gas in

this particular application. Furthermore, apparatus similar to that described may have the potential to be used as a classroom demonstration of the Bragg curve.

## **1.2 Previous Work**

In many ways, this work is a continuation of a previous investigation performed by Andrej Sipaj for his Master of Applied Science thesis in completed in 2012 [10]. Sipaj examined the potential use of gas electron multiplier (GEM) technology for use in a one-dimensional particle tracking application for collecting stopping power measurements from alpha particles. His work included the design and construction of an experimental detector based on the concept, and the results from the experiment suggested that the concept is workable. Additionally, he identified areas where the concept had room for improvement.

While the design for the apparatus described in this thesis is original and does not use Sipaj's design as a starting point, it was based on the same concept and incorporated some suggestions from Sipaj's conclusion regarding how the concept could be improved. Furthermore, Sipaj's design was used as a benchmark while looking for additional ways in which the concept could be improved.

## **1.3 Thesis Outline**

The body of this thesis consists of four chapters. Chapter 2 provides background information on concepts that is necessary for a reader to understand the contents of the remaining three chapters. Chapter 3 provides an overview of the concept behind the experiment, as well as an explanation of the experiment's design process; both of these are intended to place the subsequent chapters in context as they delve into more specific aspects of the experiment. Chapter 4 describes in detail the design and construction of the

individual components that make up the detector used in the experiment. Chapter 5 provides a description of the other pieces of equipment used in the experiment and describes the methodology used in performing the experiment. Finally, Chapter 6 presents the results of the experiment and provides a discussion of them.

## **Chapter 2. Background and Theory**

### **2.1 Alpha Radiation**

#### **2.1.1 Brief History**

The form of radiation now known as alpha radiation was first investigated in 1896 by Henri Becquerel, when he observed photographic plates darkening in the vicinity of potassium and uranium salts [11]. In subsequent experiments, he discovered that the darkening effect was lessened by increasing the thickness of the light-tight aluminum shutters between the salts and the photographic plates. Becquerel originally thought that effect had something to do with the phosphorescence of the salts when exposed to sunlight, but found that the same effect occurred even in the dark and, therefore, seemed to be invisible rays that were emitted from the substance. These so-called “Becquerel rays” were likened to the x-rays that Wilhelm Roentgen had discovered the previous year, but further characterization differentiated them in that Becquerel rays were much more easily blocked by sheets of metal.

In 1899, Ernest Rutherford, through experimentation, discovered that Becquerel rays were in fact composed of two different types of radiation with different capabilities for penetration. The poorly-penetrating component was named “alpha radiation” and the other was called “beta radiation.” Later in 1899, Julius Elster and Hans Geitel discovered that the beta radiation were particles that could be deflected by a magnet. Further experiments by Bequerel in 1900 discovered that beta particles had the same mass-to-charge ratio as the electrons previously discovered by J. J. Thomson in 1897. Becquerel suggested that they were in fact electrons, and they quickly became accepted as such.

While earlier experiments suggested that alpha radiation could not be deflected by magnets, in 1903 experiments by Rutherford determined that they were in fact charged particles that could be affected by magnetic fields. The magnetic fields needed, however, were much greater than those used by Eltster and Geitel in their experiments due to the much higher mass of the particles. The results also showed that the charge of the alpha particles was opposite to that of beta particles.

Investigation continued into the precise nature of the alpha particle for several years. While evidence was building that the alpha particles were helium nuclei, it was not until 1909 that Rutherford and Thomas Royds published the results of an experiment that supported this hypothesis with high certainty [12]. While the question of the identity of the particles were solved within a mere decade of their discovery, it would not be until later that the mechanism of their emission was discovered. In 1928, George Gamow published a proof showing that alpha particles leave their parent nuclei via quantum tunneling, overcoming the strong potential barrier that would otherwise prevent their escape [4, 12].

### **2.1.2 Interactions with Matter**

As helium nuclei, alpha particles fall into the category of heavy charged particles. Heavy charged particles are defined as those particles which have a charge as well as a greater rest mass than electrons or positrons [2, 5, 13]. Other examples of heavy charged particles include protons, deuterons, and ions of heavier elements. Although the focus of this work is on alpha particles, it is worth noting that all heavy charged particles behave in a similar manner as they pass through matter.

At high velocities, alpha particles interact primarily with the orbital electrons in the constituent atoms of the medium that they are travelling through. It is possible for alpha particles to interact with the atomic nuclei, but this particular mechanism only becomes likely (and therefore significant) at much lower energies. The interactions with orbital electrons are through the Coulomb force with the positive charge of the alpha particle exerting an attractive force on the negative charge of the electrons.

As the alpha particle undergoes a series of collisions and near collisions with the electrons, it loses energy and slows down. However, due to the high mass of an alpha particle compared to the electrons it strikes, its course is altered only very slightly; it can be approximated as a straight line through its entire path length. A corresponding amount of energy is transferred to the electrons, causing the atoms to be ionized or excited. Electrons that have been freed from their atoms by the passage of the alpha particle are called “delta rays” if they gain enough energy in the interaction to travel a significant distance and cause further ionizations. Figure 1 illustrates the collision of an alpha particle with an orbital electron and the subsequent release of a delta ray.

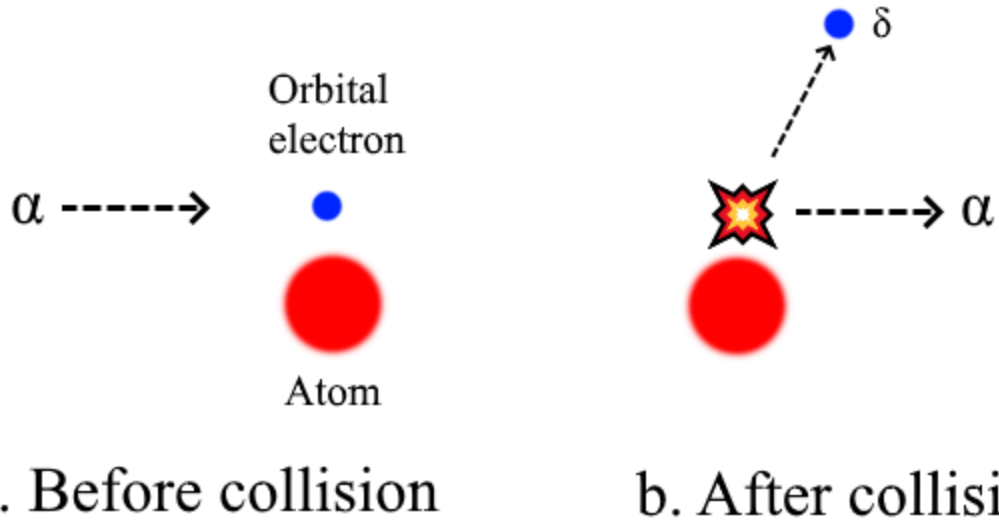


*Figure 1 - Alpha Particle Interaction with Orbital Electron Resulting in a Delta Ray*

When electrons are liberated from an atom, they have energy equal to the amount that was transferred to them from the alpha particle minus the small amount energy needed to ionize the atom. The maximum electron energy occurs during a direct head-on collision between the alpha particle and the electron [2, 13]. In this situation, the maximum energy without accounting for relativistic effects is

$$E_{max} = \frac{4mME}{(M + m)^2}$$

*Equation 1 - Maximum Energy Loss in Ion-Electron Collision*

Where M is the alpha particle's rest mass, m is the electron's rest mass, and E is the alpha particle's energy. This represents only about 0.055% of the alpha particle's energy, which works out to about 2.74 keV for a 5 MeV alpha.

At lower velocities, corresponding to energies below about 2 MeV, alpha particles become more likely to strike the nucleus of an atom directly. These collisions result in the loss of energy, but do not result in excitations or ionizations, although they may cause nuclear reactions to occur in certain isotopes. Additionally, the alpha particles begin to neutralize by gaining electrons from the medium. These interactions, which do not result in ionizations, are generally not detectable by radiation detectors, as radiation detectors typically measure the charge liberated within their sensitive volume. However, these interactions still contribute indirectly to the response of the detector by reducing the alpha particle's energy and thus altering the characteristics of the liberated charge that the detector "sees." In particular, the neutralization of the particle's charge has a profound effect on the rate of its energy loss, which is discussed in the next section.

### **2.1.3 Stopping Power**

Stopping power is a quantity that characterizes the "rate" of energy loss as charged particles, such as alpha particles, travel through a given medium [2, 5, 13]. While it is common to say "rate" in this context, it is not a true rate as it takes place over distance rather than over time.

Stopping power is mathematically expressed as

$$S(E) = -\frac{dE}{dx}$$

Where S is the stopping power of the given particle within a given medium, E is the particle's energy, and x is the distance it has travelled along its path through the medium.

Stopping power is a function of energy, and as the particle travels through the medium it loses energy. As the particle loses energy, its stopping power changes. Stopping power tends to increase at lower energies, forming a peak before it drastically drops off. This is the Bragg Peak, and the shape of the stopping power function is called the “Bragg curve.” A representative Bragg curve is presented in Figure 2. The sharp increase of stopping power represented by the Bragg peak is largely caused by the neutralization of the ion as it gains electrons from the medium; the change in its effective charge sharply affects the stopping power.

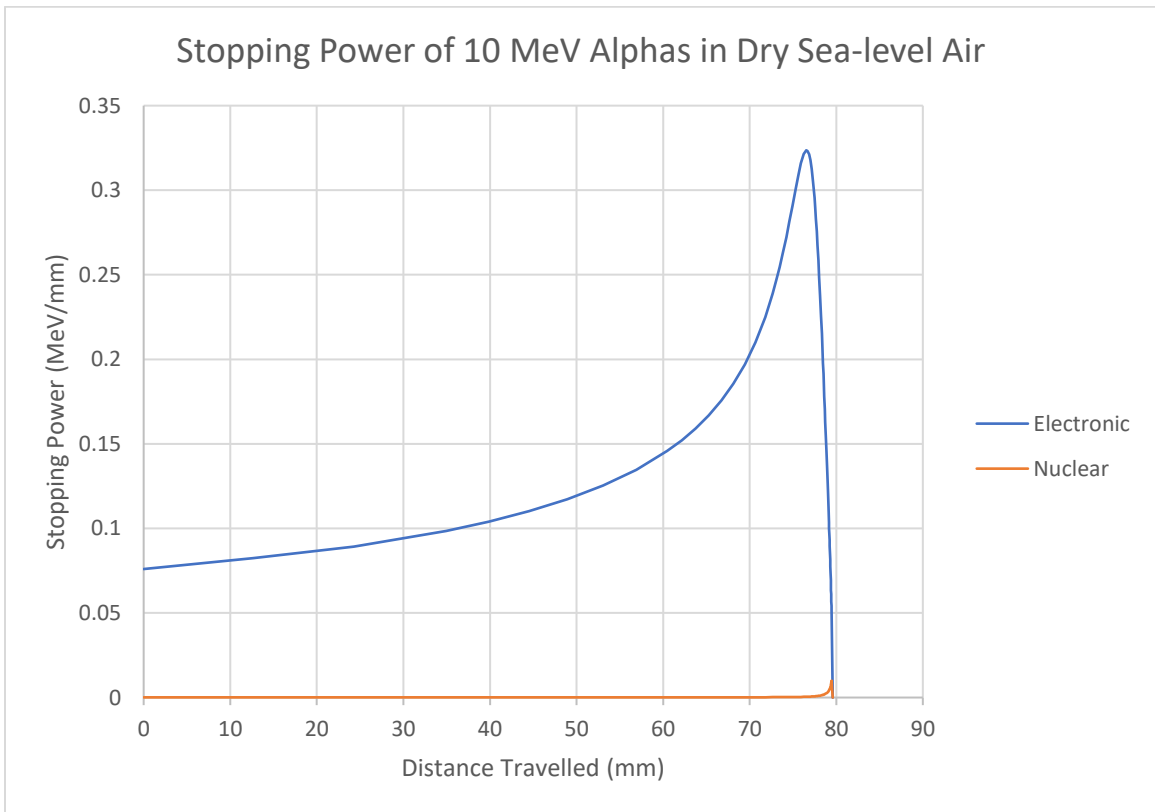


*Figure 2 - Representative Bragg Curve*

Stopping power is expressed in terms of “electronic stopping power,” which is the energy lost due to collisions with orbital electrons, and “nuclear stopping power,” which is due to collisions with nuclei. As seen in the example Bragg curve, nuclear stopping power comprises a negligible amount of the particle’s energy loss as it travels through the medium as compared with electronic stopping power, and it only increases beyond a vanishingly-small amount right at the end of the particle’s path.

Stopping power for heavy ions is fairly simple to calculate. A commonly-used [9] software program called SRIM can determine the stopping power for different heavy ions at different energies within different pure or mixed substances. It is available from [14] and has been used in this thesis, including to generate Figure 2.

Stopping power can also be represented as “mass stopping power” where the stopping power function is divided by the density of the medium in which the stopping power was measured or calculated. Mass stopping power is invariant for a given material composition, and the stopping power for a substance at a given density can be derived by multiplying the mass stopping power by that density. Mathematically, it is represented as

$$\frac{S(E)}{\rho} = -\frac{1}{\rho} \frac{dE}{dx}$$

Where  $\rho$  is the mass density of the medium. Because the mass stopping power is the same for any given density of a material as long as the atomic composition remains the same, the stopping power at different densities can be calculated simply by multiplying the mass stopping power by the density of interest.

The shape of the Bragg curve is a key contributor to the potential effectiveness of heavy ion beam therapy for the treatment of tumors. Because the stopping power is much higher near the end of the particle's path, it is advantageous to adjust the beam's energy so that the end of its path is within the tumor so that more of the beam's energy is deposited within the tumor than the intervening healthy tissue [6, 7]. This has the effect of limiting the damage to the healthy tissues while maximizing the damage sustained by the tumor. Ions heavier than alpha particles such as carbon ions have exceedingly "sharp" and "thin" Bragg peaks with much higher peak stopping powers within them than those within the rest of the beam's path as compared to lighter ions [8]. Therefore, beams consisting of such ions are superior for targeting tumors than lighter ions such as protons.

#### **2.1.4 Linear Energy Transfer**

Linear energy transfer (LET) is a quantity that is closely related to stopping power, and in certain cases is essentially the same thing [2]. While stopping power is the rate of energy loss from the particle, LET is the rate of energy transfer from the particle into the medium [2, 5, 13]. LET can be "restricted," meaning that the energy transfer excludes interactions that produce delta rays with an energy, and thus range within the medium of interest, above a certain value. However, unrestricted LET is identical to stopping power.

LET is mathematically expressed as

$$LET_{\Delta}(E) = \frac{dE_{\Delta}}{dx}$$

Where LET is the linear energy transfer for a given particle at a given energy incident upon a given medium and  $\Delta$  is the upper cutoff energy for delta rays.

The key difference compared with stopping power seen in the mathematical form is that the negative sign is missing. While both stopping power and LET are positive, stopping power represents *loss* of energy from the particle, thus requiring the negative sign to become positive, while LET represents the energy gained by the medium.

The  $\Delta$  represents the cutoff energy for delta rays produced. For instance,  $LET_{1 \text{ keV}}$  represents the LET that excludes delta rays above 1 keV. Because higher-energy delta rays have greater range, the restricted LET represents greater localization of the energy transfer. Unrestricted LET is expressed as  $LET_{\infty}$  and has no cutoff energy, thus taking into account the energy transfer from all delta rays including longer-ranged ones.

Many studies on radiological health effects relate the LET of radiation to the level of damage it is capable of causing on a cellular level [6, 7]. LET is used as one of the primary indicators of how dangerous a form of radiation is to living cells. Alpha particles have a high LET and therefore tend to present high risk to reproducing cells that they pass through. This is discussed in greater detail in Section 2.1.6.

### **2.1.5 Range and Straggling**

Because alpha particles lose energy at a fairly predictable rate as they pass through a medium, they have a fairly predictable range [2, 3, 5, 13]. The distance needed for an alpha particle to lose all of its energy, come to a stop, and become neutralized is easily predictable. However, alpha particles do not have large ranges compared with those of lighter charged particles incident upon the same medium. Even at the fairly high energies they are “born” at, their stopping power in materials is simply too great to allow them to go far before

losing all of their energy. They go only centimeters in air, down to only tens of micrometers in water or human tissue.

However, there is some statistical variance to the specific number of interactions a single particle goes through as well as the energy it loses during those interactions. Therefore, even within a beam of particles that all start at the same energy, there is some variation in the energy of particles at certain points in the beam's path as well as variation in the range of individual particles, as compared to what was predicted. This variance is called "straggling" [3].

Statistical variation in range is called "range straggling"; statistical variation in energy is called "energy straggling." Range straggling amounts to a variation of only a few percent from the average range in the substance. However, energy straggling has a greater effect, especially towards the end of a particle beam's path, resulting in a widening of the Bragg peak for the beam in aggregate beyond what may be expected for the Bragg peak exhibited by a single particle.

### **2.1.6 Health Effects**

Unlike most other forms of radiation, alpha particles are generally considered to not present a hazard to human health from external exposure [15]. This is because their range within human tissue is so small that they cannot penetrate the epidermis and reach the basal layer, which contains the stem cells that are generally accepted to be the targets of interest for producing deterministic effects and cancers. While epidermis thickness varies from individual to individual, and even from location to location on the same individual, the accepted average thickness is 70  $\mu\text{m}$  [16]. However, SRIM calculates a range in tissue-

equivalent material of about 40  $\mu\text{m}$  for 5.49 MeV alphas from  $^{241}\text{Am}$ . Therefore, it can be expected that an alpha particle at standard natural occurring energies, which are lower than that of  $^{241}\text{Am}$ , will come to a halt before they reach the sensitive stem cells and therefore will not damage cells that are vulnerable to radiation damage.

However, that is not to say that alpha particles present no risk to humans. In fact, alpha emitters present great danger to humans if ingested through various means such as inhalation, as the distance from the tissue surface to sensitive cells is lower than the range of the alpha particles in many key places. For instance, the depth of at-risk cells in the bronchiolar wall is 4-12  $\mu\text{m}$  [16] indicating that inhaled alpha emitters can be dangerous. The typical example of an alpha emitter that presents an inhalation hazard is  $^{222}\text{Rn}$ , which is part of the  $^{238}\text{U}$  decay chain [17].  $^{238}\text{U}$  is a naturally-occurring isotope that can be found in soil as well as many types of rocks and minerals, including those used for building materials such as granite. Because of this prevalence, high levels of  $^{222}\text{Rn}$  can potentially exist in the atmosphere of a residential area. In particular, enclosed, poorly-ventilated areas below ground, such as basements, present the greatest risk for radon buildup [18]. Lung cancer studies in North America and China show that the risk is not merely theoretical; the results indicate that residential radon is the second leading cause of lung cancer [19]. $\mu\text{m}$

While the short range of alpha particles means the emitters have to be ingested to be harmful, it also contributes to their effectiveness at killing cells. Their high energy combined with their short range means that alpha particles have a high average LET across the length of their path through the tissue. In the case of 5.49 MeV alphas from  $^{241}\text{Am}$ , SRIM calculates an LET with an average of approximately 100 keV/ $\mu\text{m}$  across the first half of its 40 micron path through tissue, before peaking to about 250 keV/ $\mu\text{m}$  near the end

of the second half of its journey. While experimental results vary, evidence suggests that incident radiation with LETs of 100 keV/ $\mu\text{m}$  to 200 keV/ $\mu\text{m}$  have the highest relative biological effectiveness (RBE) [7]. RBE is defined as the following relation:

$$RBE = \frac{\text{Dose of standard radiation needed to cause a certain effect}}{\text{Dose of incident radiation needed to cause the same effect}}$$

Depending on the source, the standard radiation is given as 250 keV peak x-ray photons or gamma ray photons from  $^{60}\text{Co}$ . Photon radiation has an RBE at or close to 1 due to its low LET, while alpha particles have high RBEs, at lower energies where their stopping power is the highest. Therefore, alpha particles are more dangerous, especially toward the end of their path, than even several times the amount of energy deposited by photon radiation.

While it is shown that alpha particles are dangerous to ingest, the same things that make them dangerous make them potentially useful in an emerging form of cancer treatment that involves the use of radiopharmaceuticals that incorporate alpha emitters. This treatment, known as targeted alpha therapy, combines an alpha emitter such as  $^{213}\text{Bi}$  combined with a cancer-targeting antibody or protein [20], or radium-223 dichloride, which biologically mimics calcium [21]. The basic principle is that the radiopharmaceutical is ingested and is preferentially sent to the location of the tumor by the body. Once there, the alpha emitters decay and release alpha particles within the tumor, hopefully killing cancerous cells. Another variant on the concept is boron neutron capture therapy (BNCT), where a non-radioactive pharmaceutical containing  $^{10}\text{B}$ , such as sodium borocaptate, is administered to the patient [7]. After the drug has time to build up in the patient's tumor, the tumor is irradiated with thermal neutrons.  $^{10}\text{B}$  has a high thermal neutron cross section, and when it

captures a neutron it ejects a high-energy alpha particle which is likely to pass through the cancerous cells in its vicinity.

## **2.2 Gas-filled Radiation Detectors**

### **2.2.1 Electron Interactions in Gas**

When electrons are liberated in gas by the passage of an alpha particle, there are a variety of things that can happen to the electrons as they pass through the gas. They will have some energy imparted to them, so they will be able to travel through the gas until they lose their energy and slow down to a stop due to their own collisions with the atoms in the gas [2, 3]. In doing so, they can potentially cause further ionizations of their own. Due to their lower charge, they tend to have greater range than the doubly-charge alphas at the same energy; due to their lower mass, they tend to change course upon collision rather than travelling in a mostly-straight line. Therefore, electrons often take a more torturous route through gas before they come to a stop.

There exists the possibility of an electron recombining with a positive ion; some molecules like O<sub>2</sub> have a high affinity for combining with free electrons to become negatively charged [3]. In either case, these electrons are effectively lost from the perspective of a radiation detector and will not contribute to the measured signal. It is generally desirable to reduce recombination as much as possible within a detector and limit the oxygen content of the detector's gas to prevent degradation of the signal.

If there is an electric field present in the gaseous cavity, the electrons will be accelerated by it. However, they will continue to collide with atoms in the gas and lose energy before being accelerated again. While the movement of the electrons is a halting motion, it

achieves an average velocity called the “drift velocity” [3, 22]. The drift velocity is a function of electric field strength and a quantity called “mobility,” which is intrinsic to the gas.

The special case where the electrons have the opportunity to gain enough energy between collisions to cause an ionization to occur on their next collision is of particular importance to radiation detectors and is discussed in Section 2.2.3.

### **2.2.2 Tissue Equivalence**

Oftentimes the goal of radiation measurement is to determine the risk that the radiation presents to humans. It can be useful to take measurements that relate directly to the biological harm that the radiation field can cause.

The structure of a material matters only a very small amount as far as radiation interactions are concerned. In fact, the difference between materials of the same atomic composition, but different structure, is only around 1% [23].

Therefore, substitutes for living tissue can be created by mimicking the atomic composition of tissue, even if the molecular structures are quite different. Materials that are designed with similar composition as tissue are called “tissue equivalent” and can be gas, which is useful for the construction of a gas-filled radiation detector. Because the range of a particle within the gas and probability of interaction per unit distance travelled generally scale linearly with density, a detector containing tissue-equivalent gas at, for example, 1/1000 the density of tissue simulates a mass of tissue 1/1000 the size of the detector’s real size. This allows the construction of macro-scale detectors that simulate microscopic tissue sizes, which is useful due to the difficulty of constructing exceedingly-small detectors [24]. The

practice of using detectors configured in this way to draw conclusions about the microscopic effects of radiation is called microdosimetry [24].

The molecular compositions of two common tissue-equivalent gases, or TEGs, are listed and compared to tissue in Table 1. While the nitrogen and hydrogen compositions of the TEGs are very close to the real thing, the carbon and oxygen ratios differ. However, carbon and oxygen have similar relevant properties so they are nearly interchangeable within a gas. Therefore, while the compositions of the two types of TEG do not precisely match that of tissue, they are a close enough match as far as radiation is concerned.

*Table 1 - TEG Composition by Weight Percent Compared to ICRU Tissue (from [24])*

<b>Element</b>	<b>Methane-based TEG</b>	<b>Propane-based TEG</b>	<b>ICRU standard Tissue</b>
Carbon (C)	45.6	56.9	11.1
Hydrogen (H)	10.2	10.3	10.1
Nitrogen (N)	3.5	3.5	2.6
Oxygen (O)	40.7	29.3	76.2

### **2.2.3 Gas Multiplication Process and Proportional Counters**

In a combination of sufficiently low gas pressures and sufficiently high electric field strengths, a process can take place where electrons being propelled by the electric field gain enough energy in between collisions with the gas to cause ionization [3, 22]. If this continues to happen, then one electron can become two, two can become four, four can become eight, and so on until a large number of electrons have been liberated from the gas. This process, called a Townsend discharge or “avalanche,” can happen in uncontrolled electric arcs, but it is cultivated on purpose within certain gas-filled radiation detectors [3]. Radiation detectors that make use of gas as a detection medium and make controlled use

of Townsend discharges are called “proportional counters” because the multiplication that takes place within them is predictable and constant as long as conditions do not change, so the output signal is proportional to the number of electrons liberated by the ionization caused by the radiation multiplied by the multiplication factor, or “gain.”

Some detectors make use of massive, uncontrolled discharges, such as Geiger-Muller tubes and spark detectors; these are excluded from this discussion, as they do not preserve proportionality.

Proportional counters have an advantage in that, with high enough gains, even single interactions can be measured relatively easily. Because the gain is constant for a given set of conditions, knowledge of the gain or the use of a calibration source of radiation allows signals from the tube to be directly related to the amount of energy deposited by radiation. Furthermore, the standard tissue-equivalent gas is usable as a proportional counter gas allowing the use of gas gain in such detectors to make single radiation events easy to detect and measure.

Standard proportional counters follow a basic design consisting of a “tube” made from a conductive cylindrical outer shell with a thin metal wire stretched across the center axis. The tube is gas-tight and is filled with a suitable low-pressure gas, such as tissue-equivalent gas mixtures or other specialized detector gas mixtures [3]. By electrically grounding the outer shell, which acts as the cathode, and applying a high positive voltage to the center wire, which acts as the anode, electric fields form around the center wire that are strong enough to support gas multiplication. When radiation ionizes gas within the tube, the electrons are attracted to the anode wire while the positive ions are attracted to the cathode

shell. When the electrons reach the multiplication area around the wire, avalanches occur that greatly increase the number of electrons travelling toward the anode. Because the resulting signal output by the tube is proportional to the number of electrons travelling toward the anode, the resulting signal is larger than if there was no gas multiplication. The area that supports gas multiplication is usually very small, so a large majority of ionization events within the tube are subjected to the same multiplication factor.

#### **2.2.4 Gas Electron Multipliers**

The typical design for a proportional counter, as discussed in the previous section, is a cylindrical tube with an anode wire. However, there are other ways to make use of gas gain within a radiation detector. There exists a class of detectors known as “micropattern gas detectors” which use finely-structure components manufactured with special techniques that only became common in the 1990s [3]. The use of structures on the micrometer scale allows a designer to have a great deal of control over the shape of the electric field within the detector, allowing the creation of radiation detectors that both incorporate proportional gas multiplication as well as position-sensitive output. This makes them useful in particle tracking applications.

One type of micropattern gas detector known as the “gas electron multipliers,” or GEM, was first examined in earnest in the second half of the 90s by Fabio Sauli of CERN [25]. GEMs are manufactured from a thin, non-conductive film, such as Kapton, that is plated with copper on both sides. Using photoresist etching techniques, tiny holes with diameters typically smaller than 100  $\mu\text{m}$  are chemically etched through both the copper and Kapton film at regular intervals. An electron microscope image of the holes in a GEM foil is shown in Figure 3.

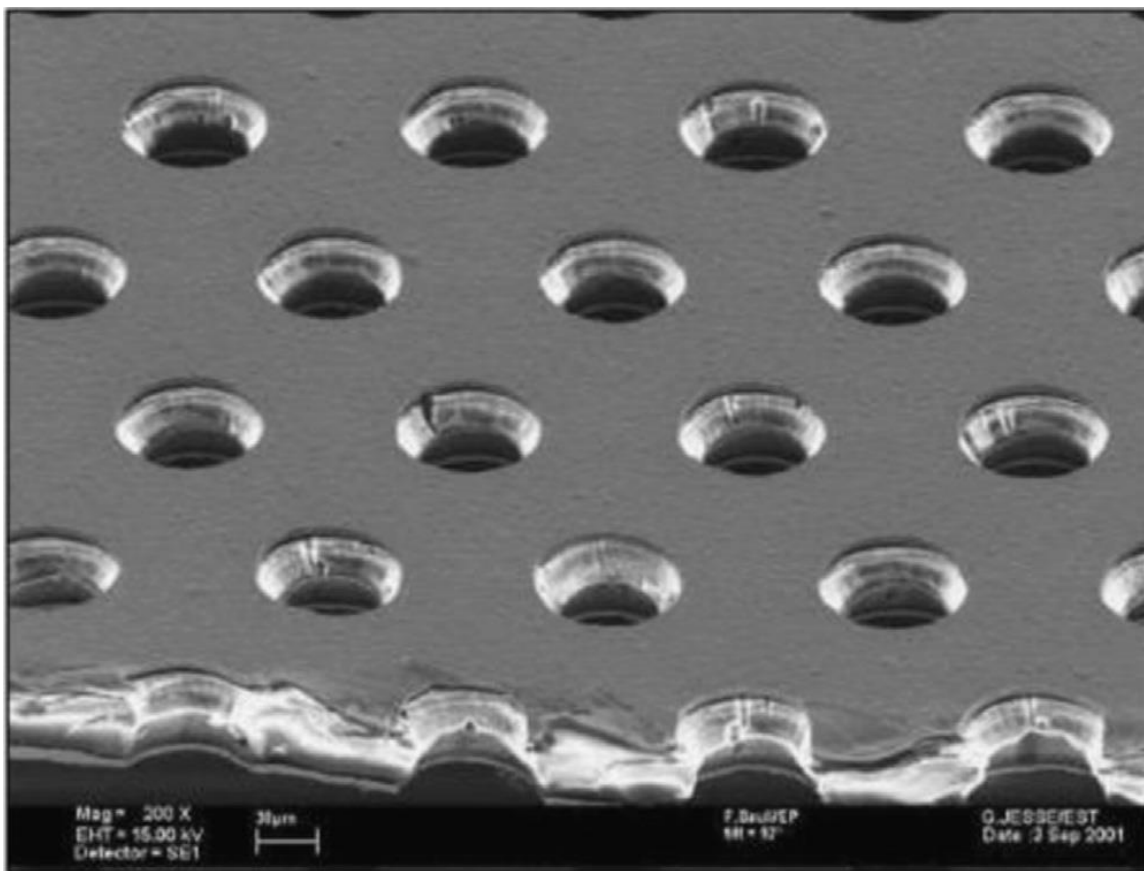


*Figure 3 - Electron microscope image of a standard CERN GEM foil (from [26])*

Due to the small size of these holes, the application of only a few hundred volts across both conductive sides of the GEM foil produce extremely high electric fields within the holes [25, 26]. An image depicting cross sections of the holes and the shape of the electric fields within them is shown in Figure 4. When paired with carefully-selected gas pressures, the conditions for high gas multiplication gains exist within the holes.

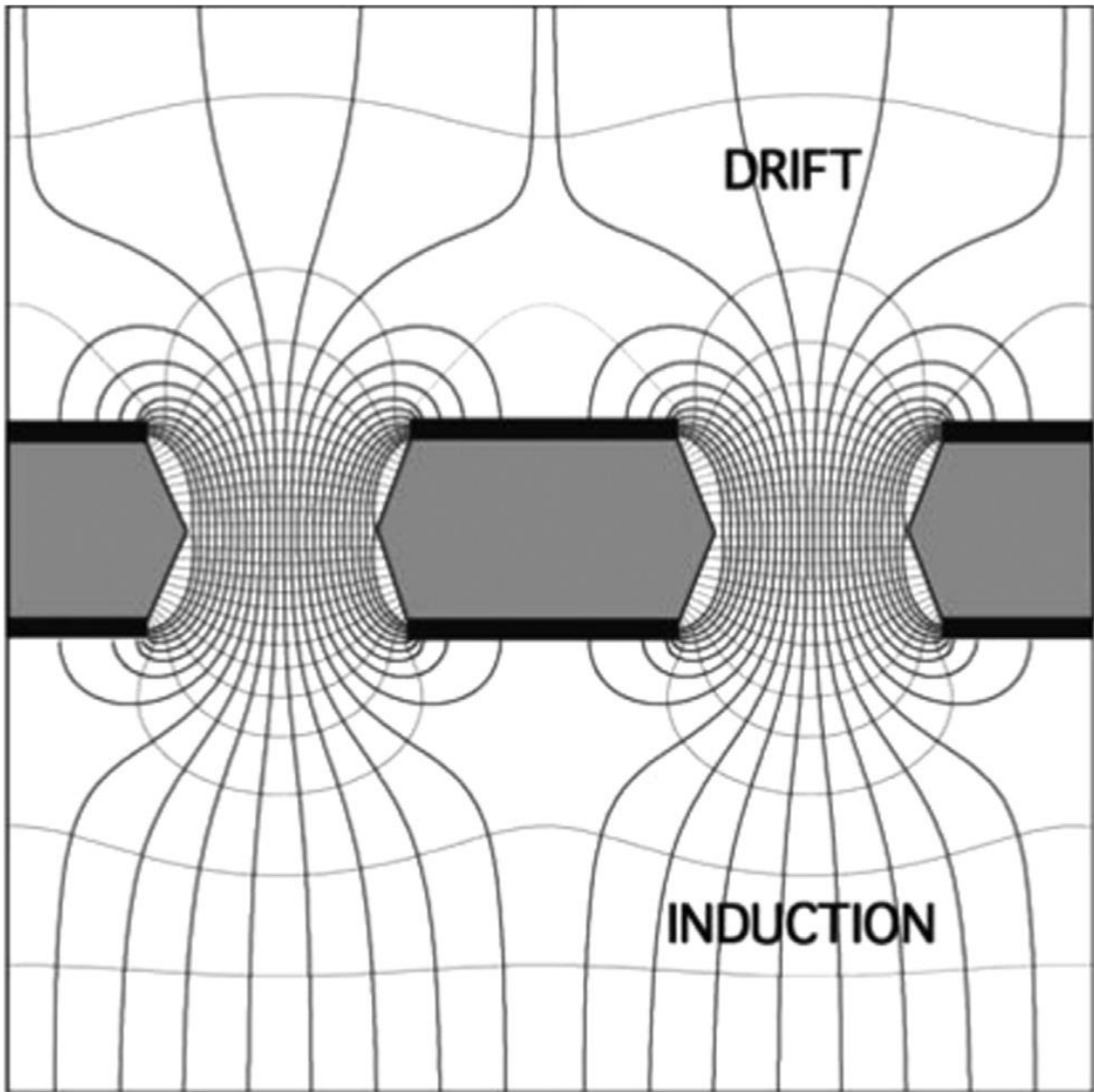


*Figure 4 - Electric field in and around holes in GEM foil (from [26])*

GEMs are not detectors in and of themselves and must be used in conjunction with other components in order to form a complete detector. A typical GEM configuration is shown in Figure 5. This figure (not to scale) illustrates the general spatial configuration of a detector that uses GEM technology. The GEM foil is suspended between two sets of electrodes – the drift plane and the collector electrodes. The area between the “top” of the

GEM and the drift plane electrode forms the “drift region” and the area between the “bottom” of the GEM and the collector electrodes forms the “induction region.”

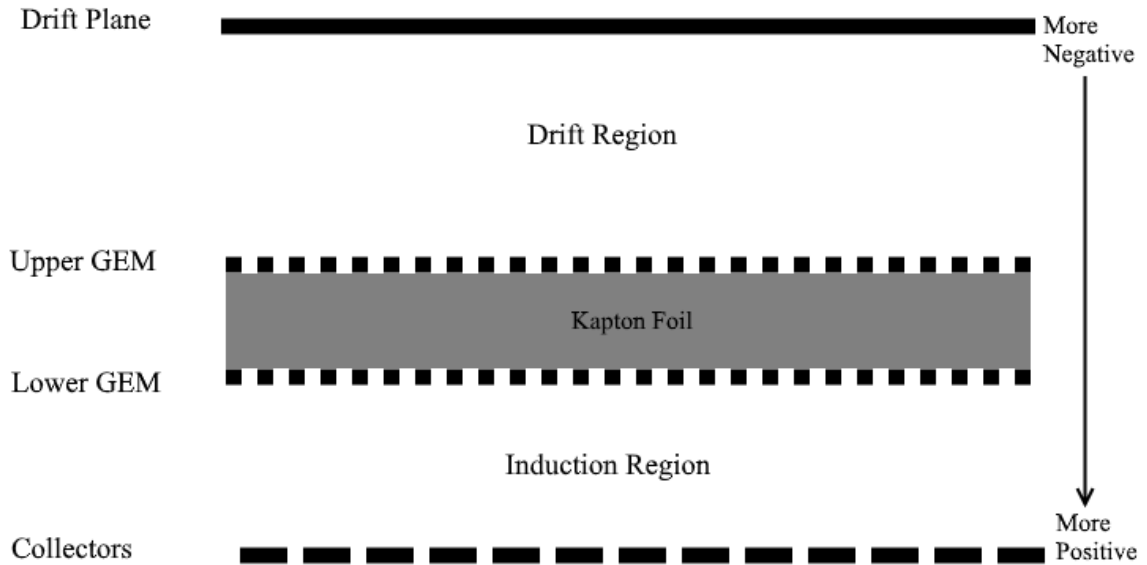


*Figure 5 - Typical GEM Configuration*

The drift plane electrode is the most negative part of the detector, followed by the upper conductive layer of the GEM, and then followed by the lower conductive layer, while the collectors are at ground potential. The result of this is that any electrons in the drift region (say, from the result of ionization by radiation interaction) are directed toward the GEM foil by the electric field because the upper side of the GEM is at a more positive potential. The shape of the electric field preferentially directs the electrons into the holes [27], where gas multiplication takes place. Most ions created during gas multiplication are neutralized on the upper side of the GEM foil, but some will enter the drift region and head toward the drift plane. The electrons, however, will mostly exit the bottom side of the GEM foil and head toward the collectors which represent the most positive part of the detector.

The holes in the GEM foil are small, generally less than 100  $\mu\text{m}$ , and are very densely packed, numbering nearly  $100\text{ mm}^{-2}$ . Because electrons generally are directed toward the closest hole, and electrons that exit head toward the closest electrode, the location of electrons arriving at the collectors corresponds very well with the location (on a 2-dimensional plane) that the ionization by radiation initially took place. Thus, with the collector electrodes configured correctly, the detector can determine the location of radiation interactions as well as how much energy they deposited. Therefore, it can be said that GEMs excel in particle tracking applications; in fact, that is why they were originally developed [25].

### **2.2.5 Shockley-Ramo Theorem**

The Shockley-Ramo Theorem, sometimes simply called Ramo's Theorem, describes a method for computing the current induced in a system of conductors as free electrical charges move in the presence of the conductors. It was first described by William Shockley in 1938 [28] and again independently by Simon Ramo in 1939 [29]. While originally intended to describe the behavior of currents in high frequency vacuum tubes where electronic transit time is longer than the period of the signal being amplified, it was later applied successfully to other applications, such as semiconductor radiation detectors [30] and is the currently-accepted method of modelling the effects of the movement of charge within gas-filled radiation detectors [3].

A rigorous description of the Shockley-Ramo Theorem will not be reproduced here as it is not necessary to understand the contents of this thesis. The salient point is that as charge moves through free space, no matter the reason why, charge in nearby conductors is

disturbed and begins to move, forming electrical currents. This is the mechanism for the formation of a signal within gas-filled detectors as charges move within them.

The behavior of moving charge in a system of two connected parallel plates is shown in Figure 6. Note that the current direction is in terms of the *conventional current* in standard use in circuit design and analysis. The flow of electrons through the conductors is actually in the opposite direction.

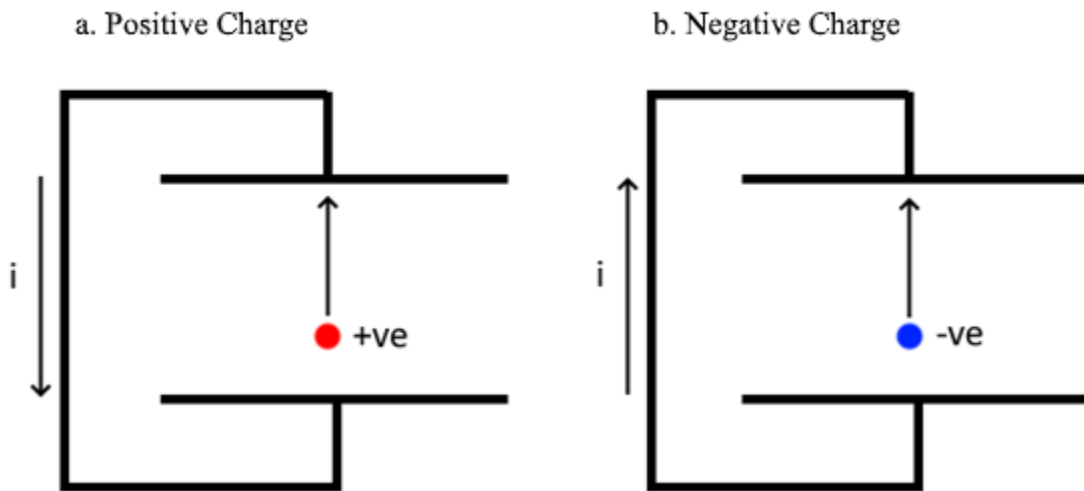


*Figure 6 - Shockley-Ramo Theorem Illustrated in a Parallel Plate Configuration*

The magnitude of the resulting current is based on not only the amount of moving charge, but also the geometry of the electrodes, the direction of its movement, and its speed. Within a radiation detector, most charge movement that is relevant to the formation of signals is the result of the electric field maintained within the detector due to the application of a high voltage. Due to their low mass, electrons accelerate very quickly in an electric field. Conversely, the high mass of heavy ions causes them to accelerate very slowly. The

electrons and ions have opposite charge and move in opposite direction, so they both contribute to current moving in the same direction. However, the electrons are “collected” very quickly ( $<1 \mu\text{s}$ ) while the positive ions take much longer to arrive at the cathode and be neutralized (tens of microseconds.) Therefore, the signal output by a proportional counter tube has a “fast” component caused by the electrons, and a “slow” component caused by the ions [3]. However, GEMs only have a fast component to the signal due to the signal being solely due to the electrons that exit the bottom of the foil [26].

Gases such as  $\text{O}_2$  that are highly electronegative and prone to forming negative ions affect the signal of a proportional counter in two undesirable ways [3]. When  $\text{O}_2$  takes an electron and becomes negatively charged, it moves along a similar path as an electron. However, the speed will be much lower, resulting in a contribution to the “slow” component rather than the fast component of the signal. Secondly, the negative ions generally do not cause avalanches, resulting in a loss of gain. Therefore, it is considered desirable to prevent oxygen from contaminating the gas within a proportional counter.

## **2.3 Radiation Detector Electronics**

### **2.3.1 Charge-Sensitive Preamplifiers**

Charge sensitive preamplifiers, or CSPs, integrate the charge pulse from a radiation detector and turn it into a more practical voltage pulse [3]. Many radiation measurement applications are interested in knowing the total amount of charge collected by the radiation detector during an interaction. CSPs help preserve that information even if the capacitance of the detector changes over time. This tends to be more of an issue with semiconductor radiation detectors, for which CSPs were designed, but advances in preamplifier design have caused CSPs to become standard in a much larger variety of radiation detector

applications, including setups using gas-filled proportional counters. The dominance of CSPs in the field is primarily due to their superior characteristics over the older voltage-sensitive configurations. Additionally, many other forms of radiation detector electronics are predicated on a detector setup using a CSP.

CSPs are available as standalone instruments for use as part of the signal chain in a radiation detection setup, or as modules that can be built into a project. While CSPs function in fairly similar ways, there is a great deal of variation in certain specifications that makes different CSPs useful in different applications. For instance, CSPs can be optimized for use with different types of detectors and can have different noise specifications and be rated for different maximum detectable charges per event.

### **2.3.2 Multi-Channel Analyzers**

Multichannel analyzers, or MCAs, process and measure the voltage pulses from CSPs. After subjecting the pulse from a CSP to a series of analog or digital processing stages designed to “shape” the signal into a more desirable form, the MCA measures the amplitude or “height” of the resultant pulse [3]. Once the height is known, the result is binned accordingly and displayed in a spectrum of counts versus channel, where the channel number indicates relative pulse height. With the use of a calibration process, the channel numbers indicate the amount of energy deposited within the detector by a given pulse.

Because of statistical variations, background radiation, and noise, a single count from a radiation detector is often not useful by itself. However, recording many counts and binning them by energy can reveal a great deal of information about the radiation being measured.

Once enough counts are collected and binned, analysis on the data can be performed visually or numerically. Peaks forming in the spectrum can provide information about which energy, or energies, are most commonly deposited by the radiation.

A representative spectrum from an MCA is shown in Figure 7. The x-axis represents the MCA's channels while the y-axis represents the number of counts binned in each channel. This data comes from an example file included with Amptek's DPPMCA multichannel analyzer software and depicts the spectrum collected from a  $^{60}\text{Co}$  source measured by a NaI scintillator detector. A visual examination of the spectrum reveals two prominent peaks in the data; these represent the 1.17 MeV and 1.33 MeV gamma rays that  $^{60}\text{Co}$  emits when it decays. Other phenomena such as pair production and Compton scattering are also visible in the data.

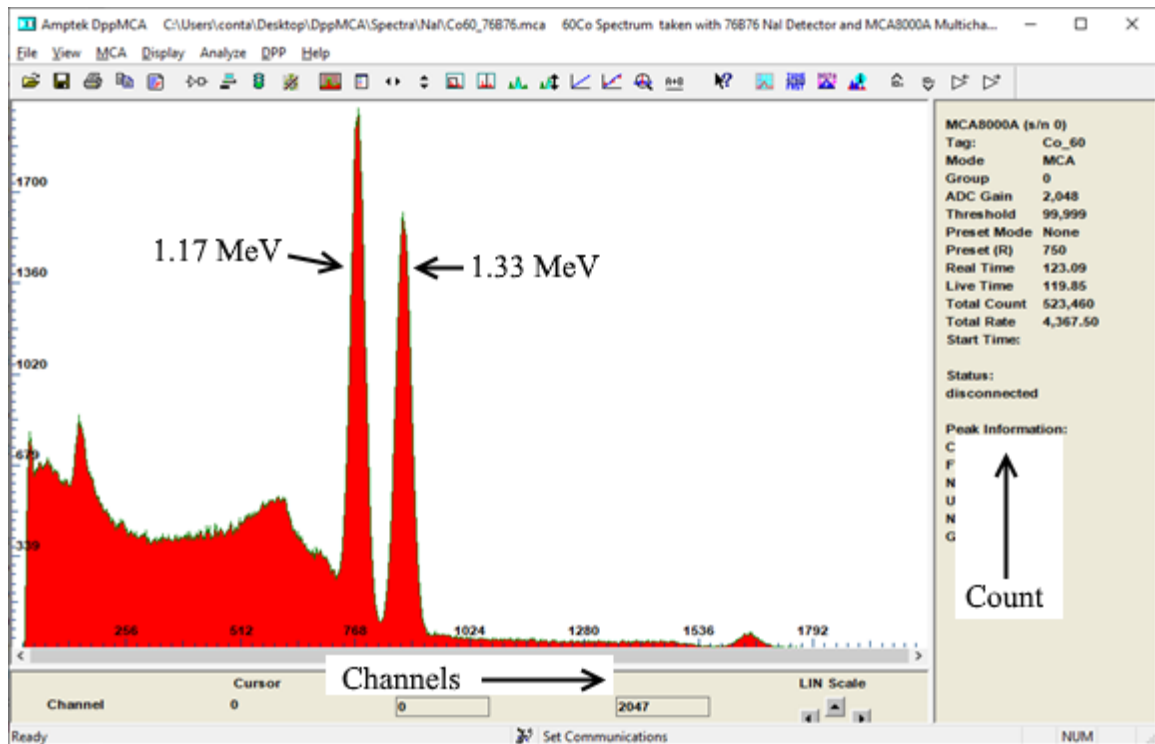


Figure 7 - Representative Output From an MCA

## Chapter 3. Experiment Concept and Design Process

This chapter has two sections that are intended to provide context for the subsequent chapters. The first section describes the concept that was envisioned for the detector used in the experiment. The second section describes the process that was followed to arrive at the design.

### 3.1 Concept

The detector constructed for the experiment was conceived as a standard GEM detector consisting of a single GEM foil between a drift plane and several readout pads. A basic diagram of the experiment as envisioned is depicted in Figure 8. Collimated alpha particles from an external alpha particle source enter the detector's drift region. As the alpha particles travel through the drift region, they cause primary ionizations, liberating electrons and delta rays from the gaseous medium filling the detector. The delta rays cause further ionizations as they are slowed down by the gas.

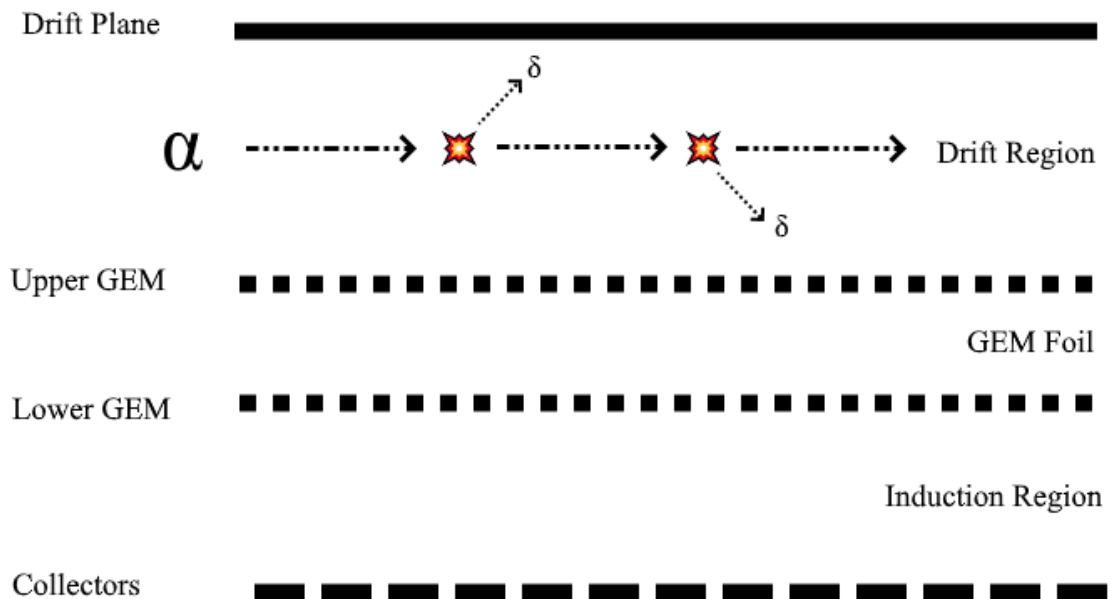
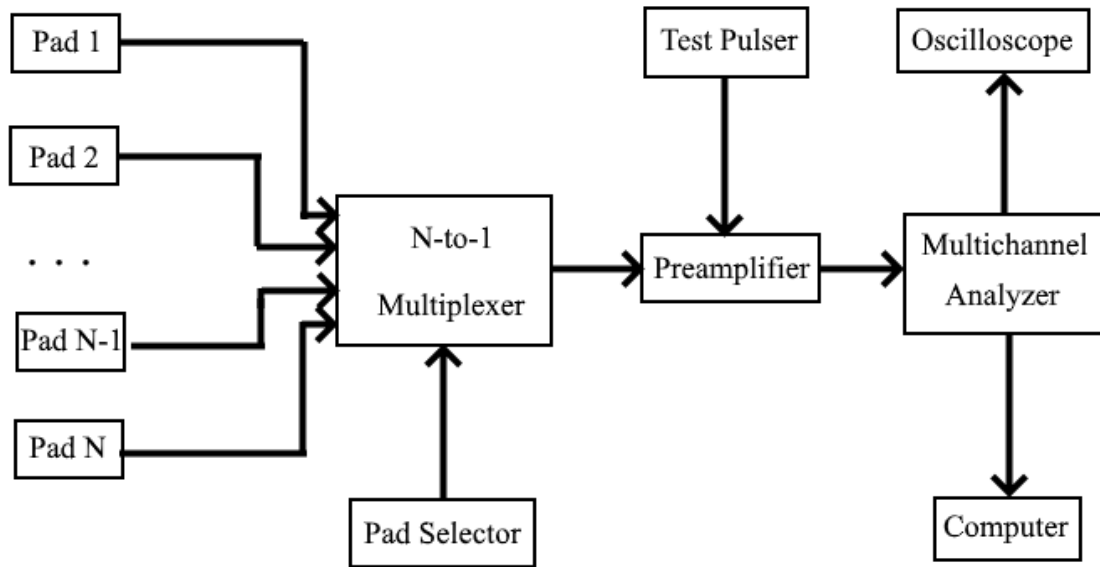


Figure 8 - Detector Concept

The electric field present in the drift region, resulting from a high potential difference between the drift electrode and “upper” side of the GEM, directs electrons within the volume toward the GEM foil. The electric field in this region is not high enough for multiplication to take place. However, as the electrons enter the holes in the GEM foil, they undergo a gas multiplication process due to the very high electric fields within the holes. For every electron that enters a hole in the GEM, several come out the other side; this multiplication factor is also referred to as the “gain” of the GEM.

As the electrons exit the holes and enter the region below the GEM, known as the “induction region,” they undergo no further multiplication due to the electric field present in that region and are directed toward the collector electrodes. As the electrons travel to the collector electrodes, also called “collector pads” or simply “pads,” they induce electrical signals in the pads as per the Shockley-Ramo theorem.

Because there are several collector pads placed along different sections of the alpha particle’s path, a many-to-one multiplexer is used to select which of the signals is currently being measured. The signal is directed toward a charge-sensitive preamplifier, which converts the total amount of charge collected by the electrode that is currently selected into a voltage signal. Finally, the signal is measured and processed by a multichannel analyzer. This signal flow is visually depicted in Figure 9.



*Figure 9 - Signal Flow*

This particular signal processing configuration collects information on how much charge arrives at a single given collector pad from each particle that crosses the volume. Because the measured charge is proportional to the gain of the GEM, which should not vary much throughout the detector, the collected charge can be related to how much energy was deposited across the length of a given collector pad. Because of the random nature of alpha particle interactions, data will need to be collected from the crossings of many different alpha particles. The average result in conjunction with known parameters of the experiment will allow the average stopping power to be calculated along the segment of the particle's path corresponding to a given pad. This will then be repeated for each of the pads in the experiment. By plotting the results received from each pad, it is expected that the Bragg curve will become apparent. Furthermore, by using tissue-equivalent gas at a carefully-selected pressure as a detection medium, the results should be similar to those expected within living tissue.

## **3.2 Design Process**

The objective of the experiment was to measure the stopping power along the path of a beam of alpha particles as it passes through tissue-equivalent material. The detector required to collect the necessary data, therefore, needed to be position-sensitive along one axis as well as energy-sensitive. As equipment to perform the planned experiment was not readily available at the time of the start of the project, the detector needed to be designed and built for the experiment. Once the detector was designed, the experiment that makes use of it was then designed.

Section 3.2.1 describes the general design process that was used to arrive at the final detector design described in Chapter 4. Section 3.2.2 describes the general design process that was used to arrive at the final experiment described in Chapter 5.

### **3.2.1 Detector Design Process**

It was decided at the start of the project that the detector would make use of gas electron multiplier technology. This detector is an ideal application for GEM technology due to the fact that GEMs excel in particle-tracking applications where both the location of particle interactions as well as the amount of energy deposited in the medium during the interaction need to be known. Standard GEM technology can provide two dimensions of special resolution, but since only one dimension is needed, the readout electronics are greatly simplified. Furthermore, GEMs are compatible with many types of proportional counter gas, including the tissue equivalent gas required by this experiment.

The role of the GEM in the detector is to provide gain in the signal produced by the interactions of the alpha particles. It is true that the GEM is not a strictly necessary

component in the envisioned experiment; however, even as densely-ionizing as they are, the ion pairs that single alpha particles create in the gaseous medium will produce only a very weak signal requiring exceedingly sensitive electronics to measure. GEMs provide large gains while still preserving both energy and position information which allows measurement with more conventional electronics.

While GEMs require specialized equipment to manufacture, they are readily available as off the shelf components. CERN sells inexpensive standardized GEMs with the caveat that only a non-commercial license is provided for their use. Furthermore, the modular nature of the available standard GEM foils combined with the relative simplicity of building a detector around them greatly eases development of the experimental apparatus. The remainder of the apparatus can be constructed with more conventional and widely-available techniques.

Several GEM frames were purchased from CERN prior to the beginning of the design phase. They came in the form of 74×74 mm square frames with the 50×50 mm sensitive foil area stretched across the center, screw holes for mounting in the corners, and a foil tab extending from one side for soldering electrical connections to it. Because the GEM frame was already decided upon, the detector needed to be designed around it.

For best results, the GEM needs to be operated in an environment with a gas of carefully-controlled composition and pressure. Therefore, the detector needed to incorporate a vacuum chamber that can be evacuated and filled with a proportional counter gas. Due to the expense and time needed to have such an enclosure machined, it was decided that the chamber used in Sipaj's experiment [10] would be reused for this experiment. The vacuum

chamber already had several threaded holes drilled in it for attaching threaded pipes or similar hardware. One hole was needed to connect gas filling apparatus while others could be used for electrical connections. Any unused holes were be capped off.

Therefore, the main design inputs going into the design of new components for the detector were as follows:

- The dimensions of the GEM frame
- The diameters and positions of the screw holes on the GEM frame
- The size and position of the solder tab on the GEM frame
- The size and position of the exposed foil on the GEM frame
- The internal dimensions of the vacuum chamber
- The diameters, positions, and threading type of the holes in the vacuum chamber

Taking those inputs into consideration, it was decided that the most efficient way to fit the necessary components and electronics into the vacuum chamber would be in the form of a 3-layer “stack” consisting of what was called the “main board” on the bottom, the “drift board” on the top, and the GEM frame in the middle. Figure 10 shows a diagram of the board stack as it was envisioned.

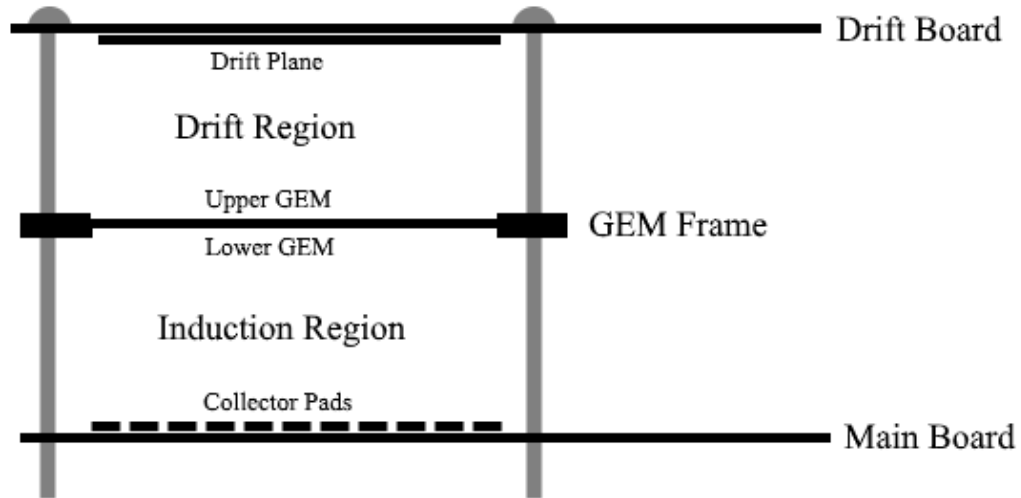


*Figure 10 - Stack Concept*

The main board is the surface where the collector electrodes necessary for GEM operation reside. The area between the collector electrodes and the bottom of the GEM's foil area forms the induction volume. Additionally, the main board is intended to hold all the active electronics that are necessary for detector operation. By keeping the electronics as close as possible to the collector pads, degradation of the relatively weak signals is minimized. The active electronics include a charge sensitive preamplifier as well as a multiplexer for selecting which of the pads is connected to the preamplifier. This arrangement allows for collecting data from only one pad at a time, but keeps the electronics simple at the cost of increasing the experiment's run time. This tradeoff is further discussed in the experimental methodology in Section 5.2, where the experimental procedure is described.

The drift board was also designed to serve multiple purposes. It is where the single large drift electrode resides. The area between the drift electrode and the top of the GEM's foil area forms the drift volume. It also has the resistor divider that sets the bias voltage for the

two sides of the GEM foil. The GEM will then be electrically-connected to the divider circuit via wires. During the design of the divider circuit, the high voltage that will be applied to the board will be decided upon. This will be influenced by the desired electric field strengths within the GEM foil, the drift volume, and the induction volume, as well as the separation of the boards.

In order to minimize attenuation of the alpha particles before they enter the sensitive volume of the detector, it was decided that the source would be positioned within the vacuum chamber itself. While this prevents easy changing of the source by sealing it in the gas-tight volume, it avoids attenuation of the particles through a solid window, such as the mylar window in Sipaj's experiment [10]. The board stack concept was envisioned such that the particle beam being measured would be centered both horizontally and vertically on the sensitive volume, so the source needs to be held in place. The particles need to be collimated into a beam as well so that particles at extreme angles do not enter the sensitive volume, so that all particles measured have a similar trajectory to minimize difference in distance travelled as they pass over the different pads.

To make the most efficient use of space, it was decided that the source holder and the collimator were to be designed as a single part that both holds the source and collimates the particles exiting it. The intended source of alpha particles for the experiment was selected at the start of the project. It was an  $^{241}\text{Am}$  source in a cylindrical form factor, with a diameter of 0.5 in and a height of 0.25 in. The radioactive material resides on one end of the cylinder in the form of a thin film. The source holder and collimator was therefore designed to hold this source.

With the board stack situated within the vacuum chamber, it was necessary for electrical connections to be made between the board and the outside world without disturbing the integrity of the vacuum seal. These connections needed to be made through existing threaded holes in the vacuum chamber. It was decided that plugs with electrical feedthroughs would be constructed that screw into the holes to complete the vacuum seal while still being removable for adjustments to be made or for the chamber to be repurposed for yet another experiment later.

Finally, the electrical connections needed to be connected with other equipment used in the experiment, such as high-voltage supplies and various detector-related electronics. It is generally preferable to use standard connectors rather than nonstandard ones or permanent connections so that existing cables can be used and so that connections can quickly be changed as needed without modification of equipment. Sipaj's experiment [10] used a two-piece metal enclosure that sat flush with one side of the vacuum chamber and held two BNC connectors, one SHV connector, and a 9-pin D-shell connector; it was decided that this enclosure would be reused. This enclosure was dubbed the "pod." The pod acts not only as a structural component, but as a shield as well.

### **3.2.2 Experiment Design Process**

Once the design of the detector was finalized, its geometry was known and fixed. This allowed for the selection of the fill gas and pressure. It was decided at the start of the project that propane-based TEG would be used because that was what was already in the laboratory. With the knowledge of the gas type, alpha particle energy, and the distance the alpha particles will need to travel to reach the end of the sensitive volume from the starting point, a gas pressure can be selected such that the particles are expected to come to a halt at the

end of the sensitive volume. This will allow for the measurement of the Bragg peak and surrounding area, which is found near the end of the particle's path.

Several additional pieces of equipment needed to be selected at this point. These pieces of equipment would reside outside of the detector and provide power, collect data, and aid in the diagnostics of issues that arise. During the design of the high voltage divider circuit on the drift board, the voltage that needs to be applied to it for proper operation of the GEM was decided upon; a high voltage supply was selected that can apply this voltage. A low-voltage power supply capable of supplying the power needed for the multiplexer and preamplifier within the detector was also needed. A multichannel analyzer needed to be selected to collect data from the output of the preamplifier, as well as to aid in interpreting that data. A test pulser was needed to supply test signals to the preamplifier, and an oscilloscope was necessary to examine preamplifier output for the expected signal shape. All of the pieces of equipment mentioned above are standardized items that are available off the shelf.

Finally, a system for generating the necessary pad selection signals needed to be built, as it was deemed easier to build a simple system for this purpose than to procure existing solutions. Two different functional selector pads were built. The first used a simple set of switches, with power provided by a 9-volt battery. However, it was later deemed preferable to perform the experiment remotely, so a computer interface was built that allowed a remote operator logged into the controlling computer to select pads without a physical presence.

Therefore, the requirements for the experimental apparatus are as follows:

- There must be a high voltage supply capable of furnishing a high negative voltage for the GEM's operation
- There must be apparatus capable of evacuating the gas and filling it with the tissue-equivalent gas.
- There must be a method for selecting the GEM pad that is currently under measurement.
- There must be a test pulser capable of testing the detector's internal CSP.
- There must be an MCA capable of measuring the output of the detector's internal CSP.
- There must be an oscilloscope for visual examination of the output pulses of the CSP.
- There must be a modular crate that provides preamplifier power for the detector as well as powers any modules that comprise any of the previous equipment.
- A computer capable of running the interface software for the MCA must be on hand for data collection.

Once all of the above work was performed and all of the above pieces of equipment procured, a round of tests and verification were performed followed by some adjustments as necessary. Once everything was found to be satisfactory, the specific procedure for executing the experiment was planned. The experimental procedure takes into account the

equipment that was gathered in the previous steps, which is why planning the procedure is the final step.

The gas filling apparatus did not need to be connected to the detector after filling it, so filling the detector was the first step that was performed. After that, the rest of the equipment was gathered in a locked room adjacent to the lab so that it will not be disturbed. This was preferable because of the long data collection times, which will be discussed further in Chapter 5.

## **Chapter 4. Detector Design**

The detector constructed for the experiment consists of a stack of printed circuit boards which are housed inside a vacuum-tight enclosure. In addition to serving as a surface for electrical connections and as a mounting for electronic components, the circuit board stack is used as a structural component and to define a sensitive volume in which the primary radiation interactions of the experiment take place in. In addition to acting as a gas-tight enclosure for the circuit board stack, the vacuum chamber has external connectors for both the communications and power connectors needed to run the experiment as well as the gas filling apparatus used to prepare the chamber's internal environment prior to the experiment. A photograph of the assembled detector is shown in Figure 11.

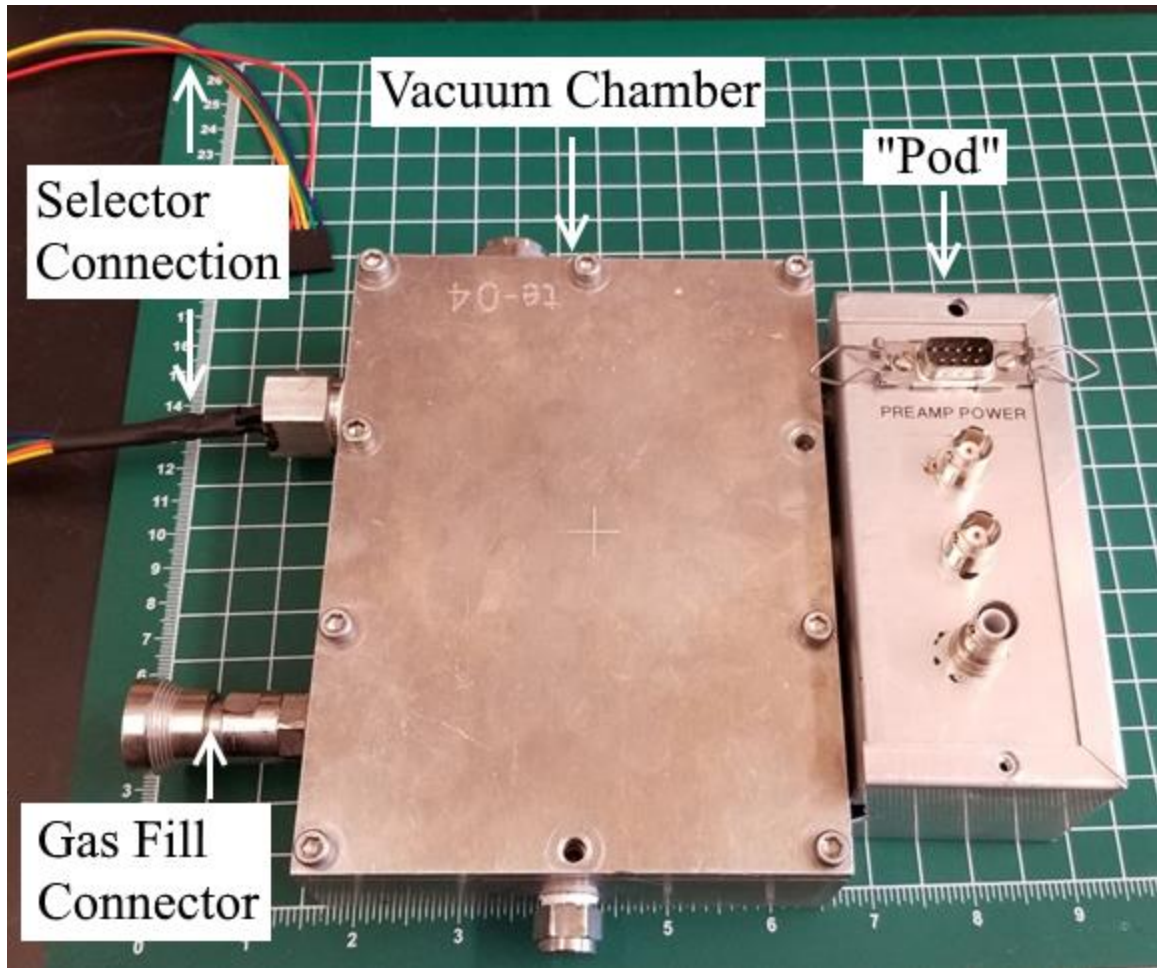


*Figure 11 - Completed Detector*

The circuit board stack, the vacuum chamber, and the components that comprise them are described in the following sections.

#### **4.1 Vacuum Chamber**

As the apparatus is designed around gas-filled radiation detector technology, the enclosure must be airtight. Due to the expense involved in having a custom chamber manufactured, the apparatus reuses an existing chamber that was made for a previous experiment. A photograph of the chamber with the lid removed is shown in Figure 12. This photograph

was taken during final assembly and depicts gas and electric feedthroughs in place and the unused ports capped off.

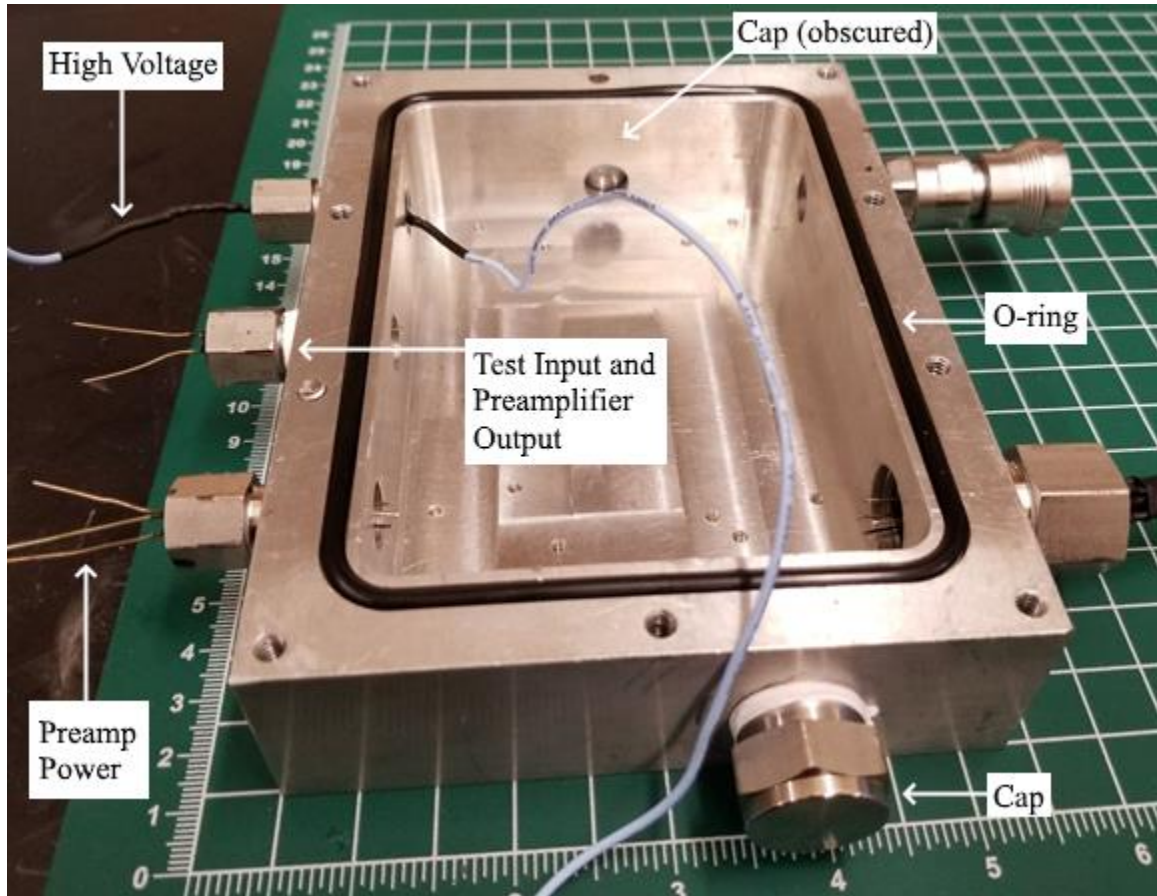


*Figure 12 - Open Vacuum Chamber*

The chamber consists of two machined aluminum parts, one of which forms the main body of the chamber while the other forms a lid. The main body has a slot for a neoprene O-ring which sits between it and the lid, aiding in the gastight seal. The lid is held on by 10 screws positioned at intervals around the edge.

Along the sides of the chamber are several threaded holes. These holes allow connections to be made between the contents of the chamber and external equipment. There are a total of two 1 inch and five 0.5 inch holes, each threaded in the American National Standard

Taper Pipe Thread standard, commonly referred to as National Pipe Taper or NPT. The tapered nature of NPT threads aids creating a tight seal when a male connector is screwed in.

The internal volume of the chamber was measured with calipers and determined to be 3.5×5.5×1.25 in with rounded corners. The rounding of the corners limited the volume usable by an object with a rectangular footprint, but a 3×5 in card comfortably fit inside the chamber when used as a guide. As a result, a 3×5 in footprint was used as a starting point for the design of the detector stack.

## **4.2 Circuit Board Stack**

The circuit board stack consists of three printed circuit boards held together in a three-layer “sandwich” by screws with separation provided by spacers. Photographs of a test fit performed prior to final assembly are shown in Figure 13 and Figure 14. This test fit was performed using a damaged GEM foil from a previous experiment so that it could be verified that the components fit without putting a working GEM foil at risk. The stack’s concept was described in Section 3.2.1 and a diagram of the concept was presented in Figure 10. The “Main Board” and “Drift Board” were designed and constructed for the experiment while the “GEM Board” was purchased from CERN.

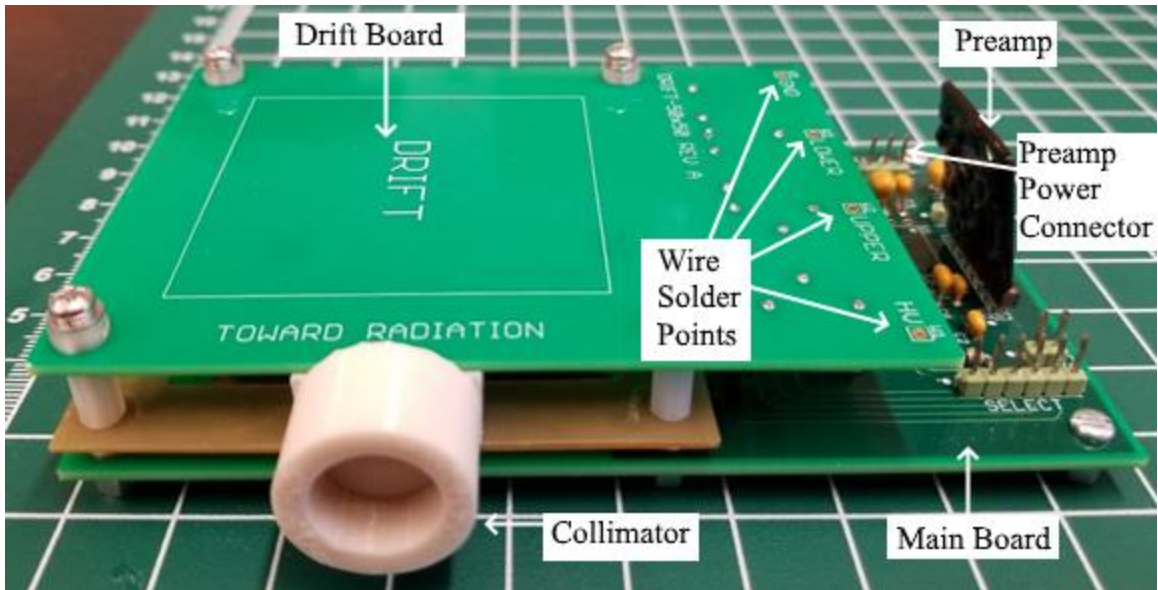


Figure 13 - Stack Test Fit

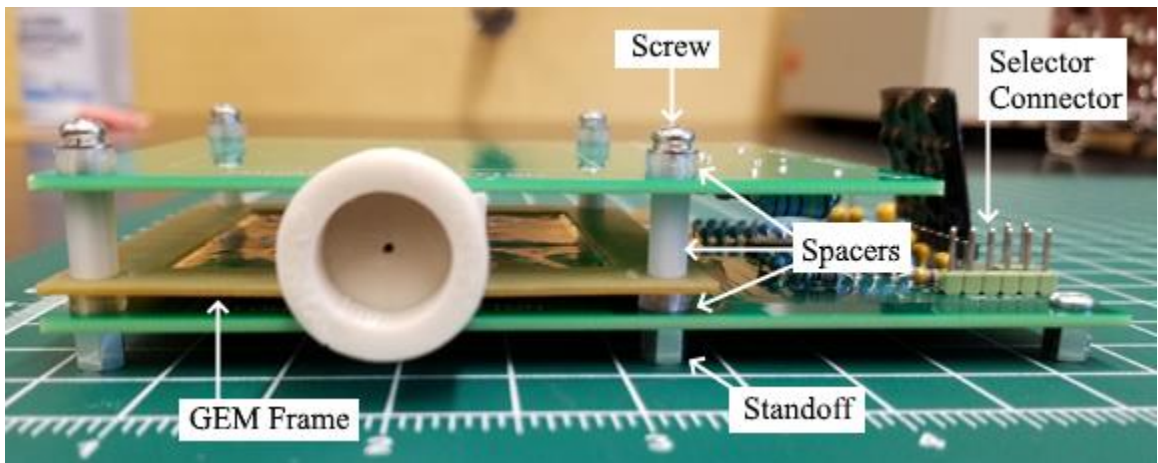


Figure 14 - Stack Test Fit, Side View

The stack of three circuit boards creates two special regions that are of great importance to the experiment. The area between the Drift Board and GEM Board is known as the “drift region.” This region is where the primary interaction between the radiation and the fill gas takes place; electrons liberated as the alpha particles cross through the region must be directed by electric fields towards the GEM board and into the GEM foil. The area between the GEM Board and the Main Board is known as the “induction region.” Electrons leaving

the GEM foil must be directed by electric fields towards pads on the Main Board where they are collected and measured.

The dimensions of the circuit boards constructed for the experiment were determined by taking into account two important factors that were outside of the control of the experiment. The first of these factors were the dimensions of the vacuum chamber. Because the vacuum chamber was made for an earlier experiment and reused for this one, its internal dimensions were fixed and represented maximum dimensions circuit boards. The second factor were the dimensions of the GEM board. Because the GEM board was purchased as a generic component, its dimensions needed to be accommodated.

As mentioned in the discussion of the vacuum chamber earlier, the starting point for the footprint of the circuit board stack was 3x5 in, or 76.2x127 mm. The GEM board was measured to be 74x74 mm, which comfortably fits within the 76.2 mm limit. To simplify the design of the circuit board layouts for both the Main Board and Drift Board, the width of the footprint was selected to be 74 mm in order to match the GEM. The slight reduction in width allows for a bit more freedom in the positioning of the board within the chamber, which later proved to allow lengthening the collimator discussed in Section 4.3. To match the aspect ratio of the original 3x5 in starting point, the maximum length of the board stack was selected to be 124 mm.

The separation between the boards were also selected by taking into account external factors. Similarly, the internal dimensions of the vacuum chamber determined the maximum allowable height for the board stack. Additionally, the high electric field strengths needed in both the drift and induction regions for proper operation of the GEM

are affected by the spacing between the boards, with smaller separations resulting in stronger electric fields. Finally, the vertical clearance in the drift region must be at least double the maximum expected range of delta rays produced by the beam of alpha particles travelling down the center line of the drift region in order to prevent loss of electrons to collisions with hard surfaces in the detector.

Using Equation 1 in Section 2.1.2, the maximum energy of delta rays expected to be liberated by the alphas was calculated to be only about 3 keV. Using NIST's ESTAR electron stopping power and range database [31], the electron range at this energy was so low as to be unavailable. Using the lowest value of 10 keV, the range at this energy was determined to be 4.11 mm as a beyond worst-case scenario. Therefore, the separation between the drift board and the GEM frame was selected to be 1 cm, as this is a round number well above double the electron range, with no risk of delta rays striking either the GEM foil or drift plane and losing their energy in a non-gaseous medium as a result.

The spacing of the induction region was selected to be 2.5 mm. This was fairly arbitrary, but it was considered preferable to have some spacing to limit the risk of contact between the GEM foil and parts of the main board, as the main board's electronics are not tolerant to high voltages.

Once the dimensions were arrived upon, a 3D representation of the stack was constructed in Siemens NX to get a feel for the scale before physical components were constructed. A render is shown in Figure 15. The collimator described in Section 4.3 is also attached. This model was placed within a 3D representation of the vacuum chamber in order to ensure that it would fit with adequate clearance.

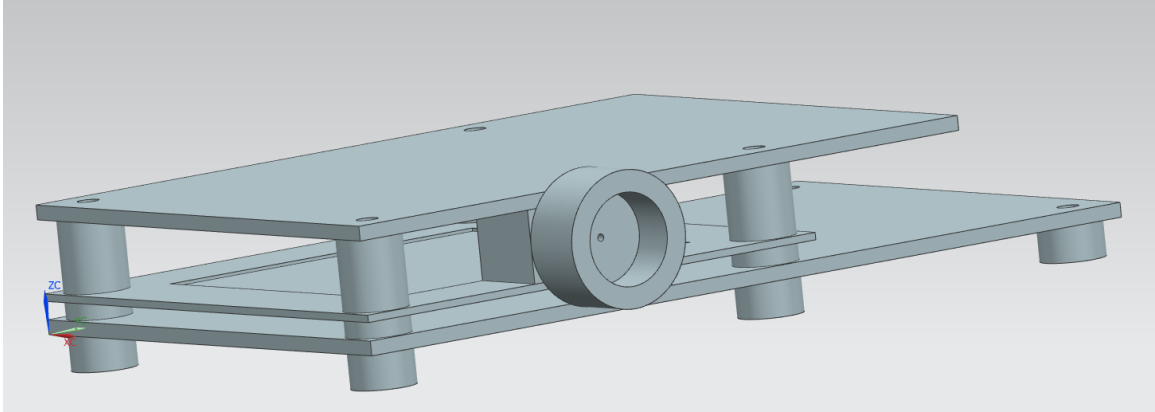


*Figure 15 - Render of Stack Concept*

To ensure that the geometry of the detector does not change if it is disturbed, the board stack was designed to firmly screw together. 25 mm long M3 screws were selected for this role. The spacing for the drift region was provided with 1 cm plastic threaded hex spacers, the spacing for the induction region was provided with 5 0.5 mm plastic washers, and spacing was provided between the bottom of the board stack and the bottom of the vacuum chamber with 5 mm aluminum threaded hex spacers. Additional washers were added between the head of the screws and the top of the drift board in order to “use up” the entire length of the screws so that the ends of them did not extend beyond the ends of the 5 mm metal spacers. A photograph of the final constructed board stack is shown in Figure 16.

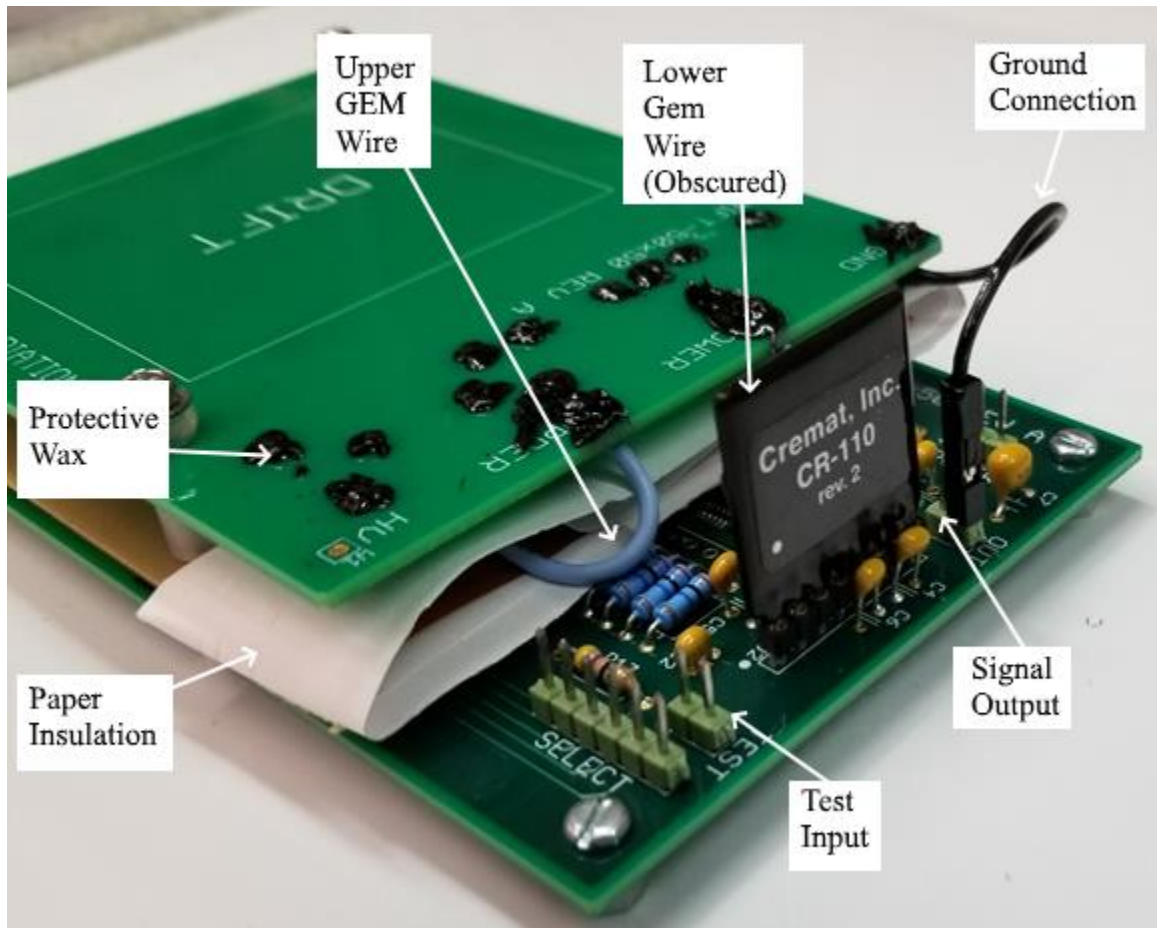


*Figure 16 - Final Stack Assembly*

Wax was applied to the solder points and exposed resistor leads on the drift board in order to provide protection against electrical arcing due to the high voltages involved. The wax used was Apiezon Wax W, a high-vacuum wax with low outgassing characteristics. For similar reasons, a piece of paper was secured with masking tape around the solder tabs of the GEM frame. Wax was not used on the GEM frame because the risk of getting it on the active part of the foil.

### **4.3 Alpha Source, Source Holder, and Collimator**

The alpha source that was selected for this experiment and the holder and collimator combination that was made for it are shown in Figure 17. The alpha source was

manufactured by Eckert & Ziegler medical; it is a 3.64 kBq  $^{241}\text{Am}$  source that is in a cylindrical form factor with a 0.5 in diameter and 0.25 in height. The americium consists of a thin film on one end of the cylinder. The thin film allows alphas to leave the source with a low amount of attenuation within it, ensuring that they have an energy as close to 5.49 MeV as possible upon exiting it. However, they exit it at random angles that are unsuitable for the experiment, as the experiment is predicated upon a beam of alphas entering its sensitive volume. Therefore, the alphas must be collimated to ensure that only the ones that exit the source on the desired trajectory make it out.

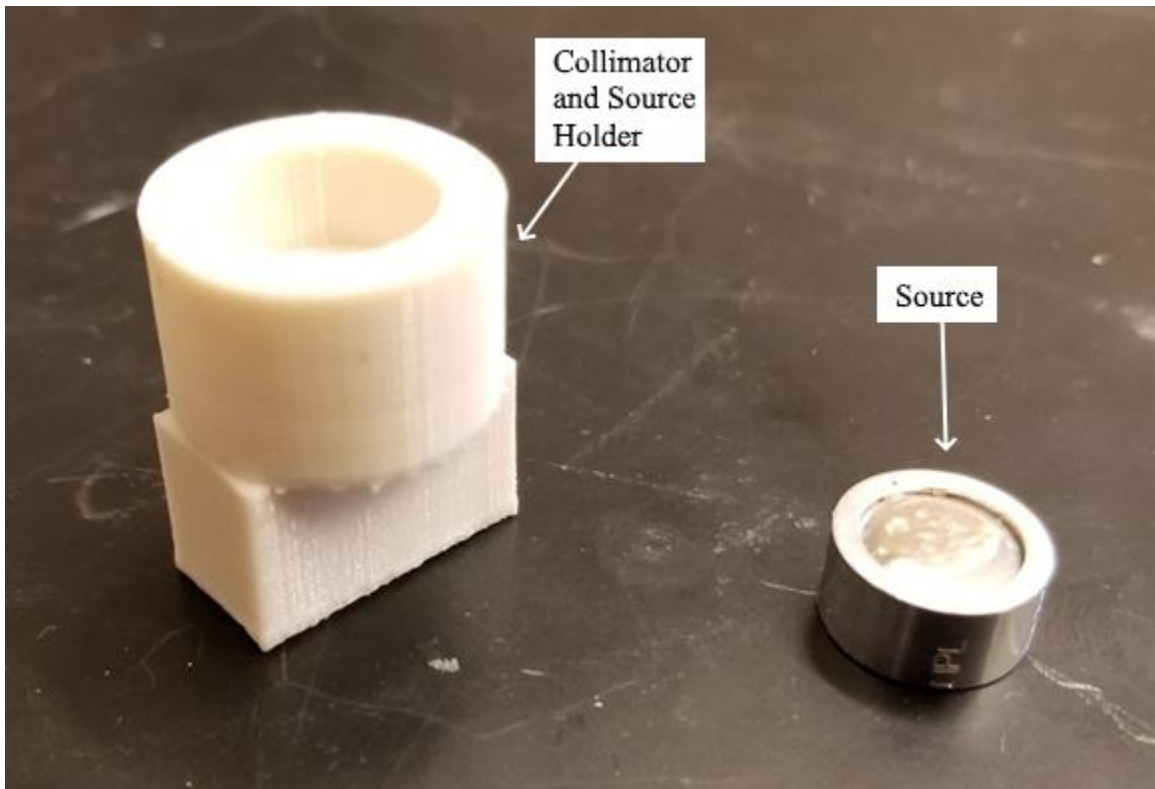


*Figure 17 - Collimator/Source Holder and Alpha Source*

The inner diameter of the circular portion that holds the source was selected to be 13.5 mm, slightly larger than the 0.5 in or 12.7 mm diameter of the source. It was deemed better to be too loose than too tight; the difference was made up with Teflon tape. The depth of the source cavity was selected to be 7 mm, rounded up from the 0.25 in or 6.35 mm length of the source. The assembly is held in place by a rectangular portion that fits between the drift board and GEM frame. This portion is 10 mm tall, matching the height of the space between the two boards, and is 20 mm wide, matching the outer diameter of the source holder.

The inner length of the collimator was selected to be 18 mm, which is as long as it can be while still fitting into the vacuum chamber. It is desirable for the diameter of the collimator to be as wide as possible to maximize particle fluence through it. However, this represents a tradeoff – widening the collimator results in particles being able to exit it at a more extreme angle. If particles exit at too extreme an angle, then they will strike the drift plane or the GEM foil instead of passing through the entire drift region. This situation is shown in Figure 18. The red line represents the most extreme possibility for a particle's angle upon exiting the collimator.

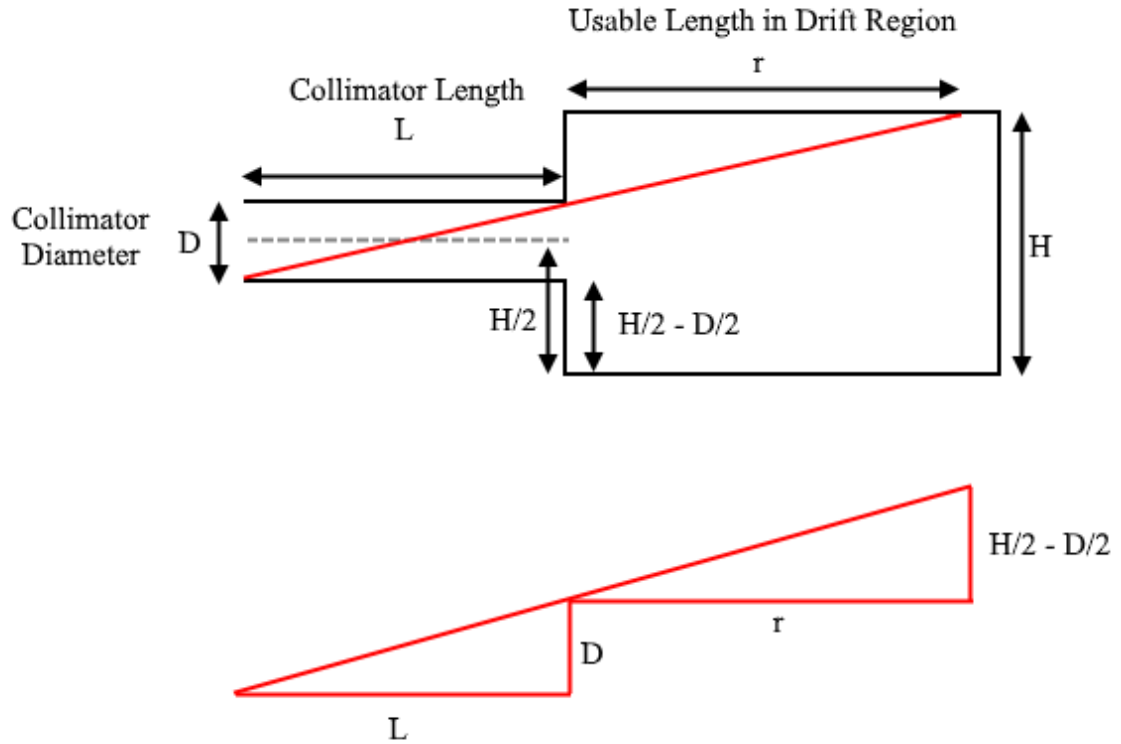


*Figure 18 - Collimator Parameters*

In Figure 18, D is the diameter of the collimator, L is the length of the collimator, H is the height of the drift region, and r is the maximum usable length of the drift region. H and L are already known, and are 10 mm and 18 mm respectively. D must be maximized without r falling below 50 mm, the length of the drift region.

Using trigonometry, the following relationship was arrived upon:

$$r = \frac{L(H - D)}{2D}$$

For a diameter of D = 1.5 mm, the maximum usable length of the drift region is determined to be 51 mm. Because this is greater than the actual 50 mm length of the drift region, there

is no risk of an alpha particle striking a surface before exiting the drift region. Therefore, 1.5 mm was used as the collimator's inner diameter.

The final collimator design was modelled in Siemens NX CAD software and 3D printed in PLA plastic.

#### 4.4 Main Board

The main board, situated at the bottom of the board stack, holds the majority of the detector's electronics as well as acts as the surface for the pads that collect electrons that exit the GEM foil. The electronics consist of a multiplexer and a preamplifier, power filter capacitors, and the necessary connectors. The final assembled board is shown in Figure 19.

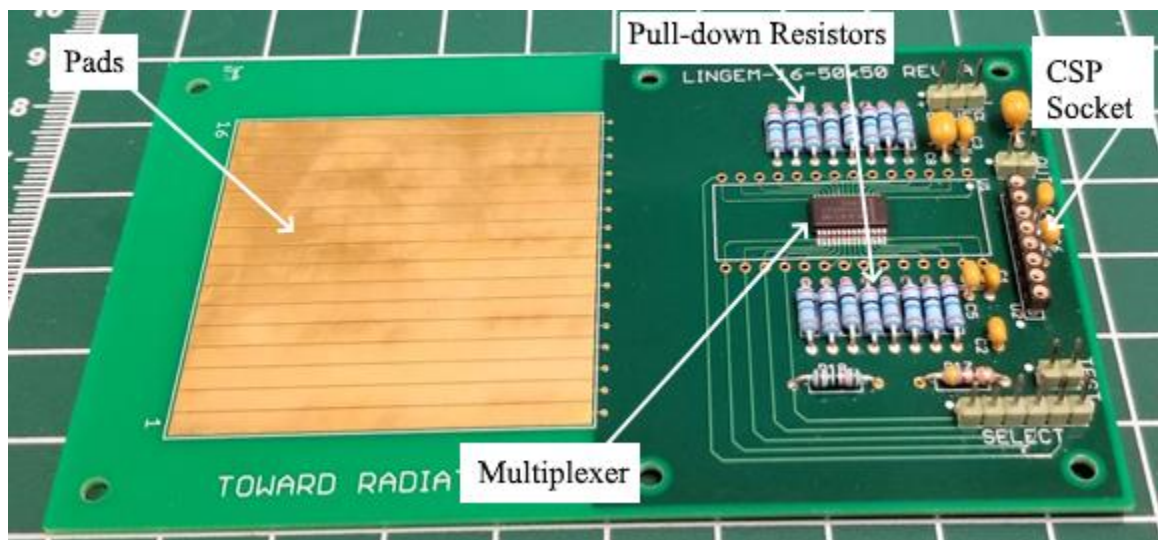


Figure 19 - Main Board

The electronics on the board require power to operate. The multiplexer and preamplifier both require positive and negative power “rails” to operate correctly. The rails on the board are connected to a power supply by a 3-pin 0.1 in pitch male pin connector that has connections for positive, negative, and ground potentials. For proper operation as designed,

+/- 12 V must be applied to the rails. While the specific power is not necessarily implied by the design, and in principle may be provided by any power supply, the intent was to connect the detector to a standard 9-pin preamplifier power connector that is typically found on NIM bins [3]; the specific NIM bin used in this experiment is described in Section 5.1.4. As per the standard [1], NIM bins have tight specifications on power supply stability, and 10  $\mu\text{F}$  and 0.1  $\mu\text{F}$  power supply decoupling capacitors are present on the board to further ensure quality of power. These aid in smoothing out power supply ripple or noise inducted into the cable [32].

#### **4.4.1 Collector Pads**

The “collector pads”, or simply “pads,” are a set of electrodes that represent the final endpoint of most of the electrons liberated within the gas by the primary ionizations caused by the passage of alpha particles, the secondary ionizations caused by the delta rays slowing down, as well as those further liberated during the gas multiplication process within the GEM foil. The pads are printed onto the circuit board itself as large pads similar to those used as solder points for surface mount components, and are made of gold-plated copper with no solder mask or silkscreening overtop. The pads are held at a potential of 0 volts, which represents the most positive potential in the path that the electrons travel through due to the negative high voltages used elsewhere. As a result, the electric fields within the induction region directs most electrons that exit the bottom side of the GEM toward the pads.

As discussed in Section 2.2.5, which contains a brief explanation of the Shockley-Ramo theorem, the act of collecting the electrons is not what causes current to flow. In fact, the signal begins to form as soon as electrons exit the bottom side of the GEM and begin

travelling toward the pads. As the mass of electrons is very small and the electric field within the induction volume is comparably strong, the electrons cross the volume and reach the pads very quickly, resulting in a fast-rising signal. The lack of a slow component to the signal caused by positive ions is considered to be one of the strengths of GEMs.

The total area of the collector volume is 50×50 mm, matching the active area of the GEM foil. It is further divided up into 16 discrete pads. Each pad's length is 50 mm, and are oriented to be perpendicular to the path of the alpha particles as they travel through the sensitive volume so that the particles cross each pad before they come to a stop. The widths of each pad were calculated with

$$W \times N + G \times (N - 1) = T$$

Where W is the width of each pad, N is the number of pads, G is the width of the gaps between the pads, and T is the total width of the whole set of pads. Solving for W, the equation arrived upon is

$$W = \frac{T - G \times (N - 1)}{N}$$

For N = 16, G = 0.1 mm, and T = 50 mm, the pad width works out to

$$W = \frac{50 \text{ mm} - 0.1 \text{ mm} \times (16 - 1)}{16} = 3.03125 \text{ mm}$$

In experimental calculations, the empty gaps between the pads is neglected and the simplified value of

$$W = \frac{50 \text{ mm}}{16 \text{ pads}} = 3.125 \text{ mm/pad}$$

is used instead.

The pads are pulled to 0 volts by 20 M $\Omega$  connected to ground. Because 0 volts is more positive than the potential of the bottom side of the GEM, electrons will be attracted to it. This resistor value was selected based on Sipaj's results in a similar experiment [10]. This resistor ensures that the pad returns to 0 volts shortly after the arrival of charge from an event. The collection of electrons charges the capacitor formed by the stray capacitance of the pad to a negative voltage, and the resistor subsequently discharges it back to 0 volts. Without the resistor, the pad would be at an indeterminate voltage and behavior would be unpredictable.

The schematic of the pads is rather simple and shown in Figure 20. The output of each one of the pad-resistor pairs is connected to a different input on the multiplexer, described next.

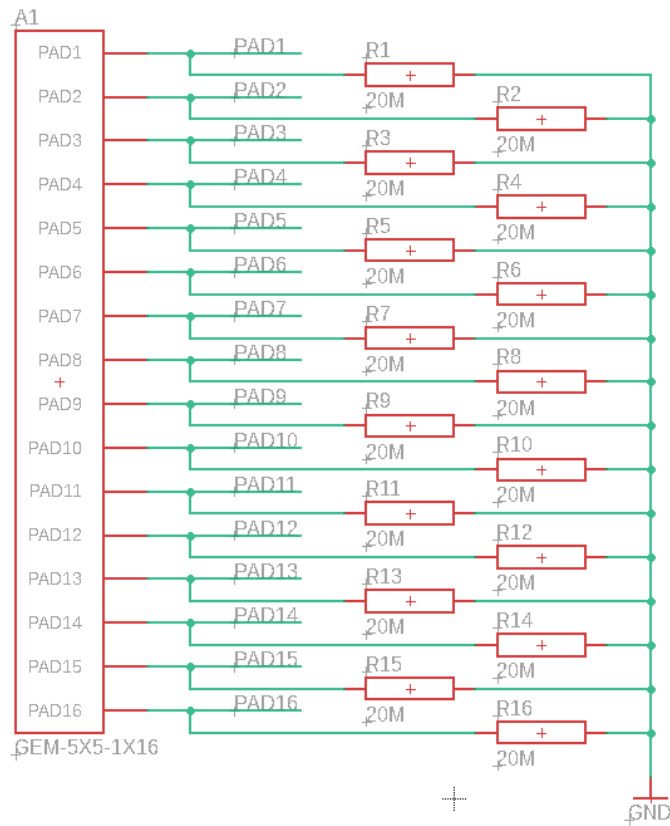


*Figure 20 - Pad Electrical Schematic*

#### 4.4.2 Multiplexer

A multiplexer was selected to serve the purpose of connecting the 16 collector pads described previously to the preamplifier described in the next subsection. Because 16 different inputs needed to be connected one at a time to a single output, a 16:1 multiplexer was used. The specific multiplexer that was selected for the detector was a Maxim Integrated MAX336 low-leakage analog multiplexer. This particular multiplexer requires very little supporting circuitry, as seen in the schematic in Figure 21. The only external component is a 10 k $\Omega$  pull-down resistor that disables the multiplexer in the absence of a signal.

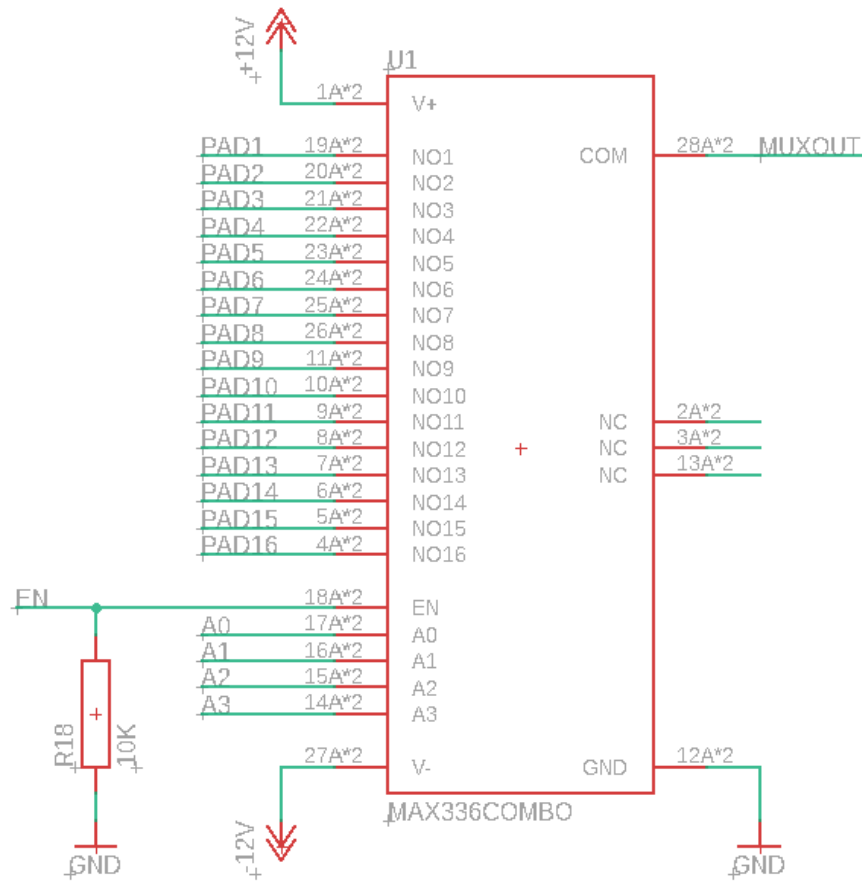


*Figure 21 - Multiplexer Section Schematic*

The MAX336 comes as a single integrated circuit in several different package types. Due to space concerns, the small surface-mount SSOP (Shrink Small Outline Package) was used rather than the much larger and easier to handle DIP (Dual In-line Package). The SSOP package represents the smallest package that the MAX336 is sold in, with a maximum specified height of only 1.99 mm, compared with the DIP's 5.08 mm height. This lower profile was necessary to fit within the 2.5 mm clearance between the main board and the GEM board as described in Section 4.2, which describes the circuit board stack. While the MAX336 was not situated under the GEM board directly, it needed to fit under

the GEM board's solder tabs, which have several centimeters of overhang and would have collided with the DIP version.

The MAX336 has 16 inputs, designated NO1 through NO16, and one output, designated COM. If the EN, or enable, signal is at logic low, the multiplexer is disabled and no signals pass through it; the connection between each input and the output acts as an open circuit. Conversely, if the enable signal is at a logic high, the multiplexer is enabled and a signal from one of the inputs is allowed to pass through; the connection between that input and the output acts as a closed circuit. The specific input that is connected to the output is selected by a 4-bit binary number provided to the multiplexer via signals A0 through A3. A 6-pin 0.1 in male pin header connector is provided to connect these signals to external equipment.

With each pad connected to a different input on the multiplexer, the current pad of interest may be selected by the experimenter through the use of simple logic signals. This means that the results from only one pad can be measured at a time, rather than measurements being taken from all pads simultaneously. This represents a tradeoff between complex electronics and data collection systems versus longer experiment run times, which was deemed more than acceptable for the experiment at hand.

The MAX336 was selected over other similar options due to its high performance in certain key characteristics compared to other similar parts, particularly less expensive ones. A particularly-notable parameter is the low leakage current and low capacitance of the multiplexer channels, which limit degradation of the small signals seen by the collector pads. Certain other characteristics of the part are worse than other similarly-priced parts,

such as the resistance between input and output channels being relatively high, but these were expected to have little or no effect on the intended application.

The logic signals that control the multiplexer are provided by hardware external to the detector called the “Pad Selector,” and are described in Section 5.1.9.

#### **4.4.3 Preamplifier**

The preamplifier selected for this experiment was the CR-110 by Cremat, Inc., a charge-sensitive preamplifier that is sold in a small 8-pin module form factor. The use of such a module greatly simplified the circuit design, as it could just be socketed in with only a bare minimum of support circuitry. Charge-sensitive preamplifiers such as this one are discussed in greater detail in Section 2.3.1.

The CR-110 has an operating voltage of  $\pm 6$  volts up to  $\pm 13$  volts, allowing it to be powered from the  $\pm 12$  volts provided by the NIM crate used to power the detector. It is the most sensitive variant in Cremat’s CSP line, with a maximum detectable charge per event of  $1.3 \times 10^7$  electrons.

The electrical schematic for the preamplifier section of the main board is shown in Figure 22. The supporting circuitry consists of a  $47 \Omega$  impedance matching resistor and 1 pF capacitor for the test signal hookup, and 10 nF DC blocking capacitor intended to help prevent high detector currents from saturating the detector, as described in the datasheet.

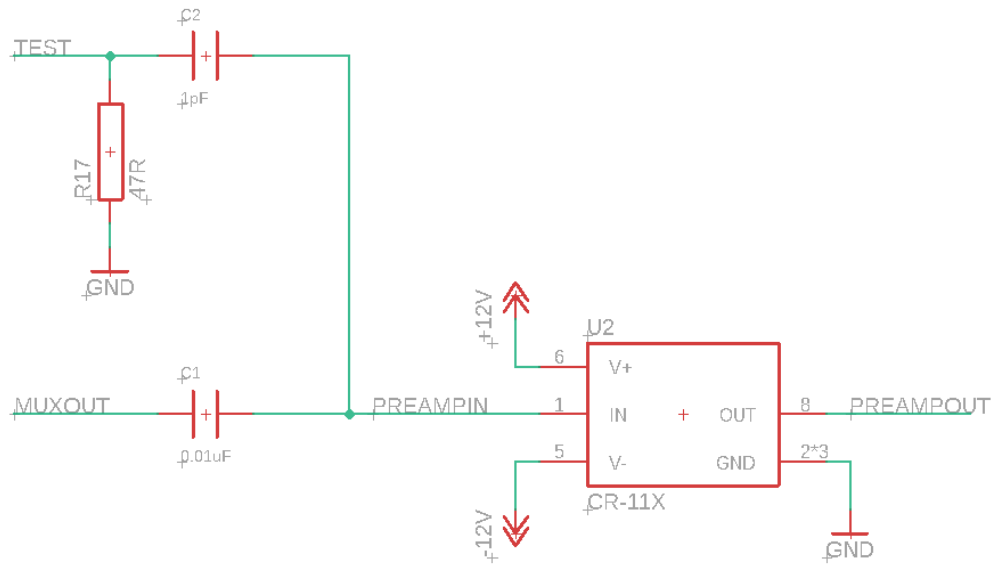


*Figure 22 - Preamplifier Schematic*

#### **4.5 GEM Frame**

The GEM board was not designed specifically for the experiment, but was purchased as an off-the-shelf component from CERN. As the organization that developed GEM technology, CERN holds patents on GEM technology and is the only authorized manufacturer of GEM products.

The particular GEM frame used in this experiment is the smallest off-the-shelf GEM that CERN sells, with an active area of 50×50 mm. Electrical connections can be made to the upper and lower sides of the foil via solder tabs that project from one side. The specific GEM frame used in this experiment is shown in Figure 23.

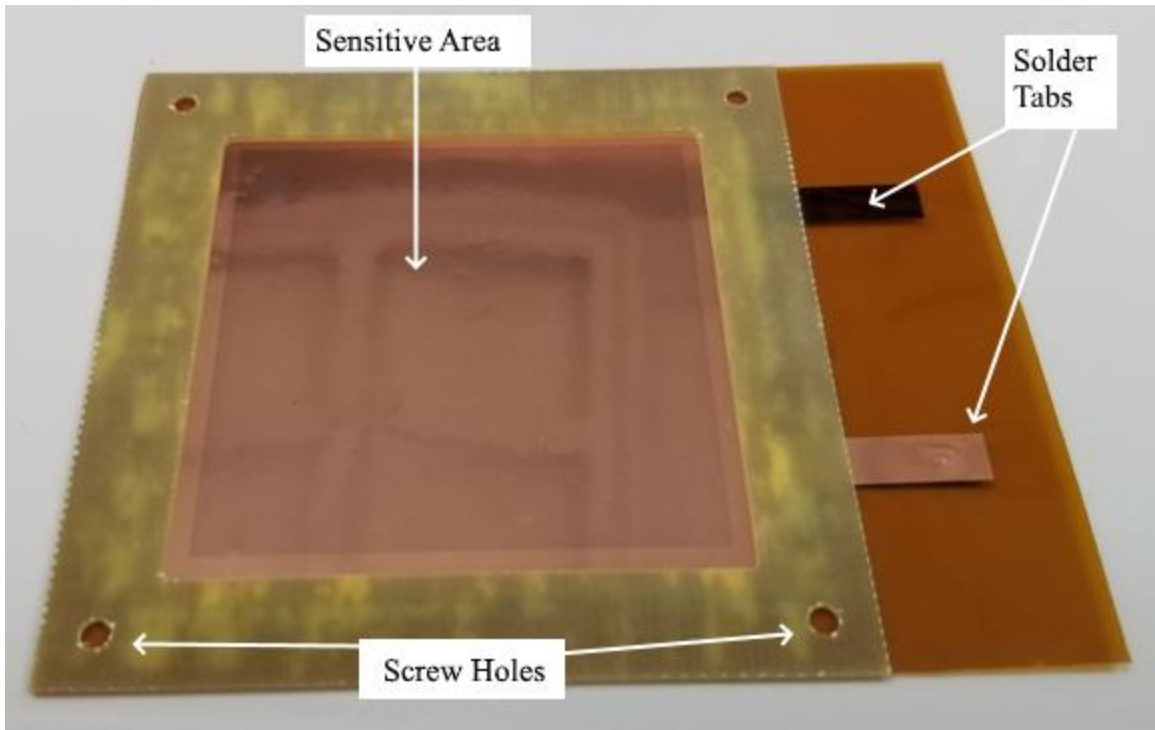


*Figure 23 - CERN Standard 50×50 mm GEM Frame*

#### **4.6 Drift Board**

The drift board, shown in Figure 24, is dominated by the 50×50 mm drift electrode. This electrode is held at the most negative potential in the detector, to ensure that electrons are repelled from it and toward the less-negative GEM foil. The rest of the board consists of a resistor divider and protection resistors. Four holes are provided for soldering wires; these are how the high voltage supply, ground, upper GEM, and lower GEM are connected to the board.

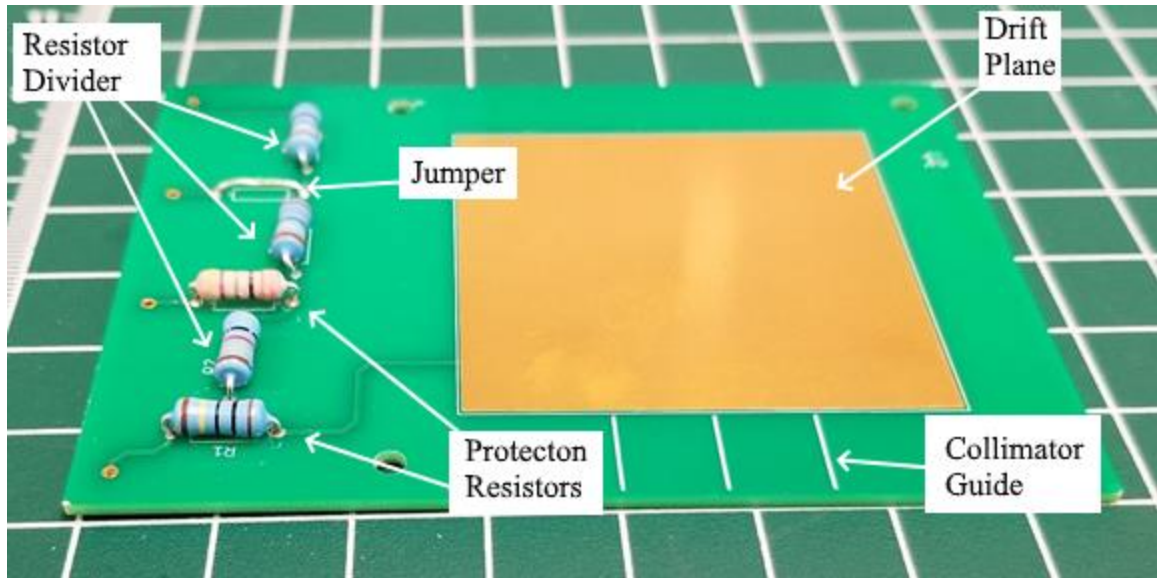


*Figure 24 - Drift Board*

The electrical schematic of the board is shown in Figure 25. Resistors R2, R4, and R6 form the divider while R1, R3, and R5 act as protection resistors. For reasons discussed later, R5 was jumpered over as it was found that populating it with a resistor would be counteractive to the protection of the GEM foil.

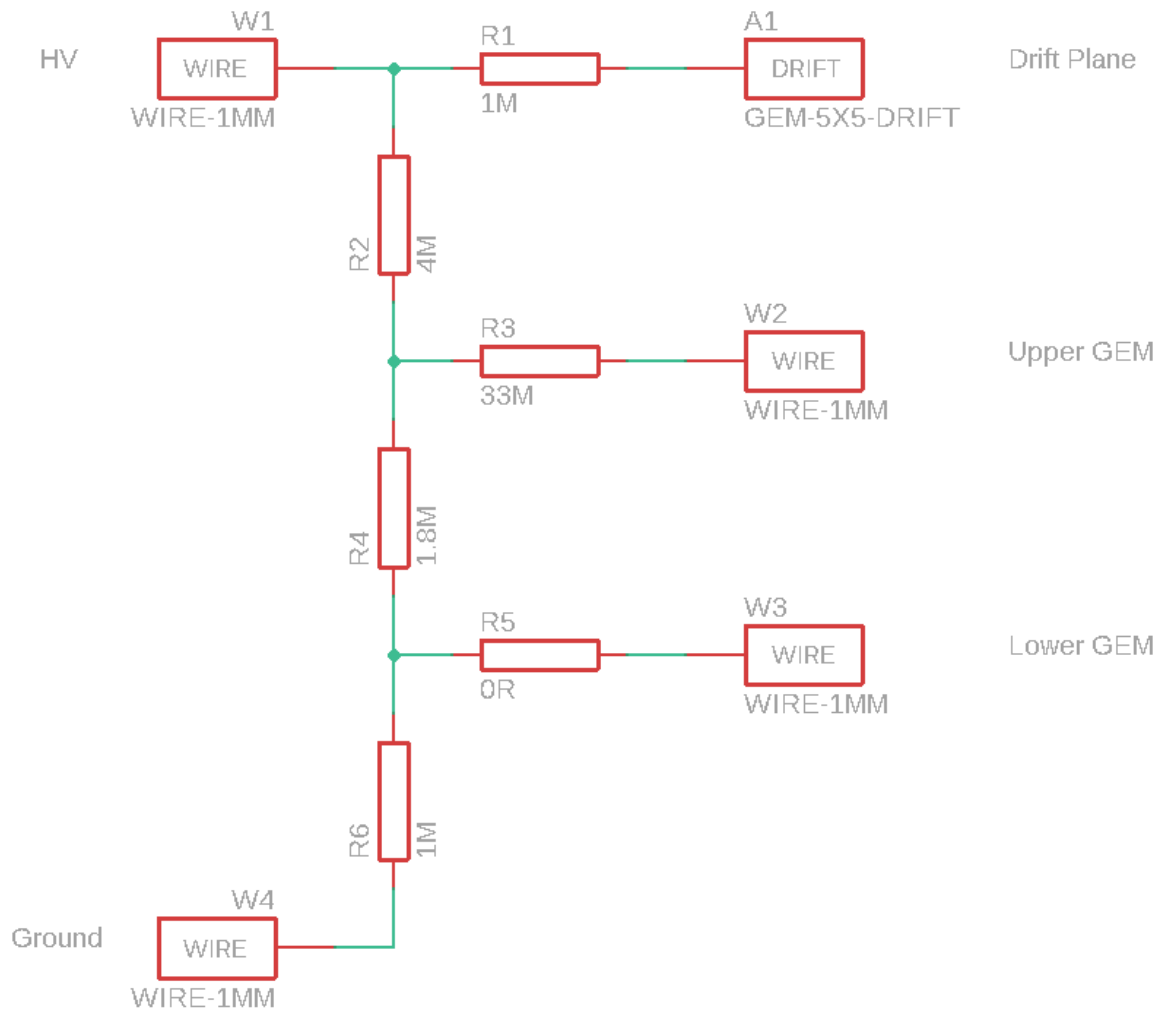


*Figure 25 - Drift Board Schematic*

Resistors R2, R4, and R6 must be selected to provide the required voltages to the upper GEM and lower GEM so that the required electric fields are maintained. It was found [33] that electric fields of about 1 kV/cm and 4 kV/cm are optimal in the drift region and induction region respectively. Sipaj [10] found that a voltage of 450 volts across the GEM was desirable.

To avoid excessively high voltages, it was decided that a lower electric field of 1 kV/cm would be used in the induction region to match the drift region. Because the drift and

induction regions closely approximate parallel plates electrode configurations, the voltage difference needed to create a resulting electric field given a particular separation is

$$\Delta V = |\mathbf{E}|d$$

Where  $|\mathbf{E}|$  is the magnitude of the electric field strength in volts/cm and  $d$  is the separation between plates in cm. With separations of 1 cm and 0.25 cm in the drift and induction regions respectively, the required voltage differences to achieve 1 kV/cm are therefore 1000 volts and 250 volts respectively. Including the 450 volt difference across the GEM, a voltage of  $-1700$  volts would need to be furnished by the high voltage power supply. Given the resistor configuration and a known supply voltage, the voltage on the upper side of the GEM is calculated by

$$V_{upper} = V_{HV} \times \frac{R_4 + R_6}{R_2 + R_4 + R_6}$$

And the voltage on the lower side of the GEM is calculated by

$$V_{lower} = V_{HV} \times \frac{R_6}{R_2 + R_4 + R_6}$$

Using these equations and some trial and error based on values of resistors for sale, the final values seen in the schematic were arrived upon. With a total series resistance of  $6.8 \text{ M}\Omega$ , the current draw of the divider is

$$I = \frac{V_{HV}}{R_{total}} = \frac{1700 \text{ V}}{6.8 \text{ M}\Omega} = 250 \mu\text{A}$$

And the power dissipated by it is

$$P = V \times I = 1700 \text{ V} \times 250 \text{ } \mu\text{A} = 425 \text{ mW}$$

Which, when spread across 3 resistors, should not require cooling and does not place demanding requirements on resistor specifications. In the final construction of the board, high voltage 0.5 W resistors from Vishay BCcomponents were used. Each resistor individually is rated for more than the total power dissipation of the divider and are rated for 3.5 kV so there is no risk of overrating the resistors in this configuration.

Protection resistor R1 is intended to limit the possible damage if an accidental short happens. Resistor R3 causes a voltage drop across the GEM if the current between the GEM sides due to high gas multiplication gets too high. By dropping the voltage, dangerous arcing is suppressed. It was decided to not install a resistor in R5's location and instead to install a short length of wire to short it, as a resistor installed there would potentially have the opposite effect and cancel out the benefit of R3.

#### **4.7 Feedthroughs**

A variety of electrical connections must be made between the board stack that sits inside the vacuum chamber and various pieces of equipment situated outside of the vacuum chamber. The points through which electrical connections breach the vacuum chamber are called "feedthroughs." The quality of the feedthroughs is important, as ingress of air will alter the composition and density of the gas within the chamber, thus affecting the results. Furthermore, O<sub>2</sub> gas such as that found in air is specifically identified as having the ability to negatively affect the performance of proportional counters even in small quantities, as it has a high preference for electron attachment, thus removing electrons that could otherwise contribute to the avalanche [3].

The feedthroughs used in this experiment were hand made using a non-standard method that was devised for this experiment. Purchasing ready-made feedthroughs proved to be a nonstarter, as the requirements for the feedthroughs needed for this experiment were so highly specific that no off-the-shelf solution existed. The main hindrances to procurement were the combination of NPT threading, the number of connections needed, and the low amount of space available for connectors.

The feedthroughs used off-the-shelf NPT reducing bushings as a base. Reducing bushings are normally used to allow larger pipes to connect to a receptacle designed for smaller pipes. Instead, “mushroom”-shaped wire guides were 3D printed that fit in the center of the bushings. These wire guides were made with equally-spaced holes for 21-gauge solid core wire. Wire was inserted through them, and then the wire guide was glued with cyanoacrylate glue (“super glue”) into place in the middle of the bushing. Once the glue set, both sides were filled with Apiezon Wax W, the same kind used as high voltage insulation in the assembly of the board stack. The assembled feedthroughs are shown in Figure 26.

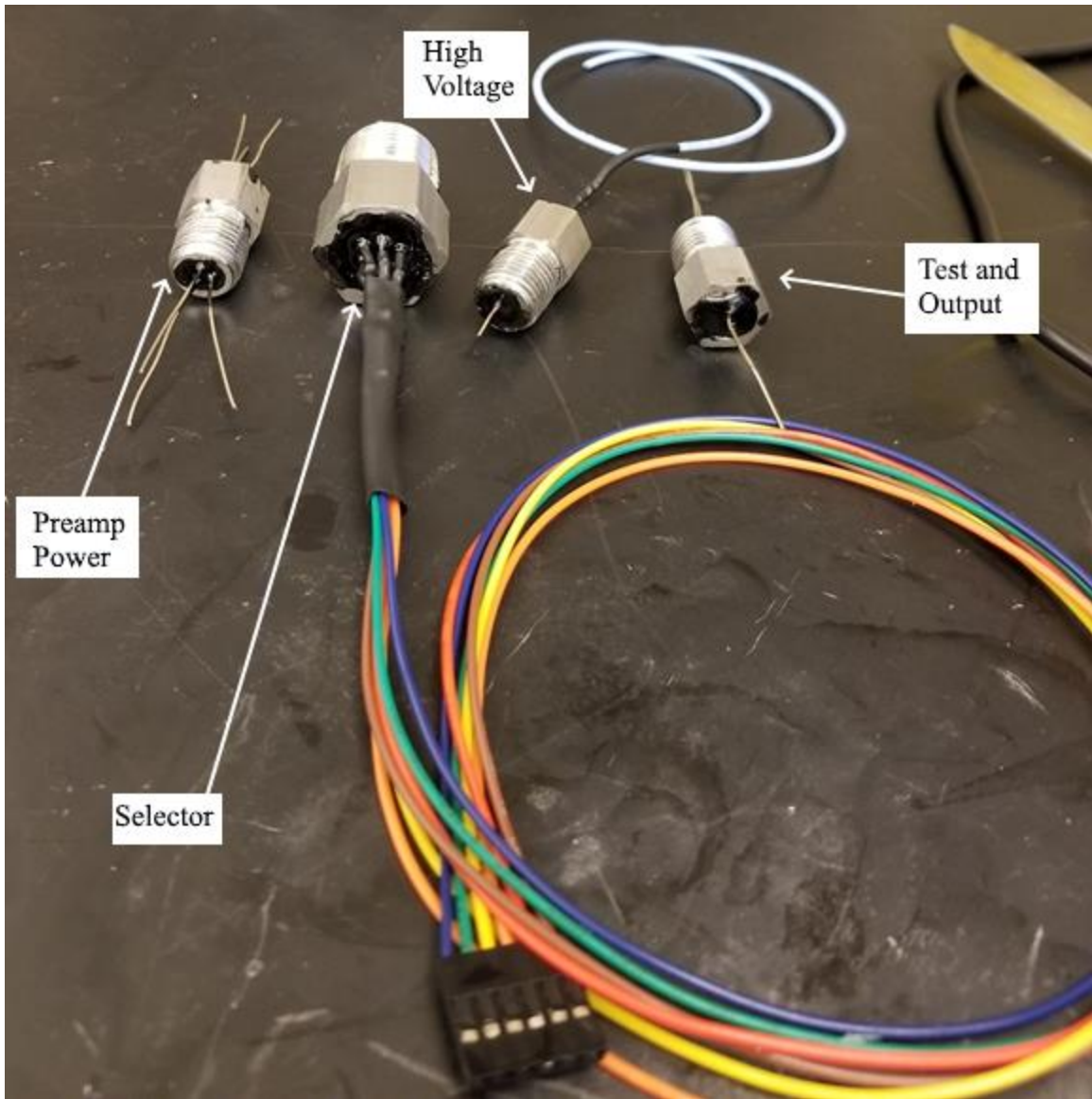


*Figure 26 - All Four Electrical Feedthroughs*

The interior connections for the low voltage feedthroughs were connected with removable rectangular connectors, as shown in Figure 27. This was intended to allow removal and adjustment without risk of damage. The high voltage feedthrough was designed with a single conductor so that risk of arcing or conducting to a low voltage signal was minimized. High voltage silicone rubber-sheathed wire manufactured by CnC Tech was used for the high voltage power. The particular wire used has a voltage rating of up to 3 kV. Instead of

attempting to create a removable connection, which opens up risk of arcing, the wire was soldered directly to the wire of the feedthrough and covered in heat shrink tubing.

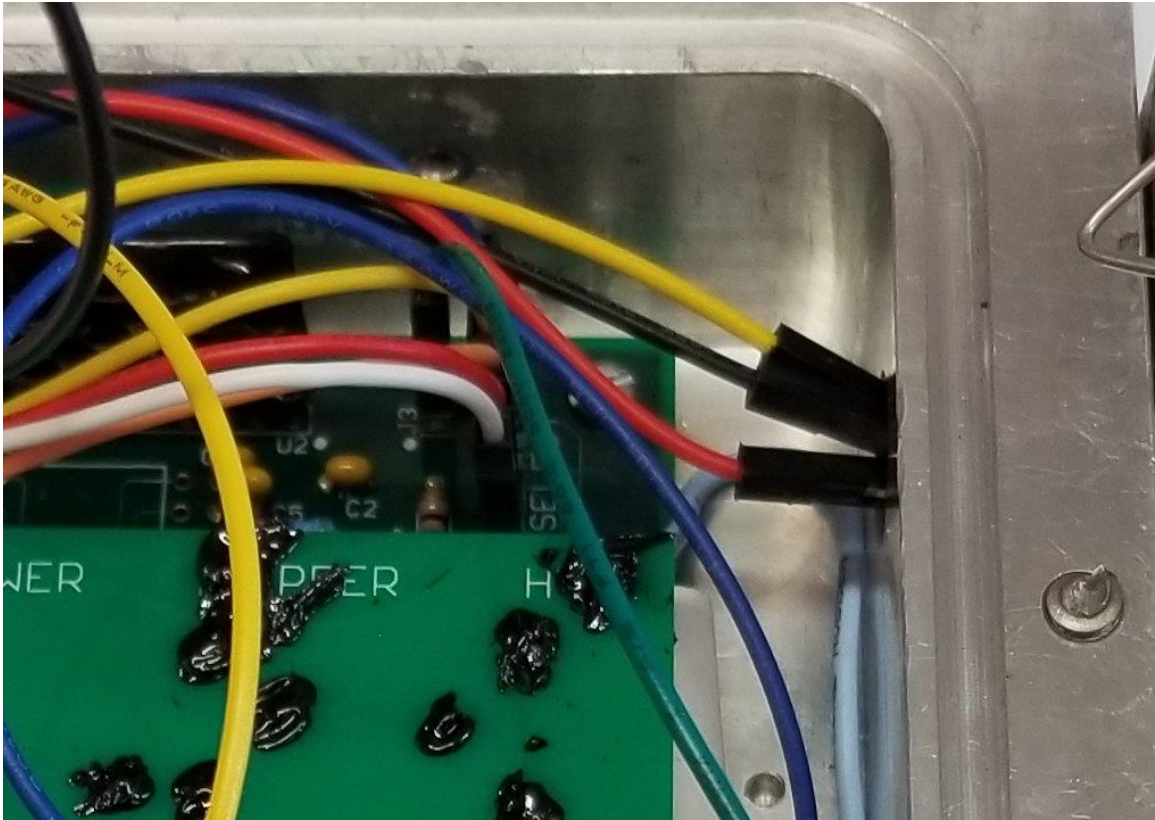


*Figure 27 - Interior Connections*

The feedthroughs proved to be rather good at maintaining the vacuum seal while having satisfactory electrical performance. However, during a test run of the experiment, it was discovered that the seal between the threads of the enclosure and the feedthroughs was leaky in spite of the use of Teflon tape. Apiezon Q sealing compound was used around the exterior of the threads as shown in Figure 28 in an attempt to solve this. Apiezon Q is intended for temporary repairs of vacuum systems, but it worked perfectly for the entire duration of the experiment. Once it was applied, there was no degradation of the gas

pressure or quality that was apparent in the collected data, which allowed for longer data collection times than previously planned.

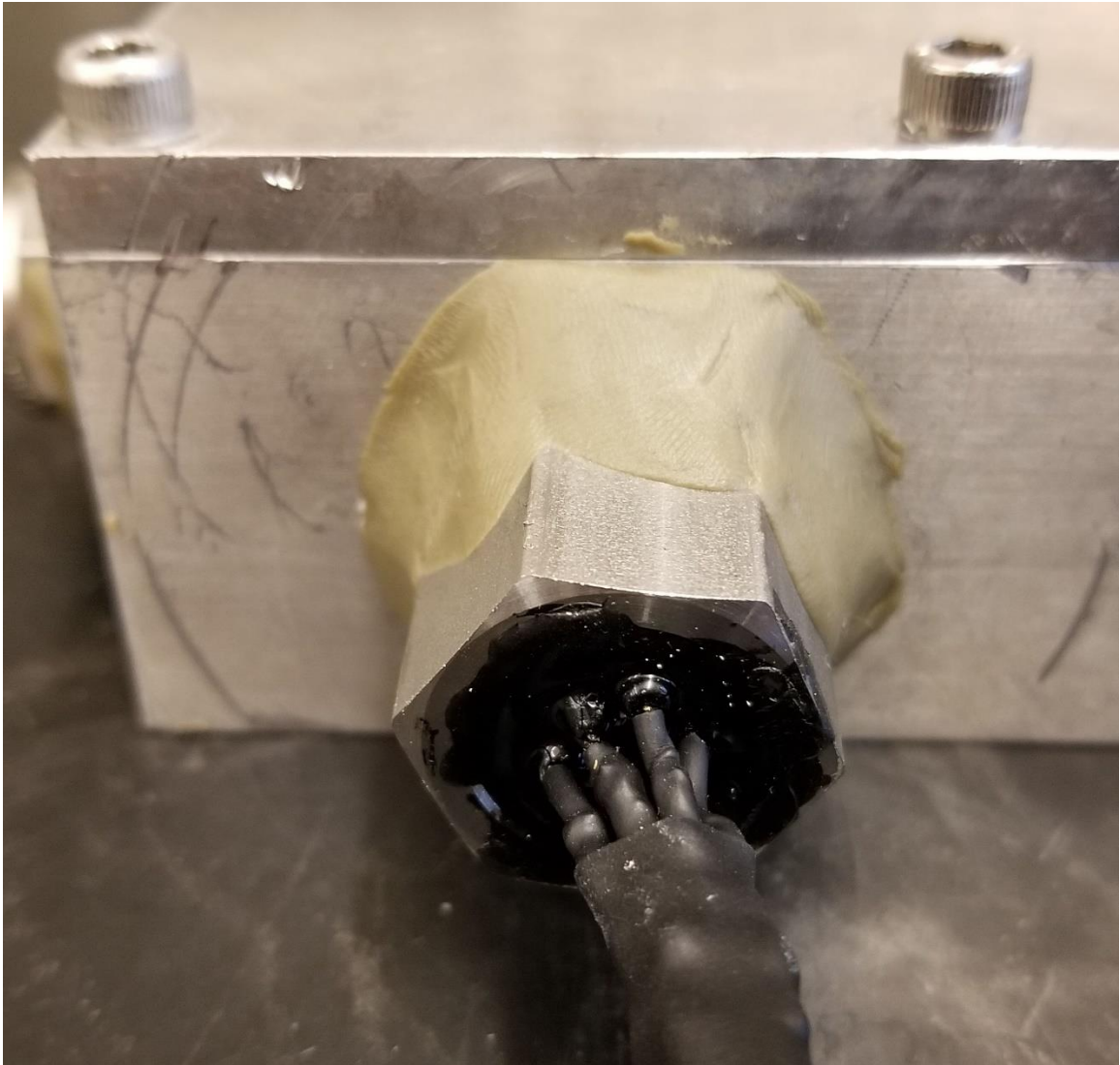


*Figure 28 - Selector Feedthrough Sealed With Apiezon Q*

## 4.8 External Connectors

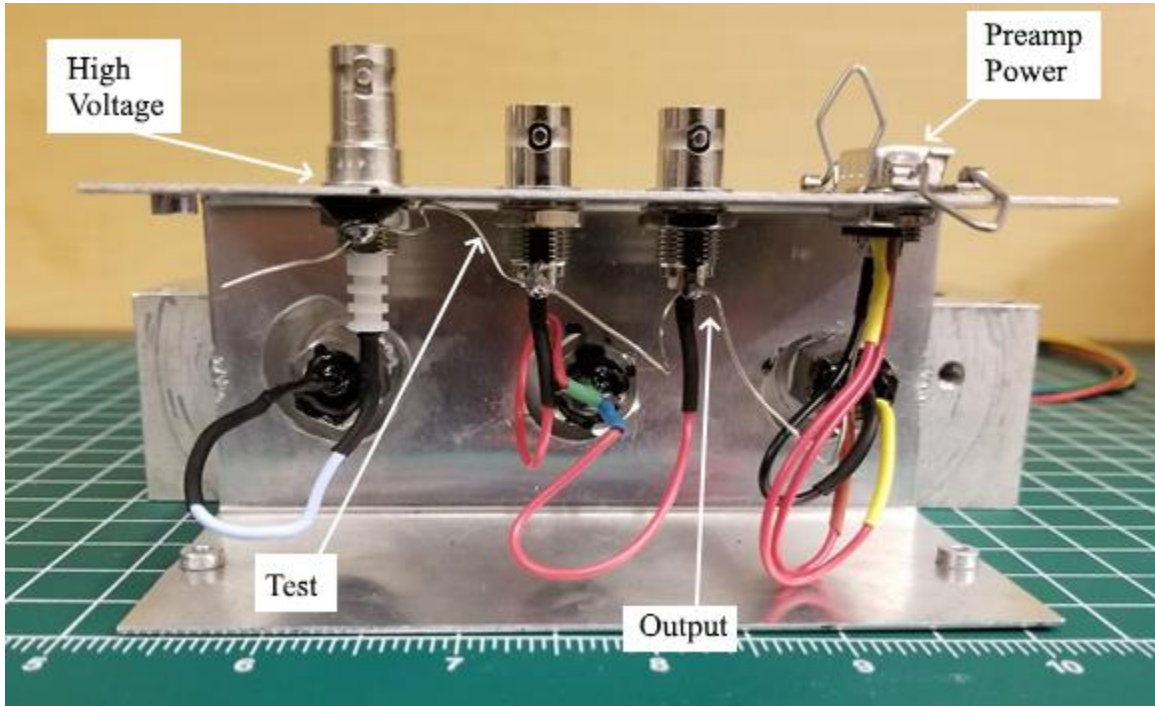


*Figure 29 - Inside of the "Pod"*

Most of the external connections were housed in the “pod,” a metal box attached to the side of the vacuum chamber. The interior of the pod is shown in Figure 29. The connections housed in the pod include the  $\pm 12\text{V}$  power provided by the 9-pin D-shell connector, test input and preamplifier output connections provided by BNC connectors, and high voltage provided by an SHV connector.

Once the feedthroughs were in place, wires were soldered onto their outer pins. The other ends of the wires were soldered onto the corresponding connectors. Heat shrink tubing was applied to reduce the risk of shorts. Once the connections were complete, the pod’s lid was secured to protect the connections and provide shielding from interference.

A different approach was used for the selector signals, because the position that was selected for the feedthrough they pass through was not within the pod. A six-wire cable

terminated in a 1×6 female connector was used; this cable is further discussed in Section 5.1.9, where the pad selector it connects to is discussed. The six wires on the end of this cable were stripped and soldered to the wires of the selector feedthrough. Heat shrink tubing was used to protect the exposed conductors. This is shown in Figure 30.



*Figure 30 - Exterior Pad Selector Connection*

## Chapter 5. Experiment Components and Methodology

### 5.1 Experiment Components

A great deal of support equipment was required for operation of the detector during the experiment. Figure 31 is a photograph of the experiment in operation. Toward the middle, the detector is placed on the benchtop. The pad selector is suspended above it using a retort stand, so that it may be visible by the laptop computer's camera for diagnostic purposes. The balance of the equipment is within the modular crate on the right, including the high voltage power supply, test pulser, and multichannel analyzer module.

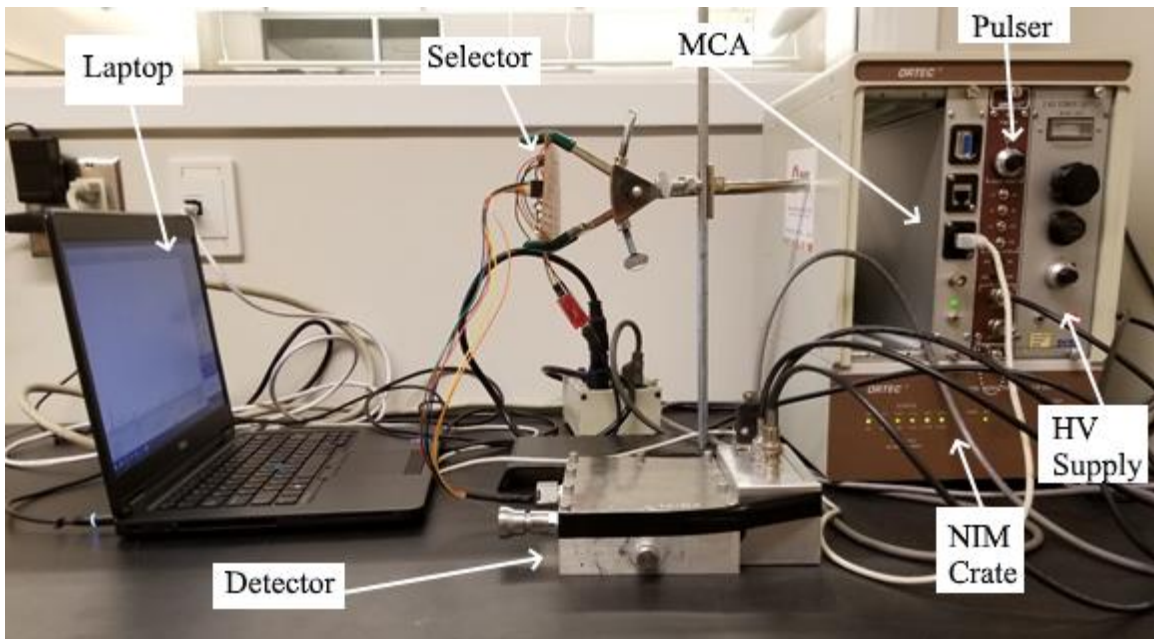


*Figure 31 - Experimental Apparatus*

Gas-filling equipment and an oscilloscope to prepare the experiment, but were not needed during operation of the experiment so they are not pictured.

These pieces of equipment are all described in this section.

### **5.1.1 Detector**

The design of the detector was described in Chapter 4. During the experiment, it resided on a bench in a side room for the lab so that it was not accidentally disturbed by other workers. This proved prudent due to the runtime of the experiment.

### **5.1.2 Gas Filling Equipment**

While the gas filling equipment did not need to be connected to the detector during operation, it played a key role in the preparation of the experiment. Figure 32 is a photograph of the equipment. It consists of a rotary vacuum pump, turbomolecular pump, several different forms of pressure gauges, a controller and display unit for the electronic gauges, connections to gas cylinders containing fill gases, and a hookup for the device being worked on. Several different types of gauges are required because they each cover different working pressure ranges.

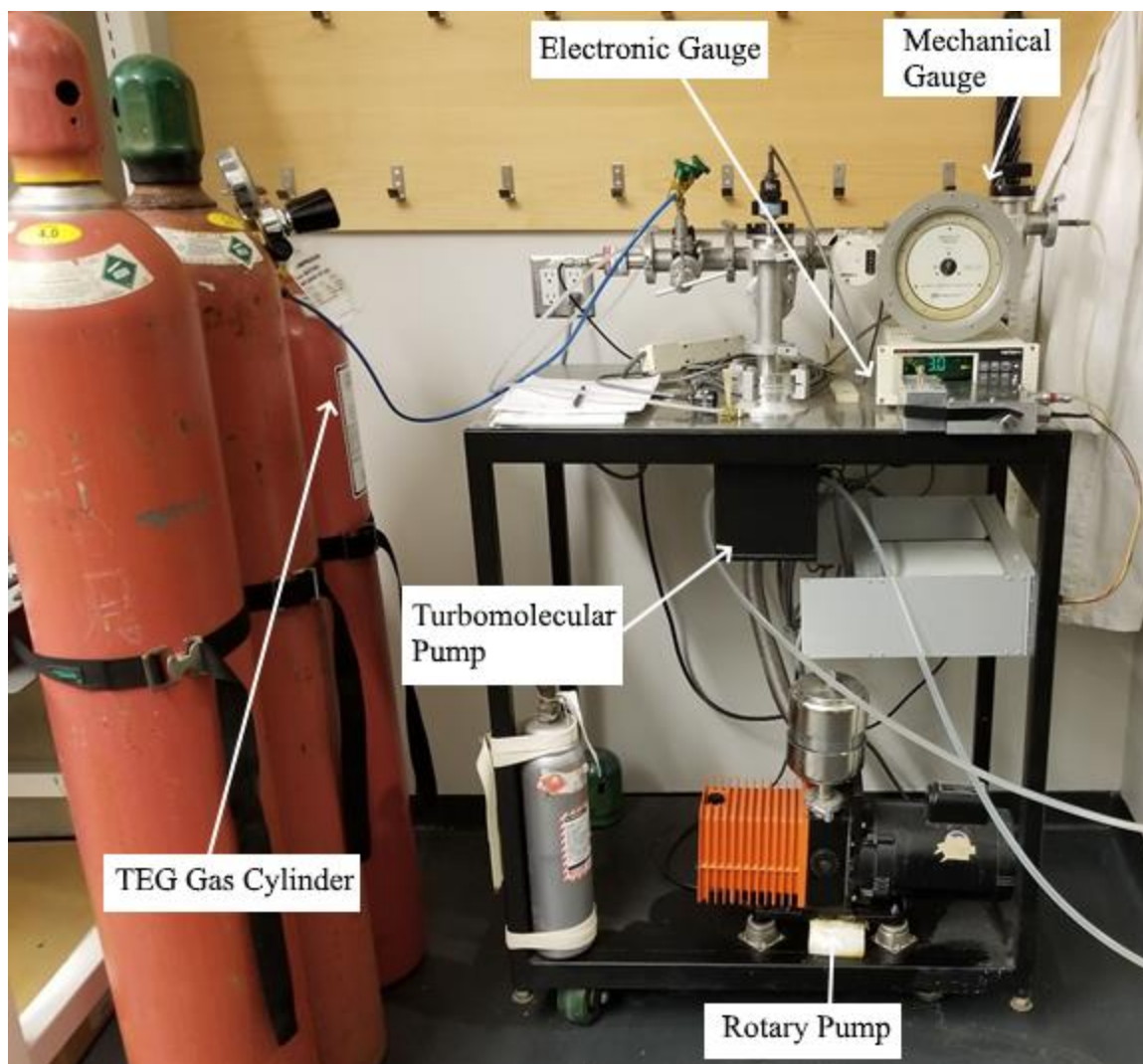


*Figure 32 - Gas Filling Equipment*

Once a device is connected, the rotary pump can be used to pump the pressure down to  $10^{-3}$  torr. Once there, the turbomolecular pump can be used to pump down to  $10^{-6}$  torr. The turbomolecular pump should be left running with the device hooked up for several days to allow outgassing to take place, so that actual leaks can be differentiated more easily from outgassing during leak tests. Once the device is pumped down and its leak rate is deemed to be satisfactory, it may be filled with gas. Valves can be adjusted to close the connection between the device and the vacuum pumps, and then open the connection between the device and the gas cylinder. A needle valve can then be used to finely-adjust the flow rate

of gas into the device. Once the pressure reaches the desired level, it can be closed. Finally, the device can be removed from the gas-filling apparatus and used.

### 5.1.3 Fill Gas

As previously mentioned, it had been decided at the start of the project to use propane-based TEG. Tissue-equivalent gas is discussed in greater detail in Section 2.2.2.

The  $^{241}\text{Am}$  source used in the experiment emits 5.49 MeV alpha particles, and it is desirable for as much of the particle's path as possible to be within the sensitive volume of the detector. Therefore, with a collimator length of 18 mm and a sensitive volume of 50 mm, the gas pressure must be selected such that the entire energy of the alpha particle is deposited within a distance of 68 mm. Or in other words, the alpha must have a range of 68 mm within the gas.

Using the SRIM, the average range of a 5.49 MeV alpha particle in unit-density ( $1 \text{ g/cm}^3$ ) propane-based TEG was calculated to be  $39.83 \text{ }\mu\text{m}$ . This should be roughly the range of the same particle within human tissue as human tissue has a similar density and composition [24], so this value was taken as such later in the experiment.

Because alpha particle range scales linearly with density [2], with a known range and density as well as a desired range, the density that provides that desired range can be easily calculated. The following equation from [24] can be used:

$$\rho_{det} = \rho_{tis} \times \frac{r_{tis}}{r_{det}}$$

Where  $\rho_{det}$  and  $\rho_{tis}$  are the densities of the gas within the detector and of tissue respectively, and  $r_{det}$  and  $r_{tis}$  are the ranges of the particles in the detector and in tissue respectively. Taking  $r_{det}$  to be 68 mm,  $r_{tis}$  to be 39.83  $\mu\text{m}$ , and  $\rho_{tis}$  to be 1  $\text{g}/\text{cm}^3$ , it was determined that the required density within the detector needed to be  $5.86 \times 10^{-4} \text{ g}/\text{cm}^3$ . Using this value in SRIM confirmed that a 5.49 MeV alpha should be expected to have a range of 68 mm in propane-based TEG.

Once the required density was known, it was necessary to determine the required gas pressure that would have the same density while at room temperature. This is simply an application of ideal gas law, which predicts that mass density increases linearly with pressure. The following equation from [24] can be used:

$$p_{det} = p_0 \times \frac{\rho_{det}}{\rho_0}$$

Where  $p_{det}$  and  $\rho_{det}$  are the pressure and density within the detector, and  $p_0$  and  $\rho_0$  are the reference pressures and density, assuming temperature is the same for both. Taking  $\rho_{det}$  to be the previously arrived upon value of  $5.86 \times 10^{-4} \text{ g}/\text{cm}^3$ , and the reference pressure and density to be 100 kPa and  $1.798 \times 10^{-3} \text{ g}/\text{cm}^3$  respectively at 20°C, a pressure of 32.6 kPa or about 244 torr. This pressure was used in the experiment.

#### **5.1.4 Modular Crate**

Several of the pieces of equipment used in this experiment are modules in the NIM standard form factor, described in [1]. In order to use them, they must be plugged into a NIM modular crate, which secures them in place as well as provides power to them. This arrangement reduces clutter in the workspace by concentrating the equipment in a small

footprint and by reducing the number of power cables needed [3]. Furthermore, NIM crates often include standard preamplifier power connectors of the type used by the experimental apparatus. Because they are used to power sensitive radiation detection equipment, NIM crates have stringent requirements for power supply stability, so it is assured that if a particular crate is functioning properly it will provide high-quality power to the equipment it is servicing.

The NIM crate used in this experiment was an Ortec model 4006 Minibin and Power Supply. It features six slots for NIM modules as well as two standard 9-pin preamplifier power connectors. While this particular model is on the small side for a NIM crate, it was more than adequate for the experiment at hand and was easier to move into position for the experiment than other options.

### **5.1.5 High Voltage Power Supply**

A high voltage power supply is required to operate the detector due to the high electric field strengths needed for proper operation of the GEM. As discussed in Section 2.2.4, GEMs require 3 different high voltages to operate; however, as discussed in the design of the detector in Section 4.6 where the design of the drift board was discussed, a simple resistor divider is used to bias the upper and lower sides of the GEM. The high voltage from the supply is applied directly to the drift plane electrode. Therefore, only a single high voltage needs to be supplied.

The detector was designed for  $-1700$  volts to be applied to it via a standard SHV connector. Many conventional gas-filled detector types do not require a voltage this high, and so many of the high voltage supplies in the lab were immediately found to be unsuitable. An older

supply, a Canberra model 3002, was found that fit the requirements. It has adjustable polarity and can be adjusted from 0 to 3000 volts. With an output current of 10 mA, it more than fit the requirements for this experiment. Its form factor is designed to fit in a NIM crate, consuming 2 slots, but this is just for space-saving purposes; it does not actually draw power from the NIM crate and instead plugs into mains power with its own cable.

#### **5.1.6 Test Pulser**

A test pulser allows the preamplifier to be tested in place, allowing one to ensure that the preamplifier is working correctly without disturbing the experiment. Test pulsers generate tail pulses of selectable amplitudes and polarities that simulate the output of a radiation detector [3]. By feeding these pulses into a designated input port of the preamplifier, the preamplifier can be tested even if the connected radiation detector is not currently in operation. In conjunction with a multichannel analyzer or an oscilloscope, the resulting output can be used to diagnose problems. This allows one to rule out the preamplifier as a source of issues in the event of unexpected output during the execution of the experiment, or even simply as a first test to verify that the preamplifier was installed correctly.

The test pulser used in this experiment is an Ortec model 480. As is fairly typical with test pulsers, it fits into and is powered from a NIM crate and has adjustable output voltage amplitude and polarity. The frequency and period of pulses, however, is fixed at 60 evenly-spaced pulses per second; however, this is adequate for ensuring proper operation of the preamplifier.

### 5.1.7 Oscilloscope

An oscilloscope allows visual examination of signals in terms of voltage as a function of time. This is an extremely powerful tool for examining the output from radiation detector preamplifiers, for diagnostic purposes as well as to determine important features of the detector such as charge collection time. The most basic way to test the operation of a preamplifier is to feed the output of a test pulser into it while examining the output with an oscilloscope in order to ensure that the output is as expected; a malformed pulse or none at all can be an indication of problems with the preamplifier [3].

The oscilloscope used in this experiment was a Tektronix model TDS 2002B, shown in Figure 33. It is an older but adequately-capable digital oscilloscope that served the needs of the experiment.

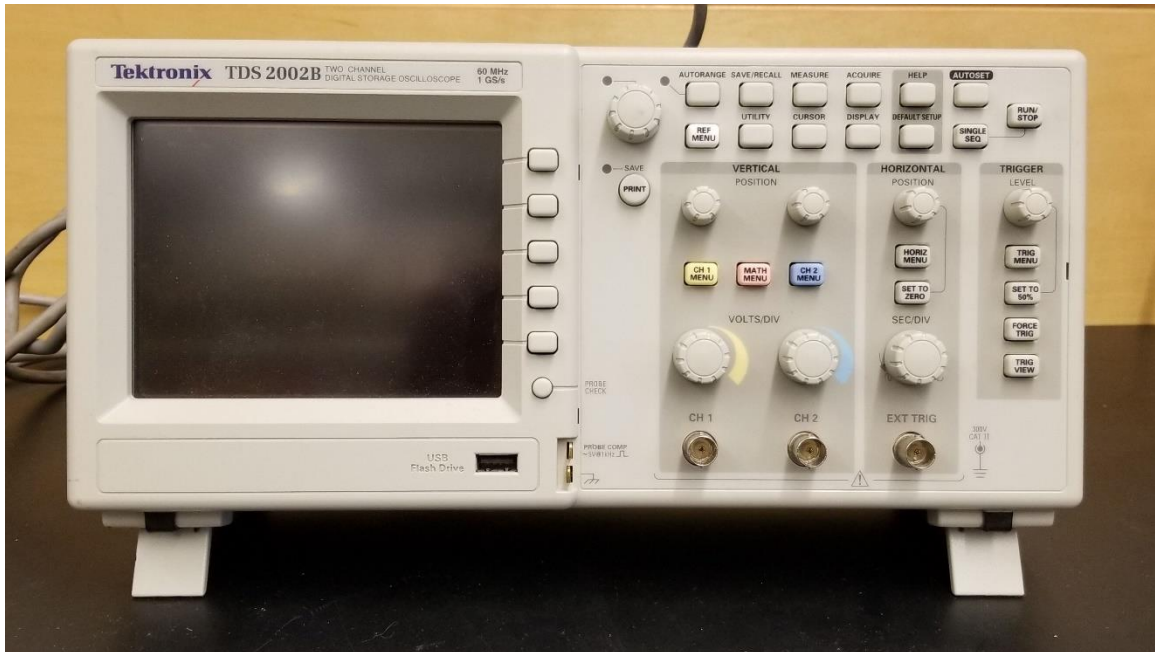


*Figure 33 - Oscilloscope*

### **5.1.8 Multichannel Analyzer**

The MCA processes and measures the signal from the preamplifier. The MCA used in this experiment is the DP5, a digital pulse processor (DPP) and MCA board manufactured by Amptek. It was housed in a custom-made NIM module, pictured in Figure 34, allowing it to fit into and be powered by a NIM crate, thus reducing clutter and cables in the workspace. It has a BNC connector on the back for the signal input from the preamplifier contained within the detector, and an additional BNC connector on the front for a signal output for diagnostic purposes. It interfaces to a computer with the user's choice of USB, Ethernet, or RS-232 serial port. For this experiment, it was connected to a laptop computer with the USB connection.

The DP5 is a high-end device that is highly configurable. As a DPP, it is capable of being reconfigured in software due to all the signal processing being purely digital. During the testing phase prior to running the experiment, the use of a test pulser connected to the preamplifier input and an oscilloscope connected to the output of the DP5 aided in selecting shaping and pulse counting settings. Figure 34 shows the DP5 board inside the NIM module it resides in.



*Figure 34 - DP5 Board Within NIM Module*

### **5.1.9 Pad Selector**

As discussed in Section 4.4, which describes the design of the main board, the detector has 16 “pads” which collect the electrons that exit the bottom of the GEM foil. These pads are connected to the multiplexer which is used to select which of the 16 pads is currently being used to take measurements from. The control of the multiplexer requires several logic signals; these signals are generated by the pad selector.

A total of 6 electrical connections must be made with the detector to select the current pad. One signal enables the multiplexer, four signals provide it with a four-bit binary number that selects which of the 16 pads is currently selected, and, because the signals are single-ended, a ground return is required. The signals are routed directly to the inputs of the multiplexer, which is designed to accept  $<0.8$  V as a logic “0” and  $>2.4$  V as logic “1.” The detector was designed with a 6-conductor cable terminated with a  $1 \times 6$  female connector

for 0.1” pitch pin connectors, allowing it to be connected to different devices for selecting pads. This proved to be useful, as two different schemes were evaluated.

Figure 35 is a photograph of the first pad selector that was built. It consists of a piece of stripboard with a row of DIP switches, several 10 K $\Omega$  pull-down resistors, and a connector for a 9-volt battery. The use of a battery was considered acceptable due to the exceedingly-low current draw presented by the pull-down resistors and the logic inputs, and has the added benefit of simplifying the apparatus by not requiring an additional power supply. Using a battery also reduces potential sources of noise in the experiment because of the high stability of battery voltages.

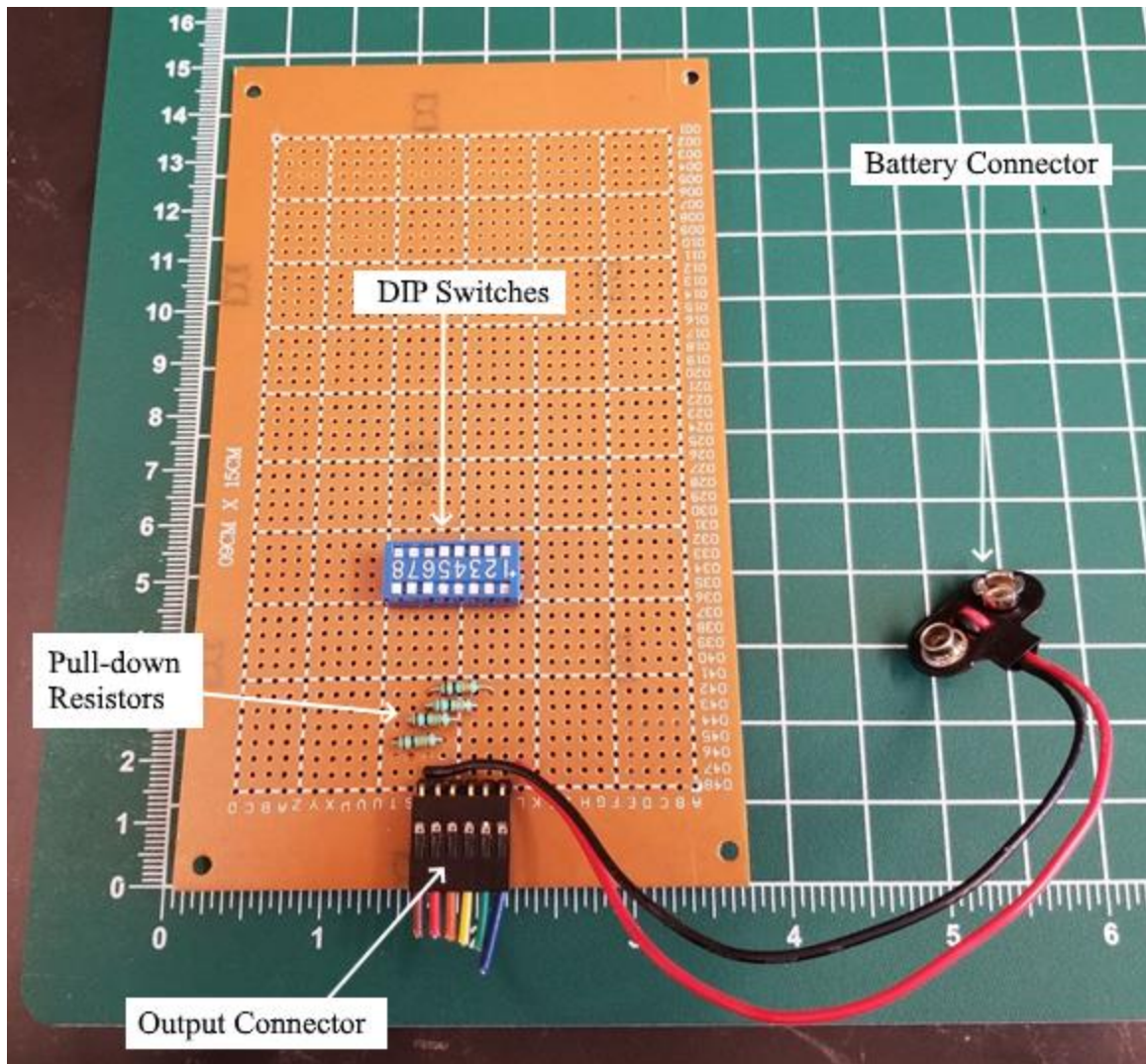


*Figure 35 - First Selector*

This pad selector worked adequately and was used during the testing process of the detector. However, it had a downside in that the experimenter needs to be present in order to adjust the physical switches on it. It was later decided that due to the long running times and the need to switch pads regularly, a new pad selector with a computer interface would be constructed in order to allow the experiment to be performed remotely.

Figure 36 is a photograph of the second pad selector, which was used in the final experiment. It was designed to connect to a computer via USB, which it uses for both power

and communication. Because of the relative difficulty in creating original USB devices, a small board with an FT232R USB-to-serial converter chip manufactured by FTDI was used. It acts as the link between the computer and a new interface board that was constructed which was designed to accept serial commands and output the corresponding parallel signal that the multiplexer is able to accept.

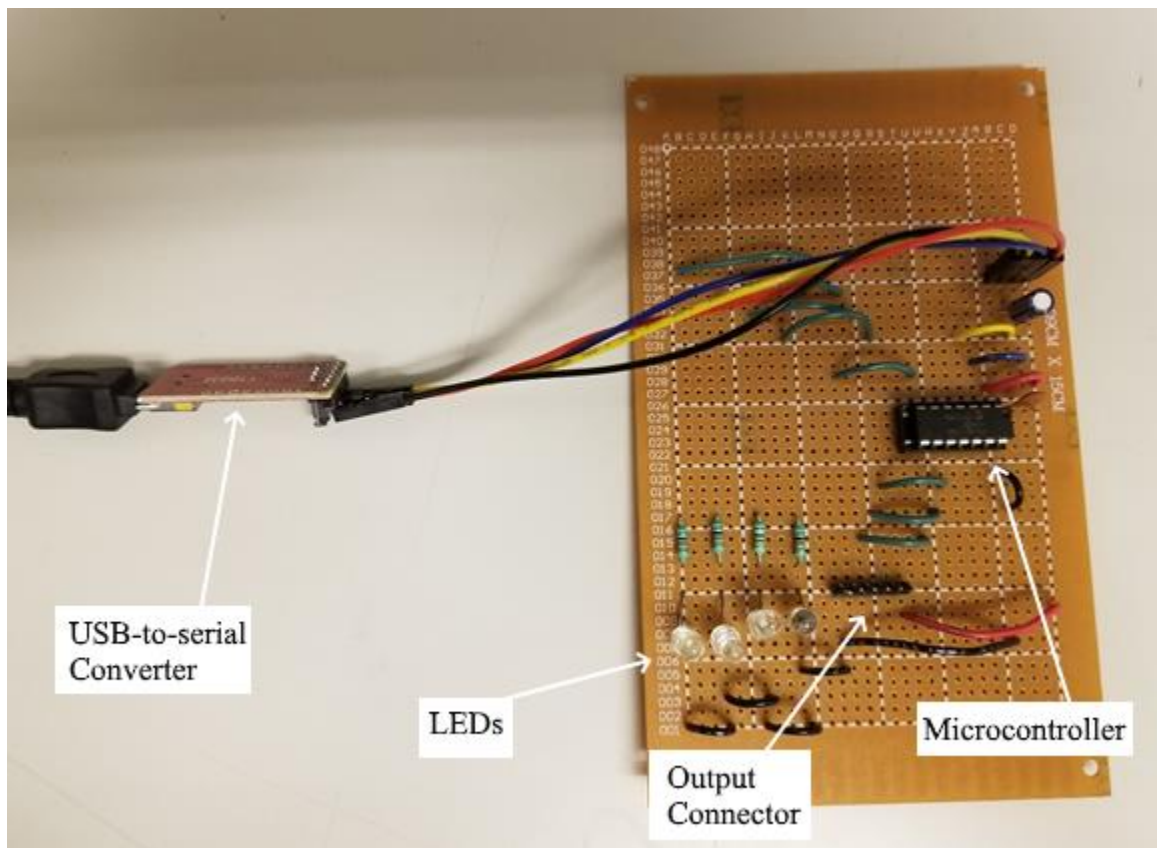


*Figure 36 - Second Selector*

The interface board includes a PIC microcontroller manufactured by Microchip Technology. Microcontrollers such as this are tiny programmable computers that can be programmed to serve a large variety of purposes. Specifically, the one present on this board was programmed to take the serial signal and translate it to the parallel signal that the multiplexer can understand. From the computer, terminal software is used to send single

character text commands indicating which pad should be selected. In addition to outputting logic signals, the board also has four LEDs that allow for visual indication of which pad is selected.

#### **5.1.10 Laptop Computer**

A fairly-standard laptop computer manufactured by Dell running Windows 10 was used to control the experiment. It was used to run the DPPMCA software needed to communicate with the DP5 modules, as well as the PuTTY serial terminal software used to send commands to the pad selector.

TeamViewer remote access software was used to control the computer over the internet. The computer's camera was pointed toward the selector so that the LEDs on it could be monitored. This was not strictly necessary for successful completion of the experiment, but it provided an easy way to monitor the selector to check that it was receiving the commands and reacting properly to them. This was deemed desirable due to the crude and improvised nature of the computer-controlled pad selector.

## **5.2 Experiment Methodology**

Once the equipment was set up, the actual experimental procedure was rather simple. The data collection process is automated except for changing pads. The only thing needed in between pad changings was to wait. This proved to be a downside to this particular scheme, as it turned out to take a long time to collect data, with rates in the neighborhood of 1000 per 24 hours. Because there were 16 pads, this meant that the already-long collection times for one pad needed to be multiplied by 16 in order to complete the entire experiment.

The length of the experiment and the simplicity in performing it provided impetus to automate it. However, the software for the DP5 has no built-in automation. It was decided that the experiment would be operated remotely using the computer-controlled pad selector described above and remote access software on the computer. This allowed the changing of pads remotely.

Therefore, the experimental procedure as designed was as follows:

1. Start DPPMCA software. A prompt should appear asking which DP5 it should be connected to. If this does not appear, click the “Connect/Disconnect” button. If the DP5 does not show up, check the connections and try again.
2. In DPPMCA, choose to connect to the DP5. The spectrum should appear. If the acquisition is running, stop the acquisition by clicking the “Start/Stop button”. If there is collected data, click the “Delete Data and Reset Time” button.
3. Start PuTTY software. Connect to the COM port that the data selector is mapped to in Windows.
4. Start DP5 data collection by clicking the “Start/Stop” button.
5. Select pad 1 by sending the pad 1 command to the selector via the PuTTY terminal software. For the collector that was constructed for the experiment, this is accomplished by typing “0” in the terminal window.
6. Clear data in DPPMCA by clicking the “Delete Data and Reset Time” button. This will clear spurious pulses caused by the multiplexer.

7. Ensure that the detector is collecting counts by monitoring DPPMCA for several minutes. This is necessary due to the low count rate.
8. Allow data collection to continue for 24 hours of run time.
9. Save collected data to disc by clicking the “Save As” button.
10. Select the next pad in sequence by sending the corresponding command to the selector via PuTTY. With the selector used in this experiment, this is accomplished by typing “1” through “9” for pads 2-10 and “A” through “F” for pads 11 through 16.
11. Repeat steps 5 through 9 until all 16 pads have data sets collected.
12. Perform one more run on pad 1 by selecting pad 1 by typing “0” in Putty and then repeat steps 5-8. This will be used to judge drift in gas gain due to leaking or air ingress.

After all data is collected, the drift in gas gain should be judged by examining the peak centroids and standard deviation of the very first pad 1 run performed with the one collected from step 12 using the instructions in section 5.2.1, where the processing of the data is addressed. If a difference between the centroids cannot be determined within the determined error, then the gas gain is likely to not have changed significantly. If it has, then the apparatus should be checked again and potential leaks fixed before running the experiment again. This proved to be the case during the first run of this experiment, which is what prompted the use of Apiezon Q sealing compound around all threaded connections.

While the original intent was for the experiment to run for 17 days, the stability of the gas pressure and composition appeared to not have changed, which allowed for longer data collection periods. Additional data was collected and gas gain was periodically monitored by collecting data from pad 1 and examining any drift. This is why in the data presented in Chapter 6, pad 1 has significantly more counts in it than the other pads. In total, about 30 days of data was collected.

### **5.2.1 Data Processing**

The data collected by DPPMCA is in the form of files with the .mca file extension. These are simple text files, allowing the data to be processed through any means the experimenter wishes. The specifications of the file format are outside of the scope of this thesis, but it may be found in the DPPMCA documentation.

MATLAB was used to sum the data collected from multiple runs of the same pad. This was accomplished by loading each of the files in sequence and adding together corresponding channels, and then writing the summed total to a file. MATLAB was also used to determine the centroids and standard deviations of each peak of interest. Representative output is shown in Figure 37. Two structures are seen in the spectra of all the data. The first is the noise floor, which represents spurious pulses from electronic noise. The second is the peak representing the energy deposition of the alpha particle as it crossed over the pad. This second peak is the peak of interest which is examined during data processing.

Once the bounds of the peak of interest were identified, a count-weighted average was calculated; this result is the center channel of the peak. Then, centered on this center

channel, the number of channels needed to encompass 68.27% of the total counts was determined. Half of this value was taken as the standard deviation, assuming a Gaussian distribution.

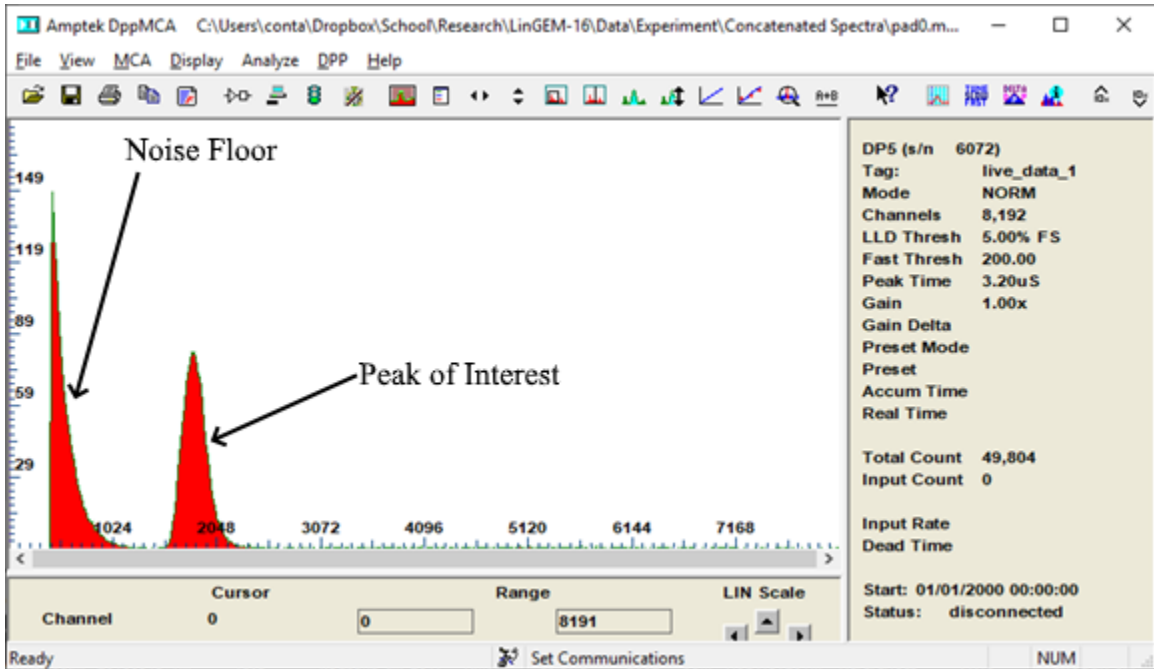


*Figure 37 - Representative Energy Deposition Spectrum*

This procedure was performed on the data sets collected from each pad.

## Chapter 6. Experiment Results

### 6.1 Expected Results from Calculations

The pads in the detector have a length of 3.125 mm and the total range of the alphas in the propane-based TEG fill gas is 68 mm. With the range of 39.83  $\mu\text{m}$  in tissue-like material comprised of unit-density propane TEG that SRIM had calculated, the tissue-equivalent length of the pads was

$$39.83 \mu\text{m} \times \frac{3.125 \text{ mm}}{68 \text{ mm}} = 1.83 \mu\text{m}$$

SRIM was used to calculate the stopping power of 5.49 MeV alphas in unit density propane-based TEG. The results are shown in Figure 38.

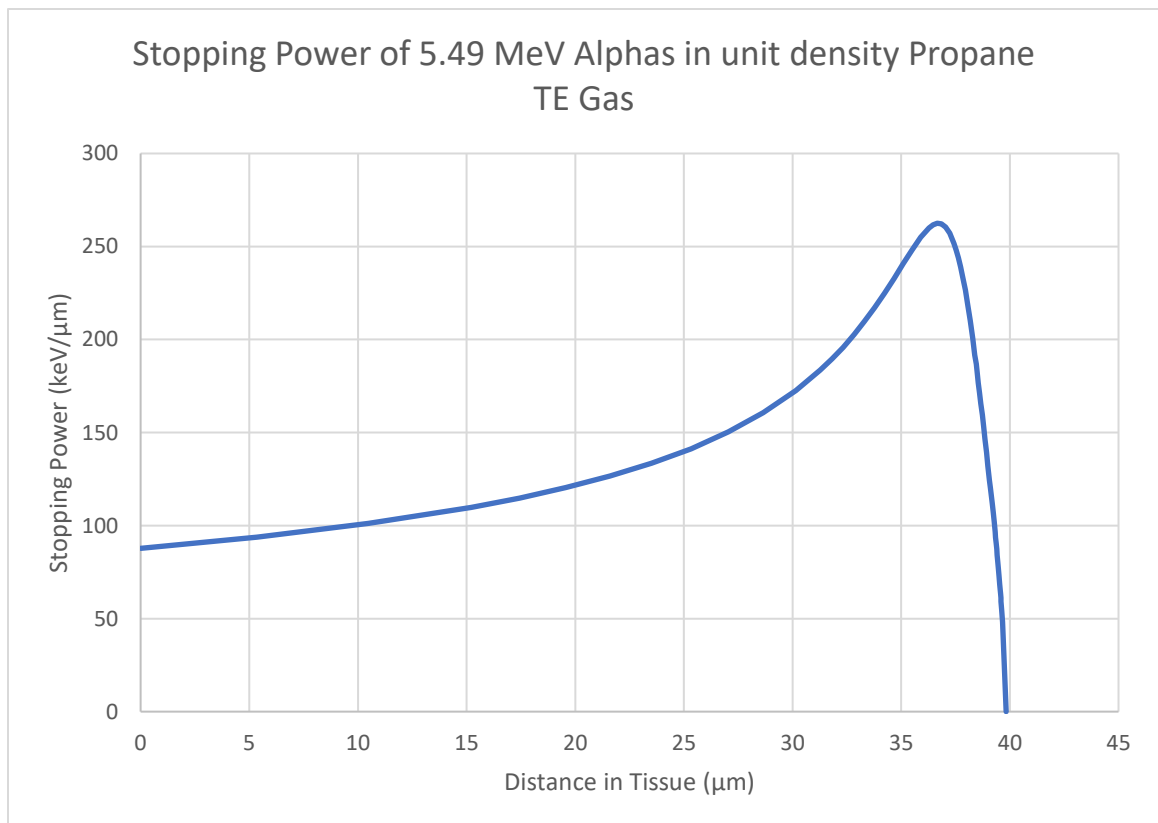
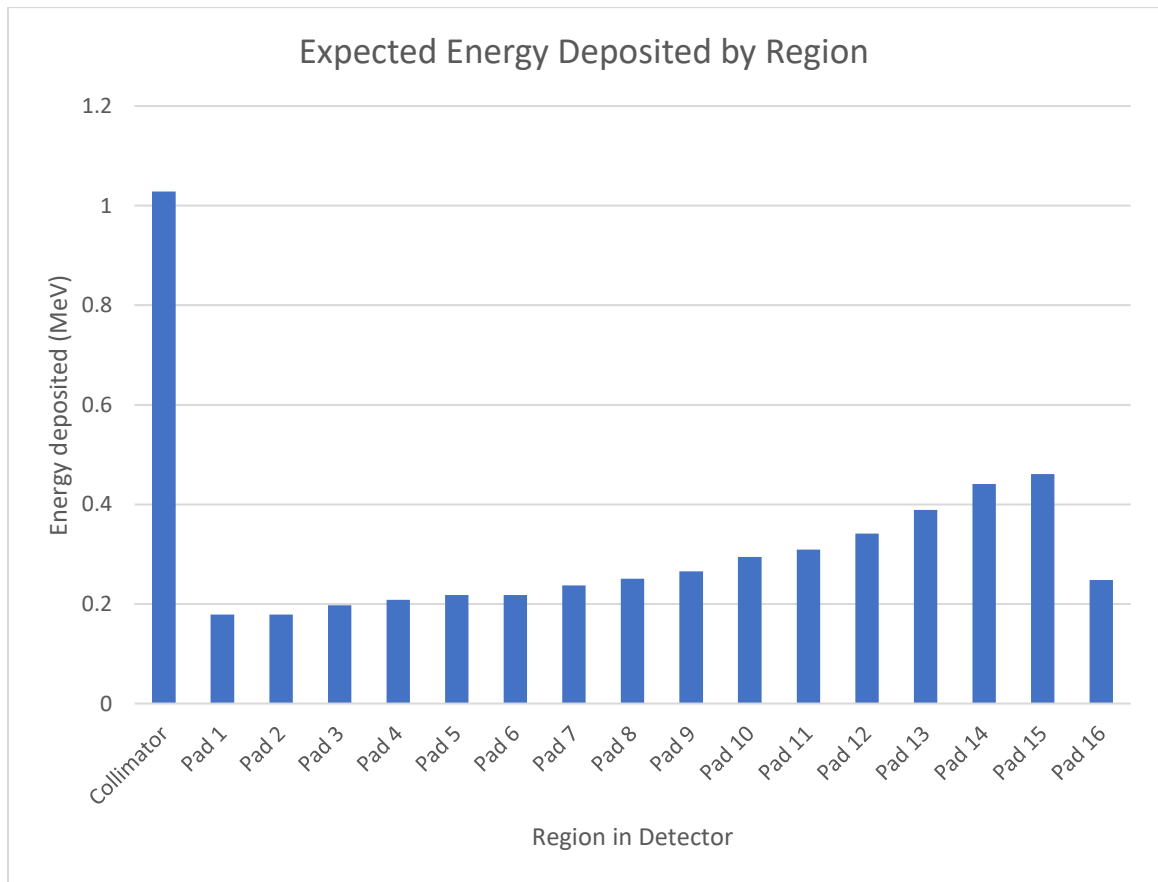


Figure 38 - Stopping Power Calculated with SRIM

By numerically integrating the data in Figure 38, the energy lost by the alpha in each area of the detector – and thus deposited in that area – can be determined. The results of this integration are shown in Figure 39. As the results show, a little over 1 MeV is lost within the collimator alone. This energy loss is unavoidable because the collimator cannot be omitted from the experiment, but it means that only about 4.46 MeV of the energy rather than the total 5.49 MeV energy could be measured. The rest is deposited non-uniformly over the 16 pads in the detector.



*Figure 39 – Expected Energy Deposited by Region Within Detector*

By neglecting the collimator and dividing the energy deposition by the effective tissue pad length of  $1.83 \mu\text{m}$ , the data in Figure 40 is arrived upon. Lines are added to guide the eye and aid in highlighting the trend, but are not intended to imply interpolation. The shape of

the Bragg curve is visible, but is slightly distorted due to the relatively low spatial resolution of the pads. Data collected from the detector should be expected to have a similar shape to it as it was designed to measure the energy deposited across each pad.

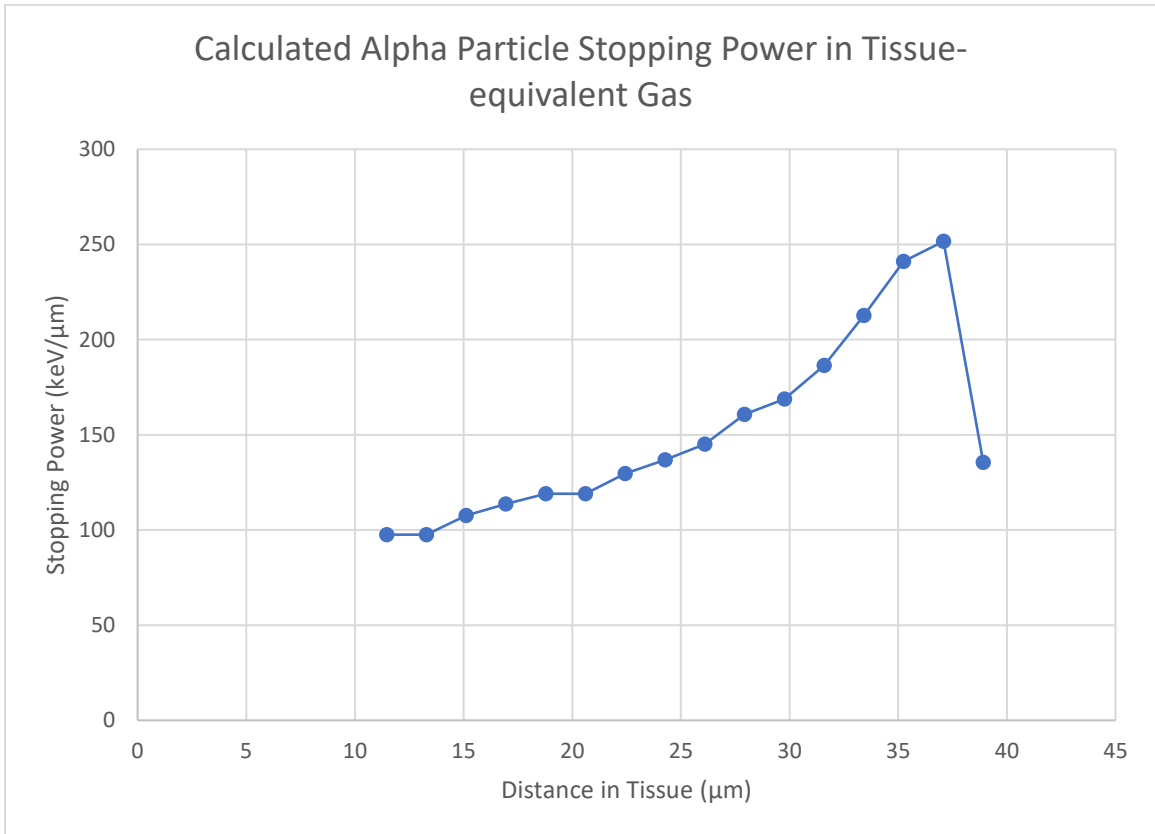


*Figure 40 - Expected Stopping Power in Unit Density Propane-based Tissue-equivalent Gas*

## 6.2 Raw Data

The raw data that was collected from the experiment is displayed in Table 2.

*Table 2 - Raw Data*

<b>Pad</b>	<b>Effective Pad Center Distance (<math>\mu\text{m}</math>)</b>	<b>Counts</b>	<b>Center Channel</b>	<b>Standard Deviation</b>
1	11.5	23275	917	58
2	13.3	2045	1721	177
3	15.1	2281	2560	170
4	16.9	3070	3190	185
5	18.8	3002	3636	184
6	20.6	2389	4119	209
7	22.4	2895	4615	220
8	24.3	2524	5061	253
9	26.1	13355	5130	259
10	27.9	2205	5841	279
11	29.8	2489	6211	295
12	31.6	2137	6979	304
13	33.4	2378	7589	367
14	35.3	2525	8097	557
15	37.1	3605	7552	969
16	38.9	3665	4319	1259

The raw data was plotted and is displayed in Figure 41. It exhibits a similar shape as the theoretical results, and the trend of increasing standard deviation with distance matches the trend of increasing along the path length that would be expected due to straggling.

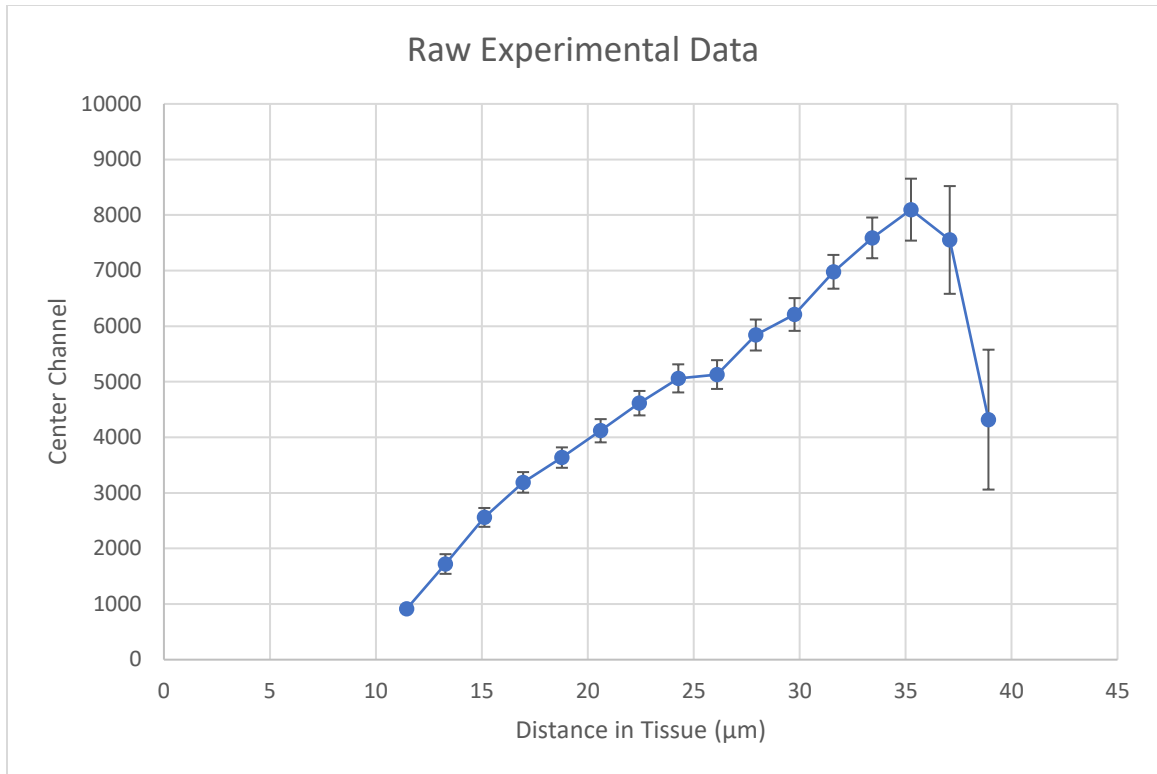


*Figure 41 - Plot of Raw Data*

### **6.3 Calibration**

In order to relate the collected data with the theoretical results, it must be calibrated somehow. This detector does not have a dedicated system for calibration, so a method was devised to use the theoretical energy deposition in one pad as a calibration point. The data used for calibration is shown in Table 3 and is reproduced from previous data presented.

*Table 3 - Data For Calibration Calculations*

<b>Pad</b>	<b>Effective Center Distance (μm)</b>	<b>Theoretical Stopping Power (keV/μm)</b>	<b>Centroid (channel)</b>	<b>Standard Deviation (channels)</b>
1	11.5	97.6	917	58
2	13.3	97.6	1721	177
3	15.1	108	2560	170
4	16.9	114	3190	185
5	18.8	119	3636	184
6	20.6	119	4119	209
7	22.4	130	4615	220
8	24.3	137	5061	253
9	26.1	145	5130	259
10	27.9	161	5841	279
11	29.8	169	6211	295
12	31.6	186	6979	304
13	33.4	213	7589	367
14	35.3	241	8097	557
15	37.1	252	7552	969
16	38.9	136	4319	1259

This data was used to calculate a calibration factor, which can convert the center channels into a stopping power value. It was calculated for each of the 16 pads with the following equation:

$$\text{Calibration Factor} = \frac{\text{Theoretical Stopping Power}}{\text{Center Channel}}$$

The potential calibration factors that were calculated are presented in Table 4.

*Table 4 - Calibration Factors*

<b>Pad</b>	<b>Effective Center Distance (<math>\mu\text{m}</math>)</b>	<b>Calibration Factor (keV/<math>\mu\text{m}</math>/channel)</b>	<b>Standard Deviation (keV/<math>\mu\text{m}</math>/channel)</b>
1	11.5	0.106	0.000747
2	13.3	0.0567	0.00122
3	15.1	0.0421	0.000871
4	16.9	0.0356	0.000805
5	18.8	0.0327	0.000735
6	20.6	0.0289	0.000737
7	22.4	0.0281	0.000754
8	24.3	0.0270	0.000835
9	26.1	0.0283	0.000894
10	27.9	0.0275	0.000936
11	29.8	0.0272	0.000978
12	31.6	0.0267	0.000991
13	33.4	0.0280	0.00125
14	35.3	0.0298	0.00203
15	37.1	0.0333	0.00394
16	38.9	0.0314	0.00482

The calibration factors were plotted to gauge their uniformity. This is shown in Figure 42. If the results were as expected, it should look like a horizontal line. However, the first several pads appear to be under-reporting the energy deposition in their locations along the particle's path. This is an indication that something is likely wrong in that part of the detector. If one of those data points were to be used to calibrate the result, the stopping power along all parts of the path would be higher than expected. It was decided that Pad 9's calibration factor would be used to arrive at the final data, as it lies in the middle of a plateau.

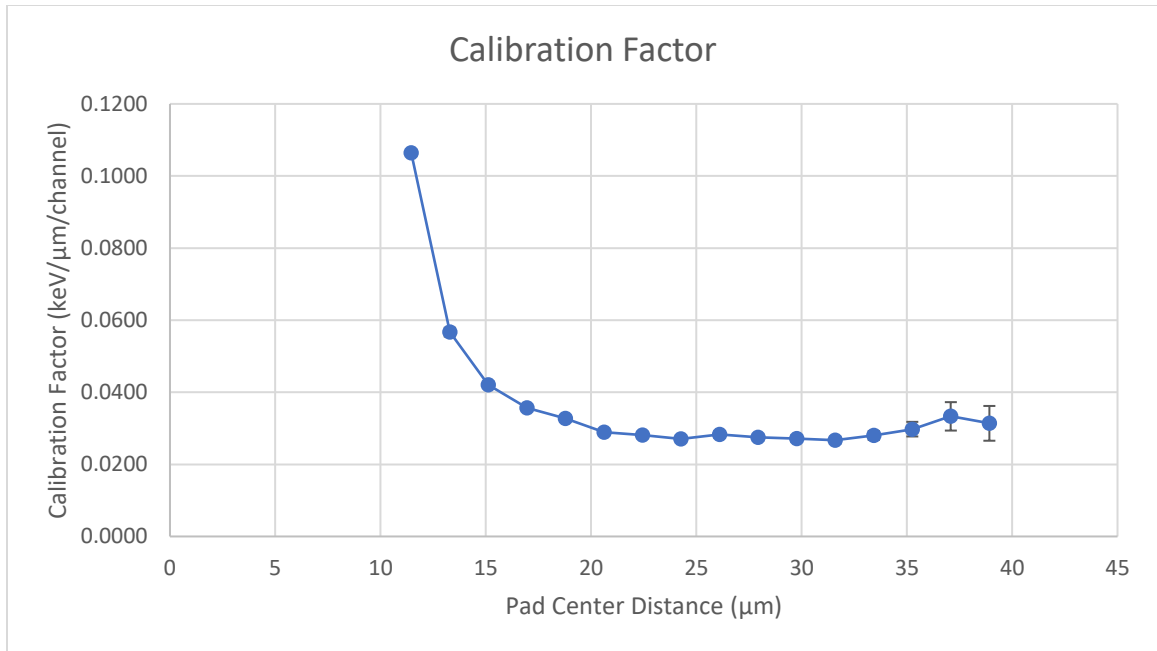


*Figure 42 - Plotted Calibration Factors*

## 6.4 Final Results

Using the Pad 9 calibration factor of 0.0283 keV/μm/channel, the collected data was calibrated in terms of keV/μm. The data is presented in Table 5.

*Table 5 - Final Results*

<b>Pad</b>	<b>Effective Center Distance (<math>\mu\text{m}</math>)</b>	<b>Calibrated Stopping Power (<math>\text{keV}/\mu\text{m}</math>)</b>	<b>Standard Deviation (<math>\text{keV}/\mu\text{m}</math>)</b>
1	11.5	25.9	1.63
2	13.3	48.7	5.01
3	15.1	72.4	4.79
4	16.9	90.2	5.23
5	18.8	103	5.20
6	20.6	116	5.91
7	22.4	131	6.22
8	24.3	143	7.16
9	26.1	145	7.33
10	27.9	165	7.88
11	29.8	176	8.33
12	31.6	197	8.60
13	33.4	215	10.4
14	35.3	229	15.8
15	37.1	214	27.4
16	38.9	122	35.6

The data was plotted and compared to the theoretical data that was calculated earlier. This is shown in Figure 43.

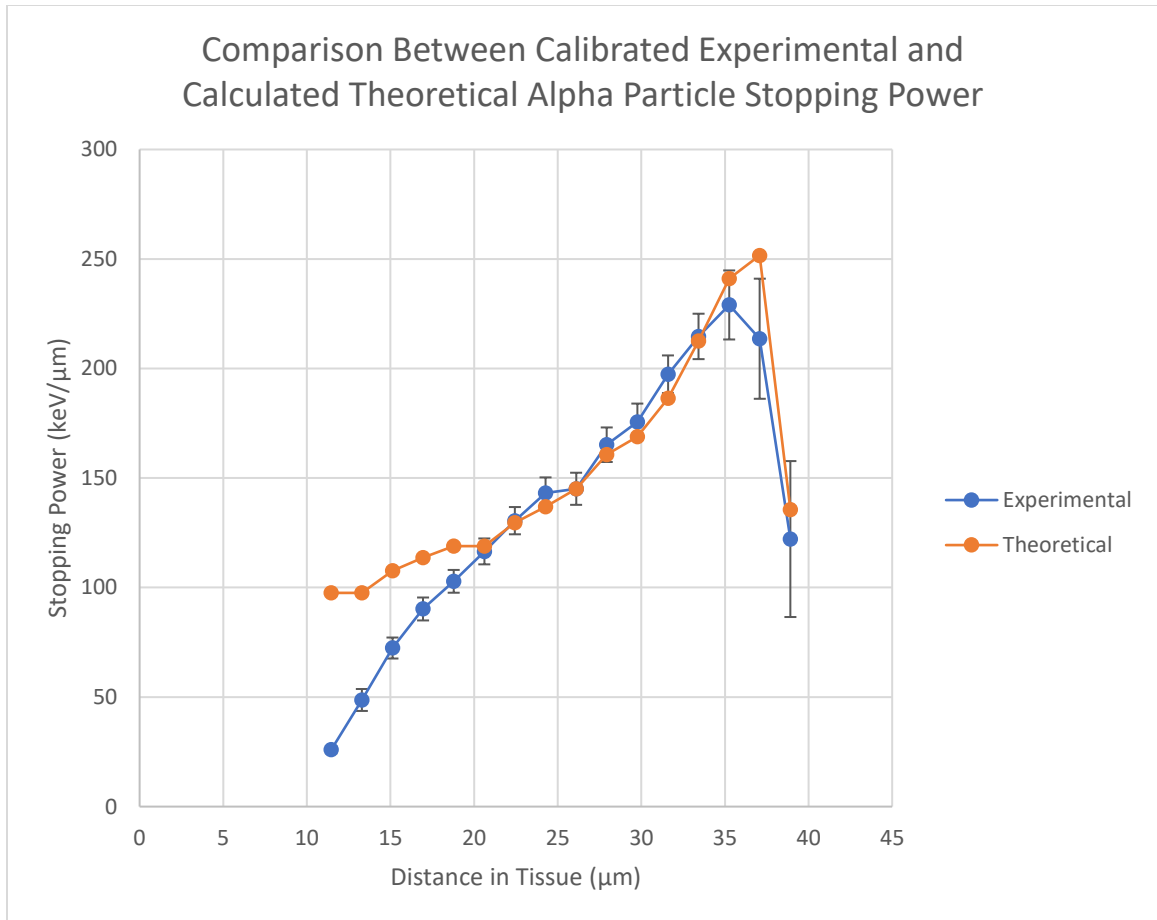


Figure 43 - Plot of Final Results

## 6.5 Discussion

While the results from the final 11 pads track closely with the expected results, the first 5 pads do not. Rather curiously, it seems that the closer the pad was to the collimator, the more the result deviates from what was expected. It is possible for GEMs to exhibit non-uniform gain across their entire area, but this is not a satisfying explanation because of the clear downward trend across the distance of almost 16 mm from pad 5 to the collimator does not seem to be the random results that one would expect from minor variations and imperfections.

One possible explanation for this is that the collimator builds up charge and distorts the electric field of the drift volume. This could have an effect on the results by impeding the collection of charge. A possible remedy for this is using a conductive collimator that is grounded to prevent the buildup of charge; however, care would have to be taken not to facilitate electrical arcing between the drift plane and the top foil of the GEM.

A curious result was observed while examining output from the preamplifier with an oscilloscope. Images from the scope are shown in Figure 44. The leftmost image represents the output received from the input of a test pulse from a pulser. The middle image represents a pulse from Pad 1, and the rightmost image represents a pulse from Pad 9.

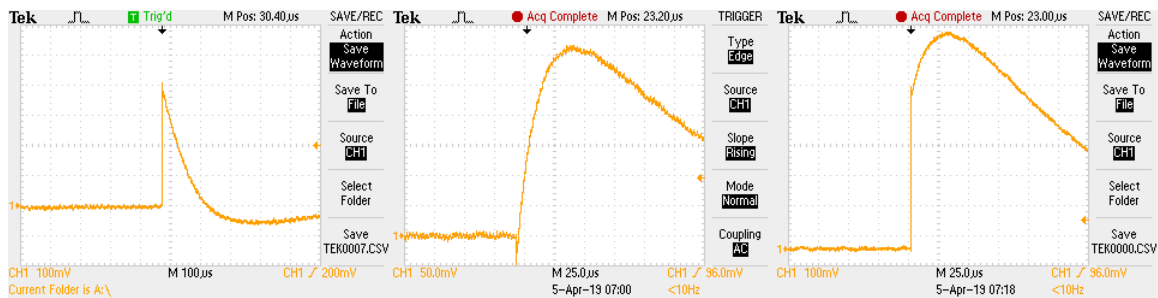


*Figure 44 - Preamplifier Output*

The pulse that results from feeding a test pulse into the preamplifier looks exactly as expected. However, the pulses from Pad 1 and Pad 9 exhibit evidence of unusually slow charge collection time. In a normal proportional counter tube, there is a “fast” component from the electrons, which travel quickly and are collected in under a microsecond, as well as a “slow” component from the positive ions, which can take tens of microseconds to be collected. A hallmark of GEMs is that the collector electrodes only “see” electrons, so the charge collection time should be very fast and should have no slow component.

However, Pad 1 apparently only has a slow component, while pads further away have substantial fast component and a minor slow component. As a GEM detector, there should be no slow component in pulses from this experiment at all.

Perhaps this would not normally be an issue, but the DP5 multichannel analyzer cannot measure the full result from pulses that take as long to fully collect as the ones in this detector. Therefore, all of the pads were “underreporting” energy to some degree; however, the worst offenders were those closer to the collimator. However, this does not seem to be something that could be explained by the collimator building up charge.

It is not possible to confirm with the tools on hand, but it is possible that there is some manner of positive ion flow into the induction volume. If positive ions enter the induction volume out of the bottom of the GEM foil alongside electrons, they will partially suppress the fast signal from the electrons. Then as they accelerate back toward the GEM foil due to the electric field direction in the induction volume, they will contribute a slow component to the signal.

A possible culprit for positive ions entering the induction volume could be the use of unoptimized electric field strengths. Testing with similar GEMs shows that electric fields of around 4 kV/cm are optimal in the induction region [33], but 1 kV/cm was used in this experiment to keep the voltages lower. This may have been a mistake if the electric fields are not strong enough to ensure positive ions stay out of the volume.

## Chapter 7. Conclusions

This project partly completed its objectives. The detector is capable of collecting a data set that shows the character of a Bragg curve. However, the investigation that was performed could not arrive at a satisfying explanation for the underreporting of the detector pads closest to the collimator.

Nonetheless, this project shows that it is relatively easy to construct a device using GEM technology. Because the foils can be purchased off-the-shelf and the balance of the detector can be constructed with conventional electronics manufacturing techniques, detectors utilizing particle tracking technology can be constructed in any moderately well-equipped workshop. The most difficult part in fact had nothing to do with the GEM technology itself; ensuring a good gas-tight seal in the enclosure proved to be the most challenging part of the project. The technique used to produce the feedthroughs was developed as an original concept for this project. In spite of the unconventional use of Apiezon wax as a space filler, it proved to provide excellent gas-tight sealing.

The multiplexer scheme used to allow measurement of 16 different pads with one preamplifier works in principle; however, the experiment run time scales linearly with the number of pads in the design. While the electronics needed are quite simple, 16 pads likely represent the limit of what one would want to attempt with this configuration. The originally-planned 16 day run time was a bit of a stretch as it was, so doubling the spatial resolution and increasing the pad count to 32 would be ill-advised. This experiment would benefit from a proper particle-tracking configuration that measures all pads simultaneously with more complex electronics.

Nonetheless, as a further development of the proof of concept demonstrated by Sipaj, this project is a success in that it improved upon the performance exhibited by its predecessor's design. While the resulting Bragg curve is by no means perfect, it lines up with the results more closely than the earlier attempt showing that the improvements were modestly successful.

## 7.1 Future Developments

The results collected from the detector built for this experiment show promise. The data collected has the character of a Bragg curve, in spite of imperfections near the collimator. The following are specific recommendations that are made based on the experience gained from this project.

- There is a lot of room for the voltages and resistor values to be optimized in the high voltage section of the detector, along with the heights of the drift and induction regions. Optimization of electric fields within the detector volumes should improve performance.
- Use of a conductive collimator or some other collimator scheme that mitigates the effects – if there are in fact any – of charge buildup on the surface of the collimator. It is not certain if this is an issue, but it should be ruled out.
- Include an additional source of calibration. A low-energy photon source such as  $^{55}\text{Fe}$  could provide peaks in the collected energy spectrum that can be used as calibration points.

- The source of the apparent “slow” component in the charge collection should be investigated, as there shouldn’t be one to begin with. It is possible that it is the result of unoptimized electric fields, but there could also have been some non-apparent flaw with the electronics design of the detector that caused it.
- A detector with a more advanced particle-tracking concept could collect data much faster by taking counts from each pad simultaneously. 16 pads likely represents the practical limit of the multiplexer concept, just due to extremely-long data collection periods.

## 8 References

- [1] U.S. NIM Committee, "Standard NIM Instrumentation System," United States Department of Energy, 1990.
- [2] J. E. Turner, "Interaction of Ionizing Radiation With Matter," *Health Physics*, vol. 88, no. 6, pp. 520-544, 2005.
- [3] G. F. Knoll, Radiation Detection and Measurement, Fourth Edition, John Wiley & Sons, Inc., 2010.
- [4] R. Lapp and H. Andrews, Nuclear Radiation Physics, Prentice-Hall, Inc., 1948.
- [5] H. Cember and T. Johnson, Introduction to Health Physics - Fourth Edition, The McGraw-Hill Medical, 2009.
- [6] E. Podgorsak, Radiation Oncology Physics: A Handbook for Teachers and Students, International Atomic Energy Agency, 2005.
- [7] E. Hall and A. Giaccia, Radiobiology for the Radiologist - Seventh Edition, Lippincott Williams & Wilkins, 2012.
- [8] D. Ebner and T. Kamada, "The Emerging Role of Carbon-Ion Radiotherapy," *Frontiers in Oncology*, vol. 6, no. 140, pp. 1-6, 2016.
- [9] J. Ziegler, M. Ziegler and J. Biersack, "SRIM - The stopping and range of ions in matter (2010)," *Nuclear Instruments and Methods in Physics Research B*, vol. 268, pp. 1818-1823, 2010.
- [10] A. Sipaj, "Simulation, Design and Construction of a Gas Electron Multiplier for Particle Tracking," University of Ontario Institute of Technology, 2012.
- [11] G. Jauncey, "The Early Years of Radioactivity," *American Journal of Physics*, vol. 14, pp. 226-241, 1946.
- [12] J. Hughes, "Rutherford, Radioactivity and the Origins of Nuclear Physics," *Journal of Physics: Conference Series*, vol. 381, p. 012001, 2012.
- [13] H. Nikjoo, S. Uehara and D. Emfietzoglou, Interaction of Radiation with Matter, CRC Press, 2012.
- [14] J. Ziegler, "James Ziegler - SRIM & Trim," [Online]. Available: <http://www.srim.org/>.
- [15] M. W. Charles, "Radon exposure of the skin: I. Biological effects," *Journal of Radiological Protection*, vol. 27, pp. 231-252, 2007.
- [16] J. Valentin, "Basic anatomical and physiological data for use in radiological protection: reference values: ICRP Publication 89," *Annals of the ICRP*, vol. 32, no. 3-4, pp. 1-277, 2002.
- [17] G. K. Gillmore, R. G. M. Crockett and T. A. Przylibski, "IGCP Project 571: Radon, Health and Natural Hazards," *Natural Hazards and Earth System Sciences*, vol. 10, pp. 2051-2054, 2010.
- [18] J. Planinik, B. Suveljak and Z. Faj, "Radon distribution in dwellings," *Journal of Radiological Protection*, vol. 14, no. 3, pp. 235-239, 1994.

- [19] J. H. Lubin, "Studies of Radon and Lung Cancer in North America and China," *Radiation Protection Dosimetry*, vol. 104, no. 4, pp. 315-319, 2003.
- [20] B. Allen, C. Raja, S. Rizvi, Y. Li, W. Tsui, D. Zhang, E. Song, C. Fa Qu, J. Kearsley, P. Graham and J. Thompson, "Targeted Alpha Therapy for Cancer," *Physics in Medicine and Biology*, vol. 49, pp. 3703-3712, 2004.
- [21] E. Deshayes, M. Roumiguie, C. Thibault, P. Beuzeboc, F. Cachin, C. Hennequin, D. Huglo, F. Rozet, D. Kassab-Chahmi, X. Rebillard and N. Houédé, "Radium-223 Dichloride for Prostate Cancer Treatment," *Drug Design, Development and Therapy*, vol. 2017:11, pp. 2643-2651, 2017.
- [22] S. Brown, Introduction to Electrical Discharges in Gases, John Wiley & Sons, Inc., 1966.
- [23] U. Fano, "Penetration of Protons, Alpha Particles, and Mesons," *Annual Review of Nuclear Science*, vol. 13, pp. 1-66, 1963.
- [24] L. Lindborg and A. Waker, Microdosimetry: Experimental Methods and Applications, CRC Press, 2017.
- [25] F. Sauli, "GEM: A New Concept for Electron Amplification in Gas Detectors," *Nuclear Instruments and Methods in Physics Research A*, vol. 386, pp. 531-534, 1997.
- [26] F. Sauli, "The gas electron multiplier (GEM): Operating principles and applications," *Nuclear Instruments and Methods in Physics Research A*, vol. 805, pp. 2-24, 2016.
- [27] A. Sharma, "3D Simulation of Charge Transfer in a Gas Electron Multiplier (GEM) and Comparison to Experiment," *Nuclear Instruments and Methods in Physics Research A*, vol. 454, pp. 267-271, 2000.
- [28] W. Shockley, "Currents to Conductors Induced by a Moving Point Charge," *Journal of Applied Physics*, vol. 9, no. 10, pp. 635-636, 1938.
- [29] S. Ramo, "Currents Induced by Electron Motion," *Proceedings of the I.R.E.*, vol. 27, pp. 584-585, 1939.
- [30] P. De Visschere, "The Validity of Ramo's Theorem," *Solid-State Electronics*, vol. 33, no. 4, pp. 455-459, 1990.
- [31] M. Berger, J. Coursey and M. Zucker, "ESTAR, PSTAR, and ASTAR: Computer Programs for Calculating Stopping-Power and Range Tables for Electrons, Protons, and Helium Ions (version 1.21)," National Institute of Standards and Technology, 1999. [Online]. Available: <http://physics.nist.gov/Star>.
- [32] J. Moore, C. Davis and M. Coplan, Building Scientific Apparatus: A Practical Guide to Design and Construction: Second Edition, Addison-Wesley Publishing Company, Inc., 1989.
- [33] S. Bachmann, A. Bressan, L. Ropelewski, F. Sauli, A. Sharma and D. Mormann, "Charge Amplification and Transfer Processes in the Gas Electron Multiplier," *Nuclear Instruments and Methods in Physics Research A*, vol. 438, pp. 376-408, 1999.